UNIVERSITY OF PÉCS

Excitations of Quasi-Two-Dimensional Electron Systems in Magnetic Field

Judit Sári

Doctoral Thesis

Supervisor

Csaba Tőke

Institute of Physics

June 2015

Contents

List of Symbols and Conventions

a_0	Bohr radius
c	speed of light
$e > 0$	elementary charge
ϵ_0	vacuum dielectric constant
ϵ_r	relative dielectric constant
$\epsilon_r(\mathbf{q}, \omega)$	dynamical dielectric function
$h.c.$	Hermitian conjugate
$H_n(x)$	Hermite polynomial
$\ell = \sqrt{\hbar/eB}$	magnetic length
$L_n(x)$	Laguerre polynomial
$L_n^m(x)$	associated Laguerre polynomial
m_0	electron rest mass
μ_0	vacuum permeability
μ_B	Bohr magneton
$\Theta(x)$	Heaviside step function
v_F	Fermi velocity

The identity matrix and the Pauli matrices are

$$\sigma_0 = \begin{pmatrix} 1 & 0 \\ 0 & 1 \end{pmatrix}, \qquad \sigma_x = \begin{pmatrix} 0 & 1 \\ 1 & 0 \end{pmatrix}, \qquad \sigma_y = \begin{pmatrix} 0 & -i \\ i & 0 \end{pmatrix}, \qquad \sigma_z = \begin{pmatrix} 1 & 0 \\ 0 & -1 \end{pmatrix}.$$

Chapter 1

Introduction

Though quasi-two-dimensional systems had always been in the core of scientific interest, the first isolation of graphene, a two-dimensional carbon allotrope, in 2005 (see Ref. [114] and [170]) gave new life to the research of two-dimensional (2D) materials.[1] The peculiarity of graphene is rooted in its two-dimensional nature, and manifests itself in extraordinary properties such as the conical band structure at low energies, or the anomalous quantum Hall effect (QHE). The conical valleys, usually referred to as Dirac cones, are described by the Dirac equation of massless particles, however with a much lower velocity v_F instead of the speed of light c. This makes graphene the first 2D condensed matter system that hosts massless, charged fermions. The versatile material properties of graphene open the possibility for applications from chemical sensors to transistors, see Ref. [45].

On the one hand, the boost in graphene research is engined by the interest in the truely 2D nature of the material, and this has led to the isolation and investigation of a plethora of other 2D materials. An important class is the transition metal dichalcogenides, which are layered crystals offering themselves to exfoliation techniques. Prominant examples include MoS_2, $MoSe_2$, WS_2 or WSe_2, for details see the review article [161]. Another important material besides the transition metal dichalcogenides is the hexagonal boron-nitride (hBN), few layer samples are readily made by chem-

[1] Several reviews demonstrate the tremendous research interest in graphene. Castro Neto *et al.* in [111] review the electronic properties of monolayer and bilayer graphene, Kotov *et al.* in [78] focuses on the electron-electron interaction in graphene. Goerbig in [48] reviews the properties in magnetic field, Peres in [123] and Das Sarma *et al.* in [33] deal with transport phenomena, while in their recent review [12] Basov *et al.* concentrates on graphene spectroscopy.

ical vapour deposition, see Ref. [156]. Some metallic 2D structures have also been recently fabricated, e.g. single-layered rhodium, see Ref. [35], or ultrathin palladium nanosheets, see [166]. An atlas of 2D materials is given in Ref. [96], where the authors review the properties of other 2D crystals including silicene, germanene, silicon carbide. It is clear that in spite of their similar 2D nature these materials vary considerably as far as their electrical properties or band structure are concerned. Some of them host Dirac electrons, others are usual semiconductors or insulators, see Ref. [162].

On the other hand, the interest in graphene is inspired by the presence of Dirac electrons, which induced a quest for other Dirac systems. An important class of three-dimensional materials that host Dirac electrons on their surface states is topological insulators, which have naturally become the focus of intense research in the last decade, see review article Ref. [55]. Besides, in some layered organic compounds, including α-(BEDT-TTF)$_2$I$_3$, the low-energy band structure is described by conical valleys. These 3D crystals have strong 2D nature and massless fermions usually appear under high pressure or strain, see Ref. [109], [151] and [153], and also discussion in Sec. 2.4.4.

However impressive the above list of 2D materials or crystals with Dirac cones may be, we should note that the research of these materials is still intense with several open questions to be answered. Undoubtedly, graphene is the best known among them, though our understanding is not complete in this case either, see the list of debated or open questions in [78]. The same is particularly true for the other materials. Some of them have not even been isolated, e.g. silicene, in other cases even basic material properties such as the low-energy band structure of α-(BEDT-TTF)$_2$I$_3$ is a debated issue, see [3],[101]. For these reasons we believe that the theoretical investigation of the elementary properties and many-body effects of these quasi-two-dimensional materials is a timely issue and reckons on general interest.

1.1 Outline of Thesis

In the present thesis we will examine single-particle and collective excitations of quasi-two-dimensional materials including monolayer and bilayer graphene and layered organic crystal α-(BEDT-TTF)$_2$I$_3$ (aI3). Our investigation will exclusively focus on

properties within a strong magnetic field, either in the integer quantum Hall regime, which allows for the mean-field treatment of electron-electron interactions, or in a field where quantum Hall ferromagnetic (QHF) states appear.

In Chap. 2 we present the materials we are dealing with in the present thesis. We focus on basic material properties and the low-energy band structure of each material, and derive the Landau level (LL) spectrum and orbitals necessary for further calculations. We also give a short outlook on experiments in each case to give a general context for our theoretical investigations. Besides reviewing the literature, however, we demonstrate how the relativistic covariance of the underlying Dirac equation of massless fermions in aI3 can be used to deduce its LL spectrum. Our contribution is to draw parallel between the tilt of the Dirac cones in aI3 and the role of the in-plane electric field for which graphene is subjected in addition to the perpendicular magnetic field.

Chap. 3 is devoted to the magneto-optical properites calculated in a single-particle picture for α-(BEDT-TTF)$_2$I$_3$ and for graphene in a magnetic and an in-plane electric fields. In both cases the rotational symmetry is broken either by an in-plane electric field or the tilt of the Dirac cones. The reduced symmetry in such systems makes the allowed dipolar optical transitions evolve into a fan of interband transitions. We analyze the emerging optical properties, and predict that infrared absorption spectra yield quantitative information on the tilted Dirac cone structure in aI3.

In Chap. 4 we study the collective modes of a low-energy continuum model of $\alpha-$(BEDT-TTF)$_2$I$_3$ with tilted anisotropic Dirac cones. We show that the tilt of the cones causes a unique intervalley damping effect: the upper hybrid mode of one cone is damped by the particle-hole continuum of the other cone in generic directions. Furthermore, as some experimental findings and *ab initio* calculations indicate that besides the massless carriers massive ones are also present in aI3, we extend our analysis of the collective modes to incorporate both carrier types. Notably, we analyse how the presence of massive carriers affects the total response, and demonstrate how doping can tune aI3 between regimes of isotropic and anisotropic screening.

In the last chapter we analyse bilayer graphene in strong magnetic fields, when either integer QH states or QHF states appear. Though in the former case a standard Landau

quantization serves an excellent explanation for the appearance of plateaus, in the latter case they arise due to interactions. Nevertheless, the low-energy excitations in both cases are magnetoexcitons, whose dispersion relation depends on single- and many-body effects in a complicated manner. We find that the mixing of different Landau level transitions not only renormalizes the magnetoexciton modes, but essentially changes their spectra and orbital character at finite wave length. We conclude by mentioning some experimental possibilities, e.g. inelastic light scattering experiments, through which our predictions can be probed.

Chapter 2

Quasi-Two-Dimensional Material Systems

This introductory chapter is devoted to those quasi-two-dimensional electron systems that are the subject matter of the present thesis. Our aim is to review the general properties of these systems, even so we shall limit ourserves to only those features that are essential for further analysis. We start our discussion by a short and up-to-the-point section on the conventional two-dimensional electron gas (2DEG). We introduce our basic notation and derive the Landau states and corresponding eigenfunctions of the 2DEG. Afterwards, we turn our attention to monolayer and bilayer graphene. We review the basic electronic properties and the most noteworthy experimental connections, but here again much of the emphasis is given to the derivation of the eigenstates and eigenfunction in a perpendicular magnetic field, which we will rely on in later chapters. Finally we introduce the layered organic conductor α-(BEDT-TTF)$_2$I$_3$ and provide a basic description of the high pressure phase of this material that hosts massless Dirac femions. We conclude the chapter with an overview of related organic compounds.

2.1 Landau Level Spectrum of Conventional 2DEG

Today conventional 2DEG is routinely realized in, among other systems, the semiconductor - oxide interface of MOSFETs (metal-oxide-semiconductor field-effect transistor) or the inversion layer of GaAs-Al$_x$Ga$_{1-x}$As heterostructures and quantum wells.

The properties of such an electron system is described in detail from various aspects in e.g. [4], [46], [142]. Here we restrict our attention to the single-particle eigenstates and eigenfunctions in a perpendicular magnetic field. The corresponding Hamiltonian reads

$$\hat{H}_{\mathrm{Q}} = \frac{(\hbar\mathbf{q} + e\mathbf{A})^2}{2m_Q}, \tag{2.1}$$

The LL spectrum is given by

$$\epsilon_n^{\mathrm{Q}} = \hbar\omega_c \left(n + \frac{1}{2}\right), \tag{2.2}$$

where $\omega_c = eB/m_Q$ is the appropriate cyclotron frequency and $n \geq 0$ is an integer. With our particular gauge choice $\mathbf{A} = (-yB, 0, 0)$ the eigenstates are given in terms of the harmonic oscillator eigenfunctions $\phi_n(y)$ as:

$$\phi_{n,k}(\mathbf{r}) = \frac{e^{ikx}}{\sqrt{2\pi}}\phi_n(y - \ell^2 k) \equiv \frac{e^{ikx}}{\sqrt{2\pi}} \frac{1}{\sqrt{\sqrt{\pi}2^n n!\ell}} H_n(\frac{y}{\ell} - \ell k) e^{-(\frac{y}{\ell} - \ell k)^2/2}. \tag{2.3}$$

2.2 Monolayer Graphene

2.2.1 Graphene as a Single Layer of Graphite - Preparation Methods

To start our discussion on single layer graphene we review here the different methods of its preparation, with the intention to provide a general background for further discussion.

Graphite, a three-dimensional allotrope of carbon, is made up of two-dimensional graphene layers, which are coupled together by van der Waals forces, thus graphite offers itself for mechanical exfoliation. Indeed, the earliest method of producing monolayer graphene is the mechanical exfoliation of graphite or the so called *Scotch Tape Method*, during which monolayer or multilayer samples are exfoliated from a graphite crystal by a simple adhesive tape, see Ref. [114] and [170]. Mechanical exfoliation provided the highest mobility samples so far, the monolayer flakes can be put on a substrate or can be suspended, though their size is not controllable.

Graphene can also be epitaxially grown on SiC or on hBN, though the graphene flakes produced with this method usually suffer from the effect of the surface. Another preparation method is chemical vapor deposition, which enabled us to produce extremely large samples, even up to width of 30 inches, see [7]. The high quality of the samples produced in this way made immediate applications possible, e.g. fabricating transparent electrodes. Various other, mainly chemical methods are also available to produce graphene in a usually simple setup, however, the quality of the samples may largely depend on the preparation method itself. These methods include electrochemical exfoliation or graphene prepared in a liquid phase, for details see [86], [120] and [146]. A detailed summary of the preparation methods is given in [12].

2.2.2 Elementary Properties in Zero Magnetic Field

In graphene the carbon atoms are arranged in a hexagonal structure. This structure requires sp^2 hybridization of the 2s and 2p orbitals, leaving a single unhybridized $2p_z$ orbital that is perpendicular to graphene's plane and provides an electron to participate in electric conductivity.

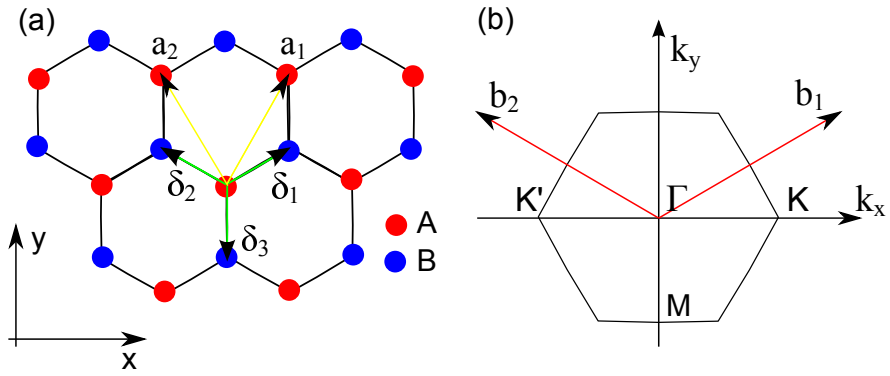

Figure 2.1: Panel (a): the primitive cell of graphene, with two atoms A and B and the lattice vectors $\mathbf{a}_1 = (a\sqrt{3}/2, 3a/2)$ and $\mathbf{a}_2 = (-a\sqrt{3}/2, 3a/2)$. In addition, the vectors connecting the nearest neighbour atoms $\delta_1 = (a\sqrt{3}/2, a/2)$, $\delta_2 = (-a\sqrt{3}/2, a/2)$, $\delta_3 = (0, -a)$ are also depicted. Panel (b): The first Brillouin zone of graphene with the reciprocal lattice vectors $\mathbf{b}_1 = (2\pi/a\sqrt{3}, 2\pi/3a)$, $\mathbf{b}_2 = (-2\pi/a\sqrt{3}, 2\pi/3a)$ and high symmetry points, including K=$(4\pi/3\sqrt{3}a, 0)$ and K'=$(-4\pi/3\sqrt{3}a, 0)$.

Fig. 2.1(a) shows the honeycomb structure of graphene. Its lattice is a triangular lattice with a primitive cell containing two atoms denoted as A and B. Both the A

and B atoms respectively build up a triangular lattice, referred to as sublattices. The nearest neighbour atoms are connected by vectors $\delta_i =$ with $i = 1, 2, 3$, while the lattice vectors $\mathbf{a}_1$ and $\mathbf{a}_2$ connect two A or B atoms. a denotes the carbon-carbon distance, which is $a \approx 1.42$ Å. The corresponding Brillouin zone is also a hexagon, with two inequivalent corner points traditionally denoted as K and K', see Fig. 2.1(b).

The simplest, but most frequently used band structure model of graphene is the tight-binding model, first derived by Wallace in 1947 in Ref. [159]. Note that Ref. [13] gives a detailed analysis of the tight-binding model of graphene. In second quantized formalism the tight-binding Hamiltonian is

$$\hat{H}_{\mathrm{G}} = -t \sum_{<i,j>,\sigma} [a^{\dagger}_{\sigma,i} b_{\sigma,j} + h.c.] - t' \sum_{\ll i,j \gg,\sigma} [a^{\dagger}_{\sigma,i} a_{\sigma,j} + b^{\dagger}_{\sigma,i} b_{\sigma,j} + h.c.] \tag{2.4}$$

$a_{\sigma,j}$ ($b_{\sigma,j}$) are annihilation operators that annihilates an electron with σ spin at site $\mathbf{R}_j$ of sublattice A (B). $< i, j >$ ($\ll i, j \gg$) denotes a summation through (next-)nearest neighbours. The value of the nearest neighbour hopping amplitude $t \approx 2.8$eV, while next-nearest neighbour hopping amplitude is estimated to be $t' \approx 0.1$eV. Neglecting the next-nearest neighbour hopping as a first approximation, the energy spectrum is

$$\epsilon^{\mathrm{G}}(\mathbf{k}) = \pm t \sqrt{3 + 2\cos(\sqrt{3}k_x a) + 4\cos(\sqrt{3}k_x a/2)\cos(3k_y a/2)}. \tag{2.5}$$

The $\pm$ sign denotes the conduction and the valence bands respectively. $\mathbf{k}$ is measured from the Γ point of the first Brillouin zone, as shown in Fig. 2.1(b). These bands touch each other at the corner points of the Brillouin zone, and when graphene is neutral the contact points coincide with the Fermi energy. The dispersion relation starts out linearly from these points. By including the next-nearest neighbour hopping term, the conduction and the valence band become asymmetric, the low-energy spectrum does not change considerabely. As we are interested in the low-energy regime, we only retain terms with t in the following.

One can achieve further simplification by expanding the Fourier transformed tight-binding Hamiltonian around both K and K', as was done by Semenoff in Ref. [137].

We recover the famous Hamiltonian

$$\hat{H}^{\xi}_{\mathrm{G}} = \hbar v_F[\xi q_x \sigma_x + q_y \sigma_y], \tag{2.6}$$

here v_F is the Fermi velocity and $\mathbf{q}$ is measured from either cone K ($\xi = 1$) or K' ($\xi = -1$), these points are also referred to as valleys.[1] Remarkably, the time-independent Schrödinger equation corresponding to the Hamiltonian in Eq. 2.6 is formally identical with the Dirac equation of massless particles, therefore K and K' points are usually called Dirac points, and it is in this context that one can call the electrons of graphene as massless Dirac electrons. The linear dispersion relation and the two-component spinorial eigenfunctions are

$$\epsilon^{\mathrm{G}}(\mathbf{q}) = \pm\hbar v_F q, \tag{2.7}$$

$$\Phi^{\mathrm{G},\xi=1}_{\mathbf{q}}(\mathbf{r}) = \frac{e^{i\mathbf{qr}}}{\sqrt{2}} \begin{pmatrix} e^{-i\vartheta/2} \\ \pm e^{i\vartheta/2} \end{pmatrix}, \quad \Phi^{\mathrm{G},\xi=-1}_{\mathbf{q}}(\mathbf{r}) = \frac{e^{i\mathbf{qr}}}{\sqrt{2}} \begin{pmatrix} e^{i\vartheta/2} \\ \pm e^{-i\vartheta/2} \end{pmatrix}. \tag{2.8}$$

Here $q = |\mathbf{q}|$ and $\vartheta = \arctan(q_x/q_y)$. Note that the above expansion is valid if the wave vector $|\mathbf{q}| \ll |\mathbf{K}| \sim 1/a$, where a is the lattice constant. This gives a huge $\approx$ 24eV cutoff in energy.

The components of this spinorial wavefunction may be identified as components of a pseudospin. The first component that represents sublattice A is now interpreted as the *up spin*, denoted as $\Uparrow$, the second component (sublattice B) is similarly interpreted as the *down spin* ($\Downarrow$). Note that this pseudospin appears due to the two sublattices and is independent of the real spin of the electrons.[2]

As an experimental outlook we mention that the angle-resolved photoemission spectroscopy (ARPES), which directly resolves the electronic structure of the material in energy-momentum space, made it possible to directly observe the conical dispersion

[1] We use the (A, B) basis in both cones for further computational ease. It is costumory to use the (B, A) basis in K', which may be reached from the present form by a unitary transformation $U = i\sigma_x$.

[2] It is common practice to describe the eigenfunctions in Eq. 2.8 with their helicity. The helicity operator, which is the projection of the momentum operator along the spin direction, is defined for graphene in Ref. [48] and [111]. One finds that $\Phi^{\mathrm{G},\xi=1}_{\mathbf{q}}$ and $\Phi^{\mathrm{G},\xi=-1}_{\mathbf{q}}$ have well-defined helicity, they are eigenfunctions of the helicity operator. Note that in the ultra-relativistic limit the helicity operator coincides with chirality operator, therefore one may also say that Dirac electron has well-defined chirality, the notion chiral electrons is also frequently used. A related issue is that the Berry's phase of massless electrons of graphene is π, for detailed derivation see Ref. [167].

relation, the deviation from the predictions of the single-particle picture shed light on possible interaction effects, including velocity renormalization, see [22]. Scanning tunnelling spectroscopy (STS) measurements provides direct access to the density of states, one of the first reliable STS measurement is made by Li *et al.* in Ref. [85].

2.2.3 Graphene in Perpendicular Magnetic Field

In this subsection we consider a graphene sheet in perpendicular magnetic field $\mathbf{B} = (0, 0, B)$. As we are concentrating on the low-energy regime, it is convenient to take the Hamiltonian in Eq. 2.6 as our starting point, which describes the Dirac cones around K and K'. In a magnetic field, the appropriate Hamiltonian is deduced from Eq. 2.6 by minimal coupling. Here and hereafter if is is explicity not stated differently we use the Landau gauge $\mathbf{A} = (A_x, A_y, A_z) = (-yB, 0, 0)$. We denote the momentum after minimal coupling by $\mathbf{p}$, thus in our particular gauge choice $\mathbf{p} = (p_x, p_y) = (q_x + eA_x/\hbar, q_y + eA_y/\hbar) = (q_x - y/\ell^2, q_y)$. Then the Hamiltonian becomes:

$$\hat{H}^{\xi}_{\mathrm{G}} = \hbar v_F[\xi p_x \sigma_x + p_y \sigma_y] = \hbar v_F[\xi(q_x - \frac{y}{\ell^2})\sigma_x + q_y \sigma_y]. \tag{2.9}$$

The eigenvalues and eigenfunctions of this Hamiltonian is derived by McClure in [94] and the derivation is reproduced in App A in great detail. The LLs are

$$\epsilon^{\mathrm{G}}_n = \mathrm{sgn}(n)\sqrt{2|n|}\frac{v_F\hbar}{\ell}, \tag{2.10}$$

note the unusual energy spectrum that scales as $\sqrt{n}$ and with $\sqrt{B}$.

The corresponding eigenfunctions in cone $\xi = 1$ reads

$$\Phi^{\mathrm{G},\xi=1}_{|n|,k}(x, y) = \frac{1}{\sqrt{2}}\frac{e^{ikx}}{\sqrt{2\pi}}\begin{pmatrix}\mathrm{sgn}(n)\phi_{|n-1|}(y - k\ell^2)\\ -\phi_{|n|}(y - k\ell^2)\end{pmatrix}, \tag{2.11}$$

similarly in cone $\xi = -1$

$$\Phi^{\mathrm{G},\xi=-1}_{|n|,k}(x, y) = \frac{1}{\sqrt{2}}\frac{e^{ikx}}{\sqrt{2\pi}}\begin{pmatrix}\phi_{|n|}(y - k\ell^2)\\ \mathrm{sgn}(n)\phi_{|n-1|}(y - k\ell^2)\end{pmatrix}, \tag{2.12}$$

where $\phi_n(y)$ is the harmonic oscillator function.

Shubnikov-de Haas and integer QH measurements can be used to directly access the unique Landau level structure. In Ref. [114] Novoselov *et al.* identified the quantum Hall plateaus in Hall conductivity σ_{xy}. As opposed to the conventional 2DEG with plateaus at $\sigma_{xy} = 2n\frac{e^2}{h}$, in graphene the quantum Hall plateaus appear at $\sigma_{xy} = 2(2n+1)\frac{e^2}{h}$, that is when the filling factor is $\nu = 2(2n+1)$, with n integer. The fourfold degeneracy of the LLs comes from the spin and valley-pseudospin. This unusual QHE is a fingerprint of graphene, this made its identification possible.

A further branch of measurements, which directly probe the special LL structure, is magnetospectroscopy, these measurements are reviewed in chapter 3. A detailed review on graphene spectroscopy is given in Ref. [12].

2.2.4 Relativistic Properties of Massless Fermions in Graphene

Graphene hosts *relativistic* electrons moving with the Fermi velocity v_F instead of the speed of the light c. This subsection is devoted to show how the machinery of relativistic quantum mechanics can be used to deduce elementary properties of the material, e.g. the LL spectrum, when graphene is placed in a perpendicular magnetic and in-plane electric field.[3]

Consider the in-plane electric field $\mathbf{E} = (0, -E_\parallel, 0)$. The corresponding scalar potential $\phi = E_\parallel y$. We use Landau gauge given previously. The Hamiltonian of electrons in graphene under these circumstances is

$$\hat{H}^{\xi}_{\mathrm{E}_\parallel} = \hbar v_F[\xi p_x \sigma_x + p_y \sigma_y] - eE_\parallel y \sigma_0 \tag{2.13}$$

The eigenvalue problem may be solved algebraically following Peres [122], but here we reproduce the solution of Lukose *et al.*, see [87]. Their procedure is based on the

[3]The relativistic nature of the electrons in graphene manifest itself in many other ways. Consider the scattering of chiral electrons by a square potential. Using the wavefunction in Eq. 2.8 one can calculate the probability that a chiral electron transmits the barrier, see Ref. [67]. With normal incidence, the transmission is identically 1, independent of the barrier width, that is the barrier is transparent and the backscattering is absent. This is the manifestation of the Klein paradox in graphene. Using extremely narrow graphene heterostructures Young and Kim in Ref. [169] observed the Klein paradox in a condensed matter system. A related relativistic phenomenon is the so called Zitterbewegung, which has been discussed theoretically in Ref. [31] and [68], but no experiments are available up to now.

covariance of the Dirac equation corresponding to the Hamiltonian in Eq. 2.13. One can boost from the laboratory frame R to another frame of reference R' in such a way that in the R' frame the electric field vanishes and the magnetic field is rescaled. In the R' frame the solution of the eigenvalue problem of the transformed Hamiltonian is readily given. The solution of the original problem may be found by applying the inverse Lorentz transformation, that is we need to boost back the eigenvalues and eigenvectors to the lab frame R.[4] For this we introduce contravariant and covariant coordinate vectors and the metric tensor following the notations of Ref. [53]:

$$x^{\mu} = (v_F t, x, y), \qquad x_{\mu} = (v_F t, -x, -y), \qquad g_{\nu\mu} = \begin{pmatrix} 1 & 0 & 0 \\ 0 & -1 & 0 \\ 0 & 0 & -1 \end{pmatrix}.$$

We also introduce here the Lorentz transformation rules between the lab frame R and the coordinate system R'. All covariant and contravariant quantities transform in the same way as the particular components of the coordinate three vector:

$$x'^{\mu} = \Lambda^{\mu}_{\nu}\, x^{\nu}, \qquad x'_{\mu} = (\Lambda^{-1})^{\nu}_{\mu}\, x_{\nu}.$$

Here Λ (Λ^{-1}) is the (inverse) Lorentz transformation. For further use we introduce also the following notations for the momentum, the gradient operator, and the vector potential respectively:

$$p^{\mu} = (\frac{\epsilon}{v_F}, \hbar k_x, \hbar k_y), \qquad \partial^{\mu} = \frac{\partial}{\partial x_{\mu}} = (\frac{1}{v_F}\frac{\partial}{\partial t}, -\frac{\partial}{\partial x}, -\frac{\partial}{\partial y}),$$
$$A^{\mu} = (\frac{\phi}{v_F}, A_x, A_y) = (\frac{E_{\parallel} y}{v_F}, -yB, 0).$$

Setting down the notation, we start with the time dependent Schrödinger equation corresponding to the Hamiltonian 2.13 with the choice of $\xi = 1$ (cone K). By applying the notation introduced above and by multiplying the Schrödinger equation by σ_z we

[4] We emphasize that in the Lorentz boost we apply v_F appears instead of the speed of light c.

arrive at the covariant form of the Dirac equation in the lab frame R:

$$-i\hbar v_F \gamma_\mu (\partial^\mu - \frac{ie}{\hbar} A^\mu)\Phi(x,y) = 0 \tag{2.14}$$

Here $\gamma_0 = \sigma_z \quad \gamma_1 = -\sigma_z\sigma_x \quad \gamma_2 = -\sigma_z\sigma_y$.[5] We are in the position to construct the appropriate Lorentz boost which should transform $A^\mu = (\frac{E_\parallel y}{v_F}, -yB, 0)$ in R to $A'^\mu = (0, -yB', 0)$ in R'. By straighforward algebra the Lorentz transformation turns out to be

$$\Lambda = \begin{pmatrix} \cosh\zeta & \sinh\zeta & 0 \\ \sinh\zeta & \cosh\zeta & 0 \\ 0 & 0 & 1 \end{pmatrix} \tag{2.15}$$

where we introduced the rapidity or boost parameter ζ as $\tanh\zeta = \beta = E_\parallel/(v_F B) > 0$ and $\lambda = \sqrt{1-\beta^2}$. Notice that β is the ratio of the usual drift velocity $E_\parallel/B$ and the Fermi velocity v_F. The rescaled magnetic field B' becomes $B' = \lambda B$, while the magnetic length rescales as $\ell' = \ell/\sqrt{\lambda}$. By construction, the Hamiltonian $\hat{H}' = \hbar v_F[(q_x - y/\ell'^2)\sigma_x + q_y\sigma_y]$ has a simple form, its eigenstates and eigenvalues has been given in Eq. 2.10 and 2.11, though here we shall use the rescaled magnetic length ℓ'.

Knowing the eigenvalue spectrum in R', that is ϵ'_n, we apply an inverse boost Λ^{-1} on the momentum three vector $p'^\mu = (\epsilon'_n/v_F, \hbar k'_x, \hbar k'_y)$ and solve the equation system to ϵ_n. Then we recover the energy spectrum inframe R:

$$\epsilon_n^{\mathrm{E}_\parallel} = \mathrm{sgn}(n)\sqrt{2|n|}\frac{\hbar v_F}{\ell}\lambda^{3/2} - \hbar k\beta v_F \tag{2.16}$$

Note that the LL spectrum is squeezed as compared to the case without electric field.

The above system of equations is used to determine the argument of the wavefunctions. However, for the wavefunction in the frame R we need to construct the matrix S, which represents the Lorentz boost in spinor space as $S\Phi = \Phi'$. Making the usual assumption that the γ_μ matrices have the same form in all frames and that S satisfies $S^{-1}\gamma_\mu S = (\Lambda^{-1})^\nu_\mu \gamma_\nu$ (see [53]), we get $S = \exp(\frac{\zeta}{2}\sigma_x)$. After the application of S^{-1} and

[5] The γ_μ matrices fulfill the requirement that γ_0 is Hermitian and unitary, while $\gamma_{1\backslash 2}$ are both anti-Hermitian and unitary. Moreover, they also fulfill the commutation relation $\gamma_\nu\gamma_\tau + \gamma_\tau\gamma_\nu = 2g_{\nu\tau}\sigma_0$ [53], that is they satisfy the Clifford algebra.

proper normalisation the wavefunction becomes for $n \neq 0$:

$$\Phi_{n,k}^{\xi=1}(\mathbf{r}) = \frac{1}{\sqrt{4(1+\lambda)}} \left[\begin{pmatrix} -\beta \\ 1+\lambda \end{pmatrix} \phi_{n,k}(\mathbf{r}) + \begin{pmatrix} -1-\lambda \\ \beta \end{pmatrix} \mathrm{sgn}(n) \phi_{n-1,k}(\mathbf{r}) \right], \tag{2.17}$$

while for the $n = 0$ Landau level,

$$\Phi_{0,k}^{\xi=1}(\mathbf{r}) = \frac{1}{\sqrt{2(1+\lambda)}} \begin{pmatrix} -\beta \\ 1+\lambda \end{pmatrix} \phi_{0,k}(\mathbf{r}). \tag{2.18}$$

We have used the subformulas

$$\phi_{n,k}(\mathbf{r}) = \frac{e^{ikx}}{\sqrt{2\pi}} \frac{\lambda^{1/4}}{(2^{|n|}|n|!\sqrt{\pi}\ell)^{1/2}} e^{-\mathrm{Y}_n^2/2} H_{|n|}(\mathrm{Y}_n) \tag{2.19}$$

and

$$\phi_{n-1,k}(\mathbf{r}) = \frac{e^{ikx}}{\sqrt{2\pi}} \frac{\lambda^{1/4}}{(2^{|n-1|}|n-1|!\sqrt{\pi}\ell)^{1/2}} e^{-\mathrm{Y}_n^2/2} H_{|n-1|}(\mathrm{Y}_n), \tag{2.20}$$

with the argument

$$\mathrm{Y}_n = \sqrt{\lambda} y/\ell - \sqrt{\lambda}\ell k - \beta\sqrt{2|n|}\mathrm{sgn}(n). \tag{2.21}$$

Notice that Y_n depends on both the LL index (including its sign). Also, it is identical for the $\phi_{n,k}$ and $\phi_{n-1,k}$ parts of $\Phi_{n,k}^{\xi=1}$ in Eq. 2.17.

From Eq. 2.13 one can derive the eigenvalues and eigenfunctions for cone K' ($\xi = -1$) in a similar manner. Note that the electric field does not change sign in cone K'. The eigenvalues are identical with that of cone K in Eq. 2.16, while the wavefunction differs. For $n \neq 0$ in cone $\xi = -1$, the orbitals are

$$\Phi_{n,k}^{\xi=-1}(\mathbf{r}) = \frac{1}{\sqrt{4(1+\lambda)}} \left[\begin{pmatrix} 1+\lambda \\ \beta \end{pmatrix} \phi_{n,k}(\mathbf{r}) + \begin{pmatrix} \beta \\ 1+\lambda \end{pmatrix} \mathrm{sgn}(n) \phi_{n-1,k}(\mathbf{r}) \right], \tag{2.22}$$

while for the $n = 0$,

$$\Phi_{0,k}^{\xi=-1}(\mathbf{r}) = \frac{1}{\sqrt{2(1+\lambda)}} \begin{pmatrix} 1+\lambda \\ \beta \end{pmatrix} \phi_{0,k}(\mathbf{r}). \tag{2.23}$$

2.3 Bilayer Graphene

Bilayer graphene has also been the focus of intense research since its first experimental identification due to the fact that its band structure is entirely different from graphene Novoselov *et al.* in Ref. [115] measured the quantum Hall conductivity σ_{xy}, and found plateaus at $\sigma_{xy} = \pm 4n\frac{e^2}{h}$ with $n \geq 1$. This sequence of fourfold degenerate LLs and an eightfold degenerate central Landau band is a fingerprint of bilayer graphene. The fourfold degeneracy comes from spin and valley pseudospin, while the additional degeneracy of the central Landau band is due to the degeneracy of $n = 0$ and $n = 1$ LLs. Similar QH measurements at $\nu = \pm 4, \pm 8$ derived the activation gap, see Ref. [79]. In Ref. [56] Henriksen *et al.* measured the cyclotron resonance via IR absorption spectroscopy and provided an experimental confirmation of the peculiar magnetic field dependence of the LL spectrum characteristic to bilayer graphene. A related magneto-Raman experiment is presented in Ref. [39]. Other measurements, such as compressibility measurements are also available for bilayer graphene for both zero and non-zero magnetic field, reinforcing the single-particle picture, see Ref. [58].[6]

The peculiar Landau level structure of these chiral fermions with Berry's phase 2π were discussed in great detail by several authors in [54],[93], [92], [121], [173], and a detailed review is found in [37].

In bilayer graphene two single layers of graphene are coupled together through van der Waals forces, the distance between the two layers being 3.37 Å. The structure of bilayer graphene is shown in Fig. 2.2. Each layer consists of two sublattices, denoted A and B in the top layer and $\widetilde{A}$ and $\widetilde{B}$ in the bottom layer. In Bernal stacking [15] two sublattices, $\widetilde{A}$ and B in our notation, are exactly above/below one another, while the A sites are above the center of the hexagons in the bottom layer, and $\widetilde{B}$ sites are below the centers of hexagons in the top layer.

The low-energy physics of bilayer graphene can be adequately described by the tight-binding effective theories that specialize the Slonczewski-Weiss-McClure (SWM) model of graphite to the case of just two layers, see Ref. [95], [141] and [159]. In the

[6] As a side note we mention that the bandgap is tunable by applied electric field, as was revealed in Ref. [172], who directly observed this with infrared spectroscopy. Similar measurements were conducted in [26], [**?**], [90] with related theoretical work available in Ref. [2], [107], [160]. The band gap can also be tuned by selectively controlling the carrier concentration in each layer, see [116].

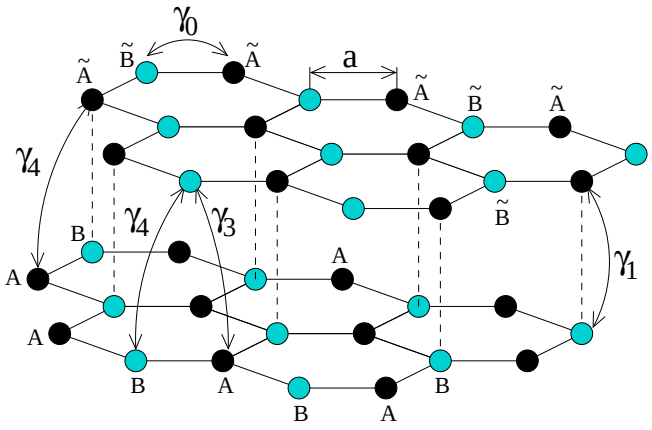

Figure 2.2: Bilayer graphene in Bernal stacking. The hopping parameters of the Slonczewski-Weiss-McClure model, conventionally denoted γ_0, γ_1, γ_3 and γ_4, are also indicated.

vicinity of the inequivalent corners of the hexagonal first Brillouin zone K ($\xi = 1$) and K' ($\xi = -1$) this amounts to using the Hamiltonian in Ref. [54] and [92]:

$$\hat{H}_{\mathrm{B}}^{\xi} = \xi \begin{pmatrix} \frac{u-\Delta'}{2} & v_3\pi & -v_4\pi^\dagger & v\pi^\dagger \\ v_3\pi^\dagger & -\frac{u+\Delta'}{2} & v\pi & -v_4\pi \\ -v_4\pi & v\pi^\dagger & -\frac{u-\Delta'}{2} & \xi\gamma_1 \\ v\pi & -v_4\pi^\dagger & \xi\gamma_1 & \frac{u+\Delta'}{2} \end{pmatrix} - \Delta_Z\sigma_z, \tag{2.24}$$

where $\pi = \hbar p_x + i\hbar p_y$ and $\mathbf{p} = (p_x, p_y) = -i\nabla - e\mathbf{A}/\hbar$ as introduced previously.

The diagonal of the Hamiltonian contains Δ', which is the on-site energy difference between the dimer sites $(\widetilde{A}, B)$ and the non-dimer sites $(\widetilde{B}, A)$. u is the potential energy difference between the layers, which may arise, e.g., because of an applied perpendicular electric field $E_\perp$.

In the non-diagonal elements one can readily identify various SWM hopping terms that are relevant in the bilayer case. First, $\gamma_0 = \gamma_{AB} = \gamma_{\widetilde{A}\widetilde{B}}$ is the intra-layer hopping amplitude, the corresponding intra-layer velocity is $v = \sqrt{3}a\gamma_0/2\hbar \approx 10^6$ m/s. Second, $\gamma_1 = \gamma_{\widetilde{A}B}$ is the interlayer hopping amplitude between sites above each other in the two layers. Third, $\gamma_3 = \gamma_{A\widetilde{B}}$ is the next-nearest-neighbour interlayer hopping amplitude, the related velocity is $v_3 = \sqrt{3}a\gamma_3/2\hbar$, which is also referred to as the trigonal warping parameter. Finally, $\gamma_4 = \gamma_{A\widetilde{A}} = \gamma_{B\widetilde{B}}$ is the interlayer next-nearest neighbour hopping

amplitude, and the related velocity is $v_4 = \sqrt{3}a\gamma_4/2\hbar$.

Note that the Hamiltonian acts in the basis of sublattice Bloch states $(A, \widetilde{B}, \widetilde{A}, B)$ in valley K and $(\widetilde{B}, A, B, \widetilde{A})$ in valley K'. Note also that the second term of the Hamiltonian $\Delta_Z = g\mu_B B$ is the Zeeman energy with g being the gyromagnetic factor, this term acts on the spin space.

The Hamiltonian in Eq. 2.24 is block-diagonal in the valley index, which is conveniently described as a pseudospin. In the special case $u = 0$ the system has SU(2) pseudospin rotation symmetry. In the theoretical limit $\Delta_Z \to 0$ this is raised to SU(4) symmetry. Throughout our subsequent analysis of bilayer graphene presented in Chap. 5 we will treat Δ_Z and u as small perturbations in comparison to the interaction energy, i.e., we will work in the $\Delta_Z, u \ll e^2/(4\pi\epsilon_0\epsilon_r\ell)$ limit.

Following the derivation of McCann *et al.* in [92] we introduce a 2×2 effective Hamiltonian instead of Eq. 2.24, acknowledging that this approximation is valid for small momenta, $p \ll \gamma_1/4v$:

$$\hat{H}^{\xi}_{\mathrm{B,\ eff.}} = -\frac{v^2}{\gamma_1}\begin{pmatrix} 0 & (\pi^\dagger)^2 \\ \pi^2 & 0 \end{pmatrix} + \xi v_3 \begin{pmatrix} 0 & \pi \\ \pi^\dagger & 0 \end{pmatrix} + \frac{\xi u}{2}\begin{pmatrix} 1 & 0 \\ 0 & -1 \end{pmatrix} - \frac{v^2\xi u}{\gamma_1^2}\begin{pmatrix} \pi^\dagger\pi & 0 \\ 0 & -\pi\pi^\dagger \end{pmatrix}, \tag{2.25}$$

Note that $\hat{H}^{\xi}_{\mathrm{B,\ eff.}}$ acts on $(A, \widetilde{B})$ in valley K and $(\widetilde{B}, A)$ in valley K'. Note also that as a further approximation we neglect v_3. Then the Landau levels and Landau orbitals, respectively, of the two-band Hamiltonian $\hat{H}^{\xi}_{\mathrm{B,\ eff.}}$ become

$$\epsilon^{\mathrm{B}}_{0,\xi} = \frac{\xi u}{2}, \quad \epsilon^{\mathrm{B}}_{1,\xi} = \frac{\xi u}{2} - \xi\frac{u\hbar\omega_c}{\gamma_1}, \quad \epsilon^{\mathrm{B}}_{n,\xi} = \mathrm{sgn}(n)\hbar\omega_c\sqrt{|n|(|n|-1)} - \xi\frac{u\hbar\omega_c}{2\gamma_1}, \tag{2.26}$$

$$\Phi^{\mathrm{B},\xi}_{0,k} = \begin{pmatrix} \phi_{0,k}(\mathbf{r}) \\ 0 \end{pmatrix}, \quad \Phi^{\mathrm{B},\xi}_{1,k} = \begin{pmatrix} \phi_{1,k}(\mathbf{r}) \\ 0 \end{pmatrix}, \quad \Phi^{\mathrm{B},\xi}_{n,k} = \begin{pmatrix} A^{(n)}_\xi \phi_{|n|,k}(\mathbf{r}) \\ B^{(n)}_\xi \phi_{|n|-2,k}(\mathbf{r}) \end{pmatrix}, \tag{2.27}$$

$$A^{(n)}_\xi = \frac{1}{C^{(n)}_\xi}, \quad B^{(n)}_\xi = \frac{1}{C^{(n)}_\xi}\frac{\epsilon^{\mathrm{B}}_{n,\xi} - \xi\frac{u}{2} + \xi\frac{u|n|\hbar\omega_c}{\gamma_1}}{\hbar\omega_c\sqrt{|n|(|n|-1)}}.$$

Here $n \neq -1$ is an integer, $C^{(n)}_\xi$ is an appropriate normalization factor, and $\phi_{n,k}(\mathbf{r})$ are the single-particle states in the conventional 2DEG given in Eq. 2.3. We have also introduced $\omega_c = 2eBv^2/\gamma_1$. The $n = 0, 1$ orbitals are degenerate in the $u \to 0$ limit, and they have a layer polarization for $\xi = \pm 1$. At realistic values of Δ_Z and u, the

$n = 0, 1$, $\xi = \pm 1$, $\sigma = \uparrow, \downarrow$ states form a quasidegenerate band we have already called the central Landau level octet. Notice that $A_\xi^{(n)} \to 1/\sqrt{2}$ and $|B_\xi^{(n)}| \to 1/\sqrt{2}$ for $u \to 0$.

In the remaining part of the section we would like to determine to what extent the simplified two-band model $\hat{H}^\xi_{\mathrm{B,\,eff.}}$ in Eq. 2.25 is adequate for the description of the low-energy band structure instead of the the four-band Hamiltonian $\hat{H}^\xi_{\mathrm{B}}$ in Eq. 2.24. Our goal is to systematically explore the range of applicability of this simplified model, which neglects several parameters of the SWM model, notably γ_3, γ_4, and Δ'. Therefore we calculate the eigenvalues of the Hamiltonian in Eq. 2.24 numerically, and test how the eigenvalues are modified by tuning the neglected parameters $\gamma_3 = \gamma_4 = \Delta' = 0$ from zero to their literary values.

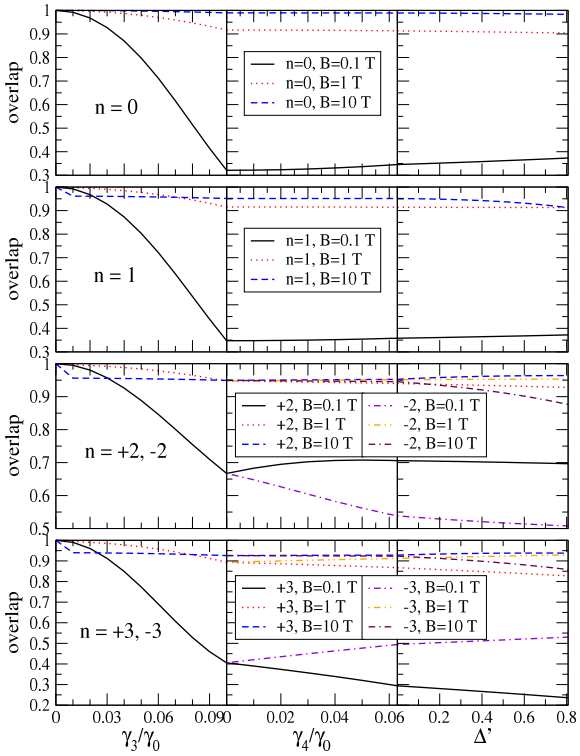

Figure 2.3: The overlap of the Landau orbitals with the *ideal* limit, $\gamma_3 = \gamma_4 = \Delta' = 0$, as the SWM parameters $\gamma_3, \gamma_4, \Delta'$ are gradually tuned from zero to their literary values [Eqs. 2.28 to 2.29] for the lowest-energy Landau levels. For the effect of γ_3 in the two-band model see Ref. [97].

First, we review the available estimates of these parameters. Their values were estimated by a combination of infrared response analysis and theoretical techniques by

Zhang *et al.* in [171]. They found

$$\frac{\gamma_1}{\gamma_0} = 0.133, \quad \frac{\gamma_3}{\gamma_0} = 0.1, \quad \frac{\Delta'}{\gamma_0} = 0.006. \tag{2.28}$$

These ratios are based on $\gamma_0 = 3.0$ eV. While somewhat greater values of γ_0 are also available in the literature, see [81], we use these values for the robustness of the analysis. For the particle-hole symmetry breaking term we use

$$\frac{\gamma_4}{\gamma_0} = 0.063 \tag{2.29}$$

from the recent electron and hole mass measurement by Zou *et al.* in [175], which is slightly greater than the value in Ref. [171].

With $\pi = \frac{\sqrt{2}\hbar}{i\ell}a$, $[a, a^\dagger] = 1$, the Hamiltonian can be expressed in terms of these Landau level ladder operators. Then the eigenstates of $\hat{H}_{\mathrm{B}}^{\xi}$ can be calculated numerically. Fig. 2.3 shows the overlap of the Landau orbitals with the *ideal* limit $\gamma_3 = \gamma_4 = \Delta' = 0$ as the SWM parameters $\gamma_3, \gamma_4, \Delta'$ are tuned from zero to their literary values [Eqs. 2.28 to 2.29] for the central ($n = 0, 1$) and the two pairs of nearby ($n = \pm 2, \pm 3$) Landau levels. At small magnetic field $B = 0.1$ T trigonal warping alone significantly changes the orbitals from their ideal limit. Switching on γ_4 hardly affects the central levels, but for $n \geq 2$ it changes the electron and hole pairs $(+n, -n)$ differently, as expected from this electron-hole symmetry breaking term. Finally, the inclusion of Δ' hardly affects the orbitals. These changes, however, are already small at modest fields ($B = 1$ T), and are further suppressed as the experimentally relevant range ($B \approx 10$ T) is approached. Thus neglecting the $\gamma_3, \gamma_4, \Delta'$ SWM parameters is justified in the high magnetic field range where quantum Hall experiments are typically performed.

As the two-band model in Eq. 2.25 applies for small momenta, and the low-index Landau orbitals have a small amplitude at high momenta, the two-band model is expected to be valid for the lowest few Landau levels. The Landau orbitals of the two-band model have a large overlap with those of the four-band model in the *ideal* limit $\gamma_3 = \gamma_4 = \Delta' = 0$: 1, 0.9995, 0.9992, 0.9987 for $n = 0, 1, \pm 2, \pm 3$, respectively. We conclude that using the Landau states of two-band model in Eq. 2.25 instead of those of the four-band model $\hat{H}_\xi$ in the lowest-energy Landau bands does not introduce

further inaccuracy beyond the neglect of γ_3, γ_4, and Δ'. Therefore, we take $\hat{H}^{\xi}_{\mathrm{B,\,eff.}}$ as our starting point for the analysis of Chap. 5.

With the view of the fourfold degenerate LLs and a peculiar eightfold degenerate central Landau band, the question of lifting the degeneracy naturally arises, which would lead to the appearence of symmetry breaking quantum Hall ferromagnetic (QHF) states. The observation of these broken symmetry states at integer filling factors is the center of discussion in chapter 5, where we discuss both theoretical predictions and experimental measurements.

We also note that beyond the single-particle picture, the effect of electron-electron interaction is the scope of today's investigation. Here we only refer to excellent reviews [12] and [78] on the topic, and postpone the detailed discussion of many-body effects in graphene to Chapter 5, where we examine how the cyclotron resonance is modified due to electron-electron interactions in bilayer graphene.

2.4 Organic Quasi-2D Materials - the α-(BEDT-TTF)$_2$I$_3$

2.4.1 Material Properties and Zero-Gap State in α-(BEDT-TTF)$_2$I$_3$

The layered organic conductor α-(BEDT-TTF)$_2$I$_3$ is the most intensively investigated member of the (BEDT-TTF)$_2$I$_3$ family. This organic compound was first synthesized in the 80's, see [14], it has been in the scope of general interest due to its surprisingly rich phase diagram. For reviews, see [109], [151] and [153]. Fig. 2.4(a) shows a BEDT-TTF molecuce, while panel (b) shows how the molecules are arranged in the unit cell. The crystal consists of conductive BEDT-TTF [where BEDT-TTF stands for bis(ethylene-dithio)tetrathiafulvalene] layers which are separated by insulating I_3^- layers. As the layers are weakly coupled to each other, the material has a quasi-two-dimensional character, confirmed in ab initio calculations in Ref. [61]. One of the most striking feature of the material is the appearance of Dirac cones in the low-energy band structure under hydrostatic pressure above 15 kbar or under uniaxial

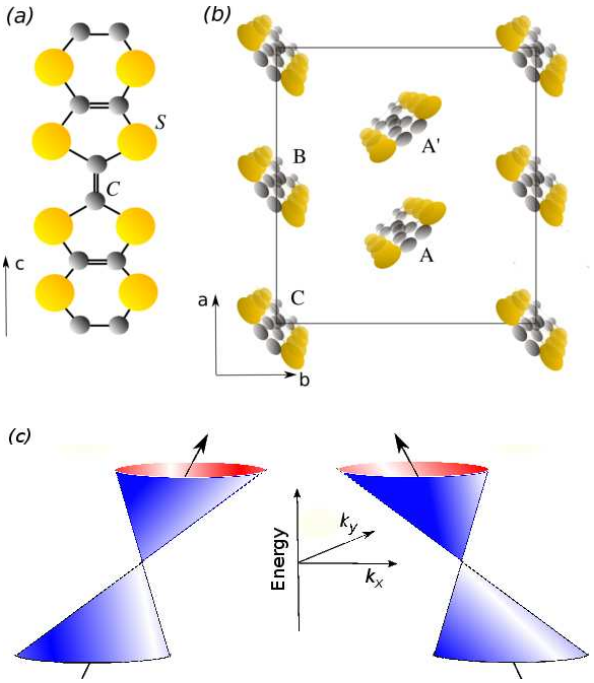

Figure 2.4: (Color online) Organic compound α-(BEDT-TTF)$_2$I$_3$. (a) Molecule (BEDT-TTF) that consists of carbon (C) and sulfur (S) atoms. (b) Arrangement of the four molecules (A, A', B, and C) in the unit cell of a single layer (*ab*-plane). (c) Sketch of the low-energy band structure in the vicinity of the Fermi level that has the form of two tilted Dirac cones. The cones are tilted in the k_x direction.

strain above 3 kbar, see [148], [149] and [152]. Here we will first review the experimental findings that confirm the existence of Dirac cones, then give a short summary on the available theoretical works.

Most importantly, transport measurements are available for this material, demonstrating that the conductivity parallel to the layers is constant from room temperature down to 2K, while both the carrier density and the mobility changes several orders of magnitude in opposite directions. This behaviour was partially documented in early measurements, see [65], and later elaborated in Ref. [148], [149] and [151]. The interpretation of these findings in terms of the zero-gap state was proposed in several theoretical works, [69], [75], in addition ab initio calculations also confirmed the existence of Dirac cones, see [3], [74].

Another class of experimental investigations considers interlayer magnetoresistance, which decreases with increasing perpendicular magnetic field, and shows a complex behaviour with the angle between the magnetic field and the sample, see Ref. [136]

and [152]. These experimental results are nicely explained in related theoretical studies of the resistivity tensor components within the Dirac cone picture, see [105], [118] and [119]. The interlayer magnetoresistance measurements made it possible to directly observe the $\sqrt{B}$ behaviour of the LL spectrum, see [147].

Finally, the observation of Shubnikov-de Haas (SdH) oscillations and integer quantum Hall plateaus are reported in Ref. [154]. The idea of Tajima *et al.* is to fix the aI3 crystal to a substrate in such a manner that makes a few of the BEDT-TTF layers close to the substrate significantly hole doped. In the experimental realization the extent of doping decreased rapidly with distance from the substrate, which made only two layers effectively doped. Both of these differently doped layers contributed independently to the transport, giving rise to the observed SdH oscillations and QH plateaus.[7]

Experimental works include ab initio calculations in Ref. [3], [74], which confirmed the presence of massless fermions in the material. Besides, extended Hubbard model calculations were developed by several authors, see [59], [69], [70], [71] and [75], as well as tight-binding model calculations appeared concerning aI3 and related layered organic compounds, see [102], [103], [104]. According to theory Dirac points may occur at ambient pressure above the metal to insulator transition, however hydrostatic pressure or strain suppresses the phase transition to lower temperature and stabilize the Dirac points. At even higher pressure or strain the Dirac points coalesce at a high-symmetry Γ point of the Brillouin zone where a gap opens, see [99], [100]. As was discussed by Mori in Ref. [103], the Dirac points appear at low-symmetry, time-reversal related points, with non-stripe charge order.

To conclude this section, we have shown through various experiments and theoretical works that at high pressure or high strain massless Dirac fermions similar to graphene occur in α-(BEDT-TTF)$_2$I$_3$. In the next subsections we highlight the differences of the the Dirac cone in this organic compound with respect to graphene and also discuss the open questions about the low-energy band structure of the material.

[7]Note however, that this interpretation is not the only possible one. Instead of interpreting the two characteristic frequencies of the SdH oscillations in terms of the two differently doped layers, one can also speculate that different carriers, e.g. massive and massless ones might lead to the observed peculiar SdH oscillations and QH pattern. Our efforts to give such a consistent interpretation were not fruitful, as the number of observed plateaus and SdH oscillation maxima is not enough to draw a conclusive picture. More precise measurement is needed before far-reaching conclusions are drawn.

2.4.2 Tight-Binding Description of the Conical Bands

α-(BEDT-TTF)$_2$I$_3$ is a three-dimensional crystal with triclinic crystal structure, containing conducting BEDT-TTF and insulating I_3^- anion layers. As confirmed by theory (Ref. [61]), this crystal has a strong 2D nature with negligible interlayer coupling, therefore it is costumary to regard each independent layer as a 2D crystal and develop a 2D model accordingly. The unit cell of the 2D model is oblique, with the primitive vectors enclosing an angle $\gamma \approx 90.8°$. The length of the primitive vectors change monotonically from $a \approx 9.1$ Å and $b \approx 10.8$ Å to $a \approx 8.6$ Å and $b \approx 10.35$ Å as the pressure is increased from ambient pressure to 17.6 kbar, see [77]. Fig. 2.5(a) shows a sketch of the unit cell containig four BEDT-TTF molecules, and panel (b) shows the first Brillouin zone with the distinguished points and directions we refer to later.

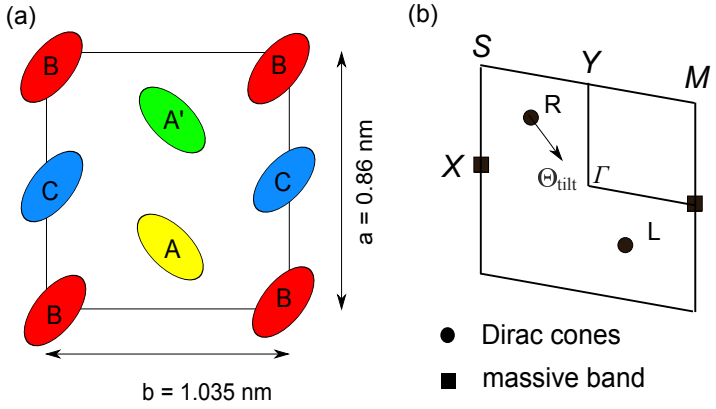

Figure 2.5: Schematic view of the unit cell (panel (a)) and the first Brillouin zone of aI3 (panel (b)). The high symmetry points, the location of the massive valley (squares), and that of the Dirac cones (dots) are indicated. The arrow from point R indicates the smallest steepness of cone R. Directions in the momentum plane will be related to this angle, θ_{tilt}.

The low-energy band structure can be derived from a tight-binding model that involves the four relevant highest occupied molecular orbitals of the four different BEDT-TTF molecules in the unit cell, see Ref. [47], [75]. Among the four bands, only the upper two play a role as the filling is 3/4 at charge neutrality [102]. These two bands have contact points at low-symmetry time-reversal related points L and R, the conical bands are anisotropic and tilted [74]. The massless Dirac carriers are suitably described

by the minimal Weyl Hamiltonian using four velocity parameters:

$$\hat{H}^{\xi}_{\mathrm{W}}(\mathbf{q}) = \xi\hbar[(v_0^x q_x + v_0^y q_y)\sigma_0 + v_x q_x \sigma_x + \xi v_y q_y \sigma_y] \tag{2.30}$$

where $\xi = 1$ ($\xi = -1$) represents the cone at R (L). This Hamiltonian obviously respects time-reversal symmetry, $\hat{H}^{\xi=1}_{\mathrm{W}}(\mathbf{q}) = [\hat{H}^{\xi=-1}_{\mathrm{W}}(-\mathbf{q})]^*$. It has spin-degenerate bands, but the dispersions in valleys $\xi = \pm 1$ differ. The inclination of the Dirac cone is determined by the combined effect of the tilt and the anisotropy. By the *anisotropy* of the Dirac cone we mean the difference between v_x and v_y, and we characterize it by parameter

$$\alpha = \sqrt{v_x/v_y}. \tag{2.31}$$

By its *tilt* we mean that the constant energy slices are not concentric because $(v_0^x, v_0^y) \neq (0, 0)$. For convenience, we will also use a rescaled and rotated coordinate system [105] defined by the transformation

$$\left.\begin{aligned} \tilde{q}_x &= q_x \cos\theta + \tfrac{q_y}{\alpha^2}\sin\theta \\ \tilde{q}_y &= -q_x \sin\theta + \tfrac{q_y}{\alpha^2}\cos\theta \end{aligned}\right\}. \tag{2.32}$$

The corresponding, transformed real-space coordinates $\tilde{\mathbf{r}} = (\tilde{x}, \tilde{y})$ are

$$\left.\begin{aligned} \tilde{x} &= x\cos\theta + \alpha^2 y \sin\theta \\ \tilde{y} &= -x\sin\theta + \alpha^2 y \cos\theta \end{aligned}\right\}. \tag{2.33}$$

Rescaling the q_y coordinate removes the anisotropy. The rotation brings the $\tilde{q}_x$ coordinate in the tilt direction if we choose

$$\cos\theta = \cos\theta_{\mathrm{tilt}} \equiv \frac{v_0^x v_y}{\sqrt{(v_0^y v_x)^2 + (v_0^x v_y)^2}}. \tag{2.34}$$

After some straightforward algebra and a unitary transformation, see [105], the Weyl Hamiltonian can be written as

$$\hat{H}^{\xi}_{\mathrm{W}}(\tilde{\mathbf{q}}) = \xi\hbar v_x[\beta\tilde{q}_x\sigma_0 + \tilde{q}_x\sigma_x + \xi\tilde{q}_y\sigma_y], \tag{2.35}$$

where we have introduced the dimensionless parameters

$$\beta = \sqrt{(v_0^x/v_x)^2 + (v_0^y/v_y)^2} \quad \text{and} \quad \lambda = \sqrt{1-\beta^2} \tag{2.36}$$

to quantify the tilt. Notice that $0 \leq \beta \leq 1$, and that $\beta = 0$ corresponds to the case of graphene. In the following we will work in the coordinate system introduced in Eq. 2.32. Fig. 2.4(c) depicts the oppositly tilted Dirac cones.

An open issue concerning the low-energy band structure of this crystal is the determination of the parameters β, α and θ_{tilt} describing the Dirac cones. Note that our knowledge of the geometry of the cones comes from theory, as the available, mainly transport, measurements are insensitive to the inclination or the anisotropy of the cones. In the literature several sets of parameters are available, see [70], [75], and their pressure dependence is also analysed in detail, see Ref. [59]. Motivated by these considerations, in Chap. 3 we present an analysis of the magneto-optical selection rules in this material, which might lead to an experimental indication for at least some of the parameter values. In Chap. 4, however, to illustrate the collective plasmon excitation in the system, we choose a representative set of parameters based on [75]. We emphasize that our results are robust and survive within a broad range of the parameter values.

Another open question of the low-energy band structure is that in addition to the linear valleys, there may be a band maximum at the time-reversal symmetric point X on the edge of the first Brillouin zone, which may host massive holes. The existence of a parabolic valley besides the linear ones is proposed by a recent ab initio calculation in Ref. [3] and experimentally verified by Monteverde *et al.* in Ref. [101]. In his article, Monteverde conducted magnetotransport experiments, identified both massive and massless carriers and deduced several quantities of interest, e.g. carrier densities for both types of carriers, the effective Fermi velocity of the massless carriers and the effective mass for the massive ones. Note, however, that his findings are not verified by additional transport measurements yet, thus we believe it is a timely issue to discuss such properties of the electron system in this material which in principle probe the existence of both carrier types. This leads us to the central idea of the *three-valley*

model discussed in Chap. 4.

2.4.3 Relativistic Covariance in α-(BEDT-TTF)$_2$I$_3$

In this subsection we derive the Landau level eigenstates and eigenfunctions of aI3 in a perpendicular magnetic field. This problem may be solved by an algebraic method presented in Ref. [105], nevertheless we utilize the relativistic covariance of the underlying Dirac equation similarly to Sec. 2.2.4. We draw a parallel between graphene in crossed electric and magnetic field and aI3, in the latter case the tilt plays a role essentially identical to that of the electric field in graphene. The same line of reasoning can be applied to any system with tilted Dirac cones, e.g. to the conical valleys realized on the surface of 3D topological insulators in a crossed electric and magnetic field, see Ref. [163]. There again, the LL eigenstates and eigenfunctions can be computed in complete analogy.

Consider the Hamiltonian in Eq. 2.35 in a perpendicular magnetic field with vector potential $\mathbf{A} = (-yB, 0, 0)$. The Schrödinger equation of the Hamiltonian Eq. 2.35 with the covariant notation introduced previously becomes

$$-i\hbar v_x \gamma_\mu (\partial^\mu - \frac{ie}{\hbar} A^\mu)\Phi(x,y) + i\hbar v_x \gamma_0 \beta \partial^x \Phi(x,y) = 0 \tag{2.37}$$

with $A^\mu = (\beta By, -yB, 0)$.

One can make the last term containing the derivative harmless by writing the ansatz for the wavefunction $\Phi(x,y) = e^{ikx}\psi(y)$. With this the Dirac equation becomes

$$-i\hbar v_x \gamma_\mu (\partial^\mu - \frac{ie}{\hbar} A^\mu)\Phi(x,y) + \gamma_0 \hbar v_x \beta k \Phi(x,y) = 0. \tag{2.38}$$

Comparing this Dirac equation with that of the graphene system in Eq. 2.14, we find the two equations are identical, if we replace v_x with v_F and equate the tilt parameter β of the Weyl system with the $\beta = E_\parallel / v_F B$ describing the quotient of the drift and Fermi velocity in graphene.[8] Note that precisely this correspondence made it possible

[8]Note, however, that the latter equation is valid in the rescaled and rotated coordinate system $\tilde{\mathbf{r}}$. Rescaling the variables leads to an appearance of α anisotropy parameter in the final eigenspectrum and also in the wavefunctions, as explicitly given in App. B.

to denote these two quantities different in nature with the same symbol. Hereafter, we use β to refer to the tilt parameter in the context of the the Weyl Hamiltonian, while β is also the appropriate parameter in the context of graphene, which describes the electric field. One may also rephrase the correspondence in terms of an effective electric field. The tilt in the Weyl systems may be interpreted as an effective electric field $E_{\parallel}^{\text{eff}} = \beta v_x B$, where $E_{\parallel}^{\text{eff}}$ plays the same role as $E_{\parallel}$ in graphene.

The eigenfunctions and eigenvalues of the Dirac equation in Eq. 2.38 is easily recovered with exactly the same machinery as was discussed for graphene. The wavefunction of this Dirac equation in the frame R is identical with that of graphene with in-plane electric field. The eigenvalue spectrum is modified by the last term of Eq. 2.38, which is finally

$$\epsilon_n^{\text{W}} = \text{sgn}(n)\sqrt{2|n|}\frac{\hbar\sqrt{v_x v_y}}{\ell}\lambda^{3/2}. \tag{2.39}$$

In principle, the same derivation can be applied to cone $\xi = -1$ to recover its proper eigenfunctions. Note however, that in graphene the electric field does not change sign in the two cones, in α-(BEDT-TTF)$_2$I$_3$ the tilt is opposite in the two valleys. Therefore the eigenfunctions are not identical in the second valley in graphene, and in the Weyl system. To follow closely the above line of derivation, we need to change the sign of the effective electric field, which does not correspond to a physical situation in graphene. For further reference the eigenfunctions for both cones are reproduced in App. B.

2.4.4 Massless Fermions in Related Zero-Gap Organic Compounds

In the previous subsections we have investigated in detail the organic compound α-(BEDT-TTF)$_2$I$_3$ and its particular high-pressure phase in which Dirac fermions occur. This fact is verified by numerous experiments hand in hand with the detailed theoretical investigations. Indeed, α-(BEDT-TTF)$_2$I$_3$ is the best established example among the layered, organic crystals that host Dirac electrons. The quest for Dirac cones in similar organic compounds has naturally set off. Several theoretical investigations appeared, though the experimental data concerning related organic crystals is still very limited.

^{13}C NMR experiments and transport measurements with $\theta-$(BEDT-TTF)$_2$I$_3$ pro-

vided evidence for the existence of Dirac femions in the material, see [98] and [150], though there might be a tiny gap, see [150]. Theoretical investigations are mostly based on tight-binding analysis. In [103] and [104] Mori presented a systematic investigation of two, three and four-molecule compounds, he deduced analytic conditions to the appearance of the zero-gap state and the contact point (in which case the apex of the Dirac cone does not coincide with the Fermi energy) and identified several other potential massless Dirac materials among layered organic conductors. One promising candidate was the four-molecule crystal α-(BEDT-TTF)$_2$KHg(SCN)$_4$, though further investigations revealed that the apex of cones is well below the Fermi energy, only a contact point appears. Other theoretical works proposed α-(BEDT-TTF)$_2$NH$_4$Hg(SCN)$_4$ to have a zero-gap state, here the Dirac cones are predicted to be isotropic, see [29]. Undoubtedly, these proposals require experimental confirmation.

In the following we will refer to the compounds that might host Dirac electrons as *2D Weyl materials*, as their electronic behaviour can be described in a similar manner by the genealized Weyl equation, see [47], [105]. As a particular example, however, we always keep α-(BEDT-TTF)$_2$I$_3$ in mind. Our predictions presented in Chap. 3 and 4 may be equally valid for any of these compounds with tilted, anisotropic Dirac cones, as there we only rely upon these facts.

Chapter 3

Magneto-Optical Properties within a Single-Particle Picture

3.1 Introduction

In the previous chapter we reviewed the basic properties of the 2D materials that are under scrutiny in the present thesis. In this chapter we are focusing on two of them: monolayer graphene in a perpendicular magnetic and crossed electric field, and Weyl materials in a perpendicular magnetic field. We have shown previously that the in-plane electric field in graphene and the tilt in the Weyl materials play a similar role, leading to identical LL eigenfunctions. We have introduced the same notation for the tilt parameter and the parameter describing the in-plane electric field, reflecting their common role. Here we build up a unified description of the magneto-optical properties of these systems, however, when necessary we point out their differences. Note that β is a tunable parameter for graphene, in that case experimental verification of the following results might become possible. For the Weyl materials β is built-in material property, which we take as a constant. With this in mind we develop an experimental procedure by which the determination of this material parameter may become possible.

The appearance of the LLs in graphene in zero electric field have been extensively studied. Besides the usual QH measurements presented in Chap. 2, several magneto-optical measurements are available. In Ref. [135] Sadowski *et al.* performed far infrared transmission experiments on ultrathin epitaxial graphite samples. Using unpolarized

light they identified several Landau level transitions as a function of the magnetic field, and found excellent agreement with the predictions of the single-particle picture discussed in Chap. 2. For right or left circular polarization a selection rule applies, making only $\delta_{|n|,|n'|\pm 1}$ LL transitions available, where $n \to n'$ are the two LLs involved. Later, in Ref. [64] and [57] similar infrared magnetospectroscopy measurements were conducted, however, they found some indications of many-body effects in monolayer graphene.

In Ref. [1] Abergel *et al.* calculated the absorption coefficient , which turns out to have a universal value $\pi\alpha \approx 2.3\ \%$, where α is the fine structure constant. Experimental verification of the above value is given in [110] by Nair *et al.*, who deduced it from the measurement of transmittance. These results are confirmed both theoretically and experimentally by [17], [82] and [89].

Our aim here is to determine the absorption coefficient both for graphene in a magnetic and an in-plane electric field and for Weyl materials in a magnetic field. For this we apply a single-particle picture. As was seen in the literature, the many-body effects renormalize the LL spectrum to such a small extent that we believe the single-particle picture gives a good first approximation. Moreover, we handle the incoming radiation within a classical picture. With these assumptions we give a simple derivation of the absorption coefficient, which, nevertheless, gives us a surprisingly rich physics. The possible experiments are discussed at the end of the chapter.

3.2 Derivation of the Dimensionless Absorption Coefficient

To derive the dimensionless absorption coefficient $i_{abs}(\omega)$ for arbitrary polarization we follow Ref. [176], note that a similar derivation is presented by Booshehri *et al.* in [21] for circular polarization. For simplicity we handle the incoming electromagnetic field classically. We are using the Coulomb gauge in SI units, then the radiation field is

$$\mathbf{A}^{\mathrm{rad}}(\mathbf{r}, t) = \frac{|E_0|}{\omega}(\kappa\hat{\mathbf{e}}_x + \tau\hat{\mathbf{e}}_y)e^{i\omega t} + h.c. \tag{3.1}$$

where $|\kappa|^2 + |\tau|^2 = 1$, ω is fixed, V denotes the volume and we take the $z = 0$ plane. The parameters κ and τ determine the light polarization. For right ($\circlearrowright$) / left ($\circlearrowleft$) circularly polarized light the parameters κ and τ are $\kappa = 1/\sqrt{2}$ and $\tau = \mp i/\sqrt{2}$, for linear polarization $\kappa = 1/\sqrt{1 + (\tan\theta)^2}$ and $\tau = \tan\theta/\sqrt{1 + (\tan\theta)^2}$, where the linearly polarized light has its own parameter θ.[1] For the Weyl materials the rescaled, rotated $\tilde{\kappa}, \tilde{\tau}$ should be applied.[2]

We take the effect of the radiation field $\mathbf{A}^{\mathrm{rad}}$ into account through minimal coupling, that is we replace $\mathbf{A}$ of Eq. 2.13 (graphene) and of Eq. 2.35 (Weyl materials) by $\mathbf{A} + \mathbf{A}^{\mathrm{rad}}$. As the dispersion relation of these systems is linear, one can separate the non-perturbative and the perturbative Hamiltonians without further approximations, as opposed to conventional 2DEG. The perturbative Hamiltonians describing the radiation field become

$$^{\mathrm{E}_\parallel}\delta H = ev_F \frac{|E_0|}{\omega}(\kappa\sigma_x + \tau\sigma_y), \tag{3.2}$$

$$^{\mathrm{W}}\delta H = ev_x \frac{|E_0|}{\omega}(\tilde{\kappa}\sigma_x + \tilde{\tau}\sigma_y + \beta\tilde{\kappa}\sigma_0), \tag{3.3}$$

In this chapter we derive i_{abs} for cone $\xi = 1$. One can check by direct calculation that both cones give the same contribution to the absorption coefficient, therefore we take the valley and the spin degeneracy into account by a factor of 4.

With the view of applying Fermi's Golden Rule, first we compute the matrix element:

$$\delta H_{n,k}^{n',k'} = \int \mathrm{d}\mathbf{r}[\Phi_{n,k}^{\xi=1}(\mathbf{r})]^\dagger \delta H \Phi_{n',k'}^{\xi=1}(\mathbf{r}) = ev\frac{|E_0|}{\omega}\delta(k - k')Q_n^{n'}, \tag{3.4}$$

where v is either v_F for graphene or v_x for the Weyl materials, and we used the spinorial wavefunctions $\Phi_{n,k}^{\xi=1}(\mathbf{r})$ of Eq. 2.17. $Q_{n'}^n$ denotes the dimensionless part of the matrix

[1] In addition to θ, the elliptically polarized light has another paramter ϕ. Then $\kappa = 1/\sqrt{1 + (\tan\theta)^2}$ and $\tau = e^{i\phi}\tan\theta/\sqrt{1 + (\tan\theta)^2}$.

[2] Here the same transformation rule applies as for the momentum $\mathbf{q}$ in Eq. 2.32: $\tilde{\kappa} = \kappa\cos\theta_{\mathrm{tilt}} + \tau\sin\theta_{\mathrm{tilt}}/\alpha^2$ and $\tilde{\tau} = -\kappa\sin\theta_{\mathrm{tilt}} + \tau\cos\theta_{\mathrm{tilt}}/\alpha^2$.

element, which is different for graphene and the Weyl materials

$$
\begin{aligned}
{}^{\mathrm{E}_\parallel}Q_n^{n'} = -\frac{1}{2}\Big[&F^{n,n'}_{|n|,|n'|}\kappa\beta + \mathrm{sgn}(n)\mathrm{sgn}(n')F^{n,n'}_{|n-1|,|n'-1|}\kappa\beta \\
&+\mathrm{sgn}(n')F^{n,n'}_{|n|,|n'-1|}(\kappa + i\tau\lambda) + \mathrm{sgn}(n)F^{n,n'}_{|n-1|,|n'|}(\kappa - i\tau\lambda)\Big]. \qquad (3.5)
\end{aligned}
$$

$$
{}^{\mathrm{W}}Q_n^{n'} = \frac{\lambda}{2}\Big[\mathrm{sgn}(n')F^{n,n'}_{|n|,|n'-1|}(\lambda\tilde{\kappa} - i\tilde{\tau}) + \mathrm{sgn}(n)F^{n,n'}_{|n-1|,|n'|}(\lambda\tilde{\kappa} + i\tilde{\tau})\Big]. \qquad (3.6)
$$

The function $F^{n,n'}_{|n|,|n'|}$ is defined in App. C.

Next we calculate the transition rate per unit area A using Fermi's Golden Rule and taking notice of the occupancy of the initial and final states. Then

$$
R^{\mathrm{emi/abs}}_{n,k\to n',k'} = \frac{1}{A}\frac{2\pi}{\hbar}\left|\delta H^{n,k}_{n',k'}\right|^2 \delta(\epsilon_{n'} - \epsilon_n \pm \hbar\omega) f_0(\epsilon_n)(1 - f_0(\epsilon_{n'})), \qquad (3.7)
$$

where $f_0(\epsilon)$ is the Fermi function.[3] $R^{\mathrm{emi/abs}}_{n,k\to n',k'}$ represents the emission/absorption processes. The total transition rate is obtained by integration over the available k states and summing over the filled (n) and empty (n') Landau levels

$$
R = \sum_{n,n'}\int \mathrm{d}k \int \mathrm{d}k' \left[R^{\mathrm{abs}}_{n,k\to n',k'} - R^{\mathrm{emi}}_{n',k'\to n,k}\right]. \qquad (3.8)
$$

The dimensionless magneto-absorption coefficient is given by

$$
i^{\mathrm{W/G}}_{\mathrm{abs}}(\omega) = \frac{R\hbar\omega}{S}, \qquad (3.9)
$$

where $S = |E_0|^2/2\mu_0 c$ is the magnitude of time averaged Poynting vector. As an approximation we take the $T \to 0$ limit. Furthermore, we introduce a Lorentzian broadening Γ for neglected effects (impurities, phonons, etc). Then one finds

$$
\begin{aligned}
i^{\mathrm{W/E}_\parallel}_{\mathrm{abs}}(\omega) &= \frac{2v^2\hbar\mu_0 c e^2}{\ell^2}\sum_{n,n'}\frac{1}{\epsilon_{n'} - \epsilon_n}\left|{}^{\mathrm{W/E}_\parallel}Q_n^{n'}\right|^2 \delta(\epsilon_{n'} - \epsilon_n - \hbar\omega) \\
&= \frac{2v^2\hbar\mu_0 c e^2}{\ell^2}\sum_{n,n'}\frac{1}{\epsilon_{n'} - \epsilon_n}\left|{}^{\mathrm{W/E}_\parallel}Q_n^{n'}\right|^2 \frac{1}{\pi}\frac{\Gamma}{\Gamma^2 + (\epsilon_{n'} - \epsilon_n - \hbar\omega)^2} \qquad (3.10)
\end{aligned}
$$

both for graphene and 2D Weyl materials, respectively. We estimated $\Gamma = 0.002$eV on

[3]Note that to get a dimensionless absorption coefficient for a 3D material, one shall compute the transition rate per unit volume V.

the basis of Ref. [135] and use this value as a constant broadening.

3.3 Results and Discussion

3.3.1 The Dimensionless Matrix Element

With the view of calculating the dimensionless absorption coefficient we find it illuminating to examine the modulus square of the dimensionless matrix element $\left|{}^{\mathrm{E}_\parallel/\mathrm{W}}Q_n^{n'}\right|^2$. It corresponds to a fixed $n \to n'$ Landau level transition, for which a particularly severe selection rule applies in the $\beta = 0$ ($E_\parallel = 0$) limit: under right/left circular polarization only the matrix elements satisfying $\left|Q_n^{n'}\right|^2 \propto \delta_{|n|,|n'|\pm 1}$ are nonzero. In this chapter we are interested in whether the electric field or the tilt induce additional transitions and analyse their structure, if they appear.

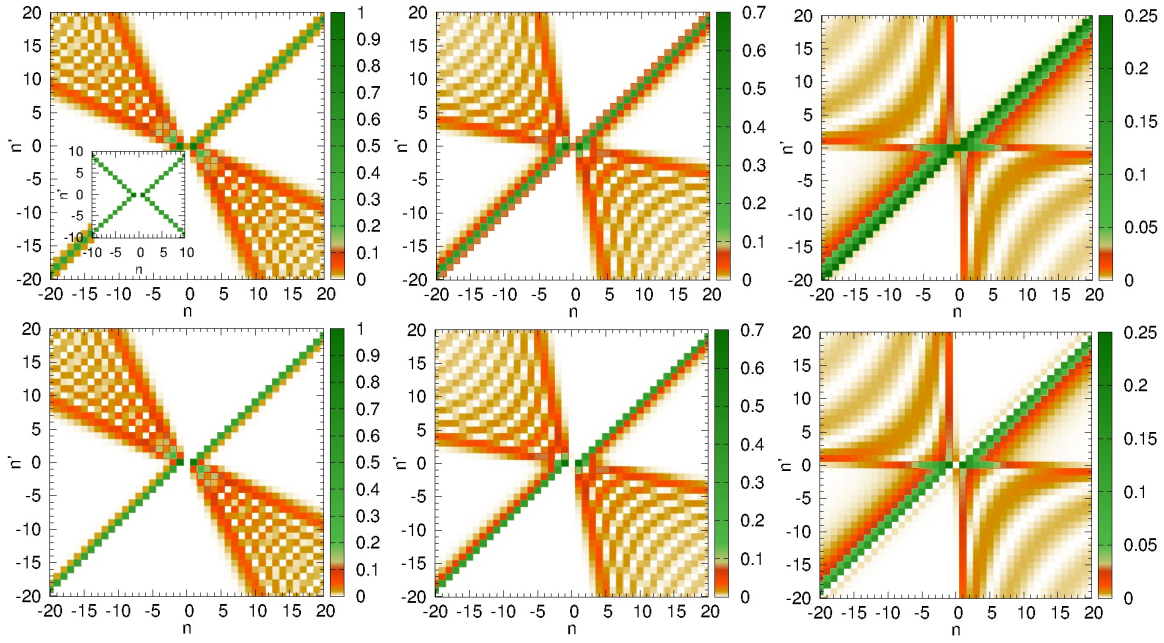

Figure 3.1: Dimensionless matrix elements $\left|{}^{\mathrm{E}_\parallel}Q_n^{n'}\right|^2$ of graphene corresponding to $n \to n'$ transitions are depicted in the first row for $\beta = 0.2, 0.4, 0.7$ respectively. Here right circularly polarized light is considered. The inset shows the $\beta = 0$ case. In the second row the $\left|{}^{\mathrm{W}}Q_n^{n'}\right|^2$ is shown, for the same β parameters, but for such an elliptically polarized light that appears right circularly polarized in the rotated, rescaled system.

Fig. 3.1 shows the modulus square of the matrix elements for both systems under

consideration for various β values under right circular polarization. Here we only consider right circular polarization, as the identity $\left|{}^{\circlearrowleft}Q^{\mathrm{sgn}(n')|n'|}_{\mathrm{sgn}(n)|n|}\right|^2 = \left|{}^{\circlearrowleft}Q^{\mathrm{sgn}(n')|n|}_{\mathrm{sgn}(n)|n'|}\right|^2$ holds between the right and left circular polarization case. For direct comparison with graphene we apply such an elliptically polarized light to the Weyl materials that appears to be right circularly polarized after the rotation and rescale. The results of the two systems are essentially identical, nevertheless, there are some minor differences, e.g. the matrix elements along the antidiagonal ultimately vanish for the Weyl materials for all polarizations, whereas they are proportional to β^2 for graphene under circularly polarized light. We will see that these differences between the two material systems is marginal in the following analysis of the absorption coefficient, therefore we may examine the two systems together.

As it is visible in Fig. 3.1, we obtain novel transitions beyond the usual dipolar ones (see inset in Fig. 3.1). The intraband matrix elements that change the LL index n by more than one unit become nonzero, their weight grows with β. More saliently, the interband transitions show a complex *fan* structure whose opening angle increases with β, and it displays a noticable arc pattern. The fan itself is bounded by large values of the perturbation matrix elements that are not affected by the arc pattern, the latter is visible in the middle of the fan, the arcs become wider with increasing β.

To understand the origin of the remarkable arc pattern, let us consider a bunch of the matrix elements, namely those along the main diagonal, which correspond to transitions $-n \to n$, see Fig. 3.2 and the corresponding explanation. These matrix elements may be computed analytically, leading to a simple form for both material systems under circular polarization (or elliptical polarization that appears as circular in the rotated, rescaled coordinates):

$$Q_n^{-n} \propto (\beta^2 - 1)\beta e^{-2n\beta^2} L^1_{n-1}(4\beta^2 n) \tag{3.11}$$

For the sake of the argument we take n as a continuous variable,[4] bearing in mind that physically relevant values of the function Q_n^{-n} are only those with integer n.

Let us consider the high β limit first. The period δn of the continuous Q_n^{-n} function

[4]The associated Laguerre polynomial is generalizable in terms of confluent hypergeometric functions.

is more than, but close to unity. By Nyquist's sampling theorem in the $\delta n < 2$ range a beating pattern of the physically relevant points arise, with a distance Δn between the consecutive zeros much higher than unity. Indeed, a beating pattern is well-visible in panel 3.2(d). Note that this discussion deals with one particular bunch of the matrix elements only. A similar argument applies for interband transitions along straight lines

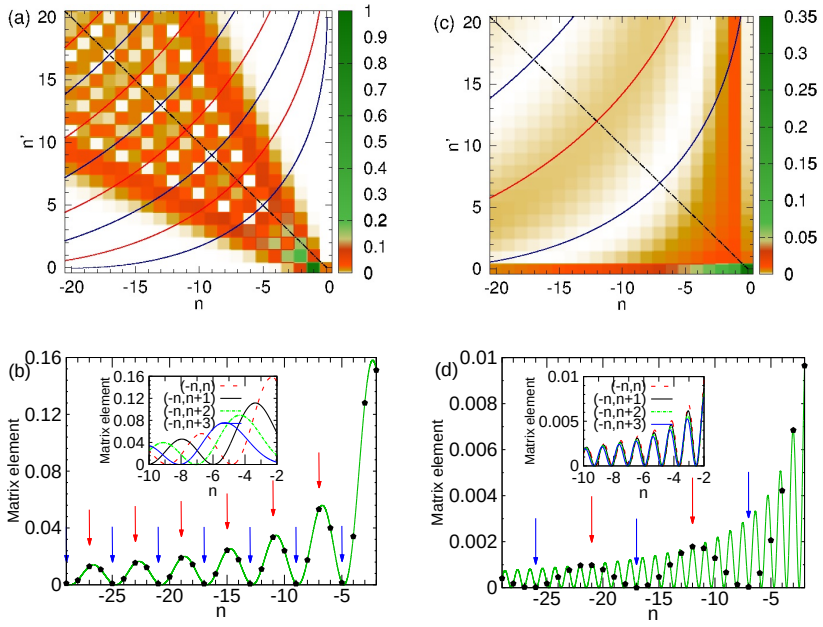

Figure 3.2: Interband matrix elements $\left|{}^{\mathrm{E}_\parallel}Q_n^{n'}\right|^2$ under circularly polarized light for $\beta = 0.2$ (panel (a)) and 0.8 (panel (c)) are reproduced. Black dotted line indicates the diagonal along which Eq. 3.11 is valid. Equienergy contours are represented as blue and red curves, whose energy is identical with the energy of the matrix elements indicated by arrows in panels below. Red curves corresponds to high, blue curves to low energy matrix elements. Panel (b) and (d) show the matrix elements $\left|{}^{\mathrm{E}_\parallel}Q_{-n}^{n}\right|^2$ along the diagonal as a function of n for $\beta = 0.2$ and 0.8, respectively. n is taken as a continuous variable (green line). The black dots indicate the physically relavant values of the matrix element, where n, the index of the two involved Landau levels, is an integer. Inset: Matrix elements along various straight lines of the (n, n') plane.

that go through the origin in the (n, n') plane, although the formulas are considerably more complicated than for the above case. These continuous functions are in phase and have the same period as the one along the main diagonal. Thus, the arc pattern finds its origin as a beating pattern of the underlying Laguerre functions along straight lines of the (n, n') plane of the matrix elements. This also means that one single period exists to describe the arc pattern. More impressively, we also find that the constant

energy contours in the plane of the matrix elements are arcs that follow the striped pattern of the interband matrix elements. This coincidence is remarkable, especially at high β values. Consequently, we anticipate the appearance of this periodic pattern in the absorption coefficient.

The above analysis is true if Nyquist's theorem is applicable, that is $\delta n < 2$, which corresponds to $\beta > 0.35$. At smaller β values, applying the same procedure we find that the equienergy contours roughly follow the arc pattern, especially in the middle of the fan, which forecasts the presence of the periodic oscillations in the absorption coefficient. By examining the matrix elements as continuous functions along various straight lines we find that they have approximately the same period, but are out-of-phase, which makes it impossible to describe the corresponding arc pattern by a single well-defined period, see Fig. 3.2(b). As we shall see later on analysing the absorption coefficients, two characteristic periods will appear.

So far we have considered circular polarization and have found a remarkable arc pattern with a characteristic period depending on the value of β. One may also consider linear polarization, then the matrix elements are described by β, as previously, and by the angle of the polarization θ. Fig. 3.3 shows a strong dependence of the matrix elements on θ for a fixed value of β. Comparing these results with that of the circularly polarized case, a surprisingly new feature is that as θ approaches the direction perpendicular to the electric field or to the tilt direction, the matrix elements inside the fan vanish. As we have already forecasted, and will verify in great detail in the next section, the matrix elements inside the fan are responsible for the appearance of the periodic oscillation in the absorption coefficient, we expect that the disappearance of the matrix elements at a certian angle of the polarization will cancel the observable periodic oscillation as well.

3.3.2 The Absorption Coefficient

In this section we present our final results of the experimentally accessible absorption coefficient calculated in Eq. 3.10 both for graphene in a crossed electric and magnetic fields and for the Weyl materials in a magnetic field. We take the highest filled Landau level $n^F = 0$ throughout the chapter. A straightforward generalization

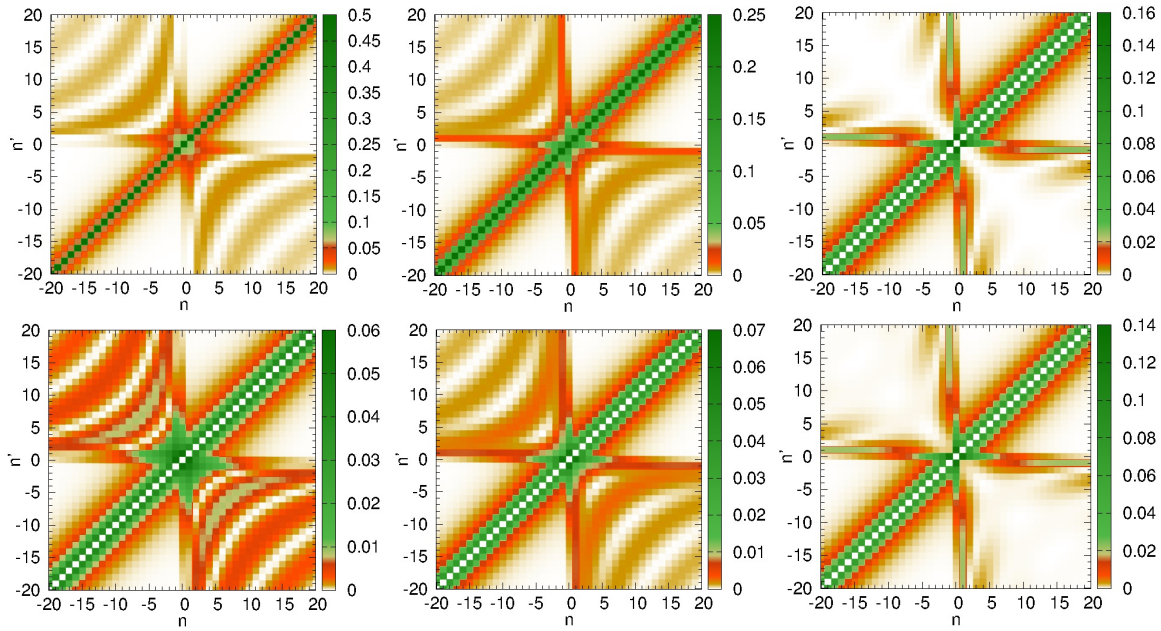

Figure 3.3: Modulus square of the dimensionless matrix elements $\left|{}^{\mathrm{E}_{\parallel}}Q_n^{n'}\right|^2$ at fixed $\beta = 0.7$ under linearly polarized light with $\theta = 0°, 45°, 90°$, respectively (first row). Similar results for the Weyl materials, but here the corresponding angle of the linearly polarized light is $\theta = \theta_{\mathrm{tilt}} + 0°, \theta_{\mathrm{tilt}} + 45°, \theta_{\mathrm{tilt}} + 90°$ (second row).

of our result for arbitrary doping is possible.

Fig. 3.4(a) shows the absorption coefficient for graphene as a function of the frequency for several values of β.

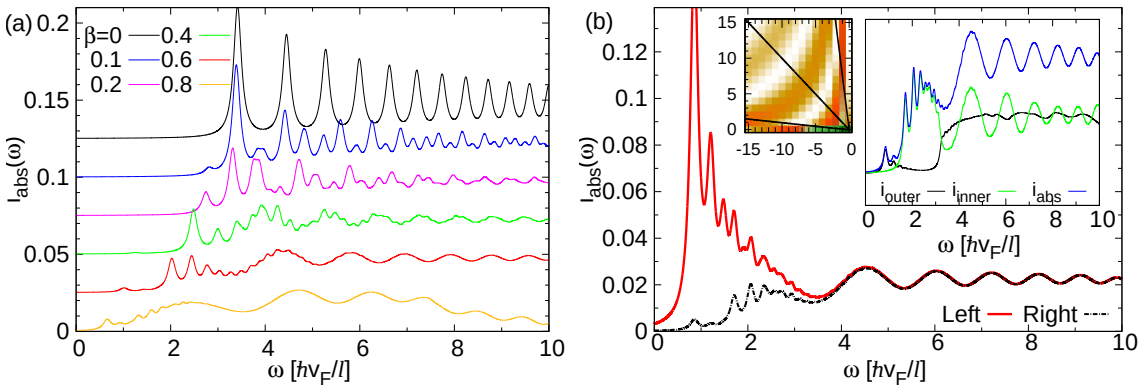

Figure 3.4: $i_{\rm abs}^{\rm E_\parallel}(\omega)$ is depicted for various values of β using right circularly polarized light (panel (a)). The absorption coefficient is shown for fixed $\beta = 0.7$ under left and right circularly polarized light (panel (b)). Inset of panel (b): $i_{\rm abs}^{\rm E_\parallel}(\omega)$ is reproduced (right circular polarization, $\beta = 0.7$) with $i_{\rm outer}$ and $i_{\rm inner}$ as explained in the text.

While for $\beta = 0$ we get back the expected dipolar transitions satisfying the selection rules $\delta_{|n|,|n'|+1}$ for all frequency range, for $\beta \neq 0$ the lines of many newly emerging transitions coalesce resulting in a periodic oscillation of the absorption curve. This feature is especially well-pronounced in the high frequency regime, for intermediate and large values of β. This resulting supermodulation stems from the arc pattern, as the arcs connect transitions that have the same energy, see Fig. 3.2. We point out that the oscillatory behaviour of the high-frequency tail is robust and does not depend on the particular polarization. Fig. 3.4(b), which shows $i_{\rm abs}$ for both right and left circularly polarized light, makes it evident that only few low frequency LL transitions depend on the light polarization, the absorption becomes polarization-independent in the large frequency range, sensitive only to the above-mentioned supermodulation. The inset of Fig. 3.4(b) examines the weight of various matrix elements to the final oscillatory behaviour of the $i_{\rm abs}$. We divided the matrix elements of the $(n,\, n')$ plane into two parts, one part representing the *inner* matrix elements, that give the arc pattern, while the other part contains those elements that delimit the fan, referred to as *outer* elements. As it is nicely shown in the figure the inner elements ($i_{\rm inner}$) are responsible

for the oscillatory behaviour, while i_{outer} only gives a featureless background. In other words, we verified the arc pattern explained in terms of the period of the underlying Laguerre function is the source of the oscillations in the absorption coefficient.

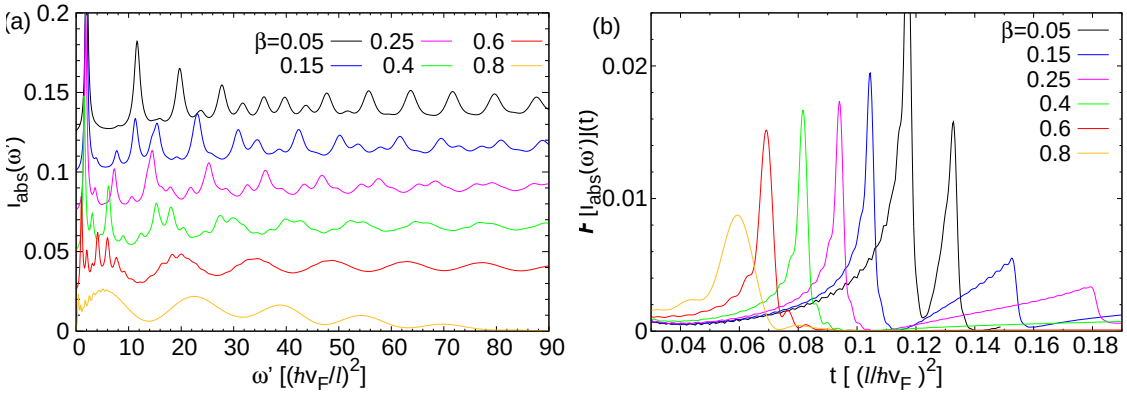

Figure 3.5: Rescaled absorption coefficient $i^{\text{W}}_{\text{abs}}(\omega')$ is shown in panel (a) for linearly polarized light with $\theta = \theta_{\text{tilt}}$. The corresponding Fourier transformed curves $\mathcal{F}[i_{\text{abs}}(\omega')](t)$ are shown in panel (b).

To proceed, we highlight that even though the matrix elements entering the i_{abs} are a periodic function of the LL index n, the Landau level spectra itself scales as $\sqrt{n}$. Therefore we consider the spectra as a function of $\omega' = \omega^2$, and seek the effect of the high-frequency regular pattern in the Fourier transform $\mathcal{F}[i_{\text{abs}}(\omega')](t)$. The rescaled absorption coefficient and the Fourier transform read:

$$i_{\text{abs}}(\hbar\omega = \sqrt{\hbar\omega'}) = \frac{2v^2\hbar\mu_0 ce^2}{\ell^2}\sum_{n,n'}\frac{1}{\epsilon_{n'}-\epsilon_n}\left|Q_n^{n'}\right|^2\frac{1}{\pi}\frac{\Gamma}{\Gamma^2+(\epsilon_{n'}-\epsilon_n-\sqrt{\hbar\omega'})^2}$$
$$\mathcal{F}[i_{\text{abs}}(\omega')](t) = \int_0^\infty \mathrm{d}\omega' e^{-i2\pi t\omega'} i_{\text{abs}}(\hbar\omega = \sqrt{\hbar\omega'}) \tag{3.12}$$

Fig. 3.5 shows a bunch of the absorption curves and the corresponding Fourier transformed curves for the Weyl materials, for several β using linearly polarized light with $\theta = \theta_{\text{tilt}}$. At $\beta > 0.3$ we find one significant Fourier transformed peak, whose location is determined by β. In the small β regime, however, an additional satellite peak appears, as expected from the analysis of the arc pattern in the previous section.

Based on the discussion of the previous section, we expect that by tuning the angle of the linearly polarized light there exists a particular polarization direction for which the visibility of the oscillations of the absorption curves are optimal, and at a

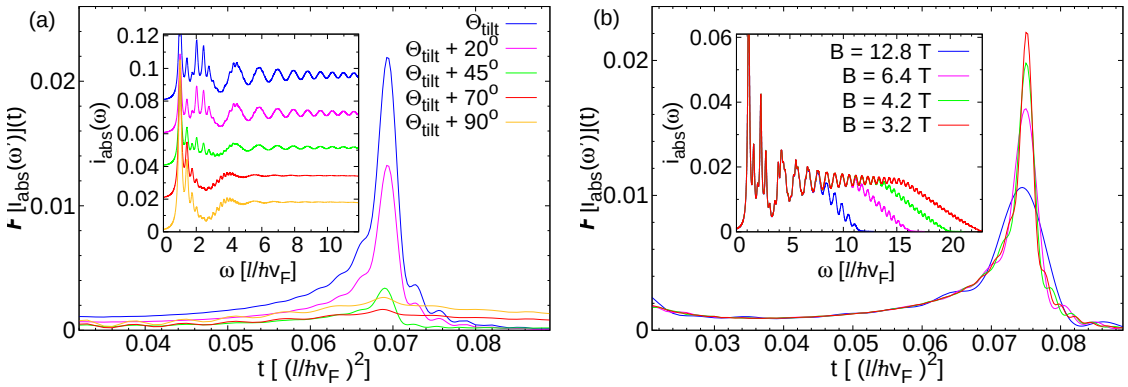

Figure 3.6: Panel (a) shows both the absorption coefficient $i^{\mathrm{W}}_{\mathrm{abs}}(\omega)$ (inset) and the corresponding Fourier transformed curves using $\beta = 0.6$ and linearly polarized light with various angles of the polarization. In a similar arrangement ($\beta = 0.5$ and using linearly polarized light with $\theta = \theta_{\mathrm{tilt}}$), panel (b) depicts how the number of available LLs affects the height of the Fourier transformed peaks. Arbitrary values of $B = 12.8, 6.4, 4.2, 3.2\mathrm{T}$ have been chosen, that correspond to 25, 50, 100 and 150 LLs.

perpendicular direction the oscillations vanish. The same is true for the the Fourier transformed peaks. This is shown in Fig. 3.6(a) for the Weyl materials, in which case the direction of optimal visibility is the tilt direction. For graphene, this is the direction of the electric field.

One can effectively use the above discussed properties to determine experimentally the tilt parameter β and the tilt direction θ_{tilt}, which have been unaccessible so far. The experimental procedure we propose is based on applying linearly polarized light. By tuning the angle of the polarization θ and measuring the optical absorption, its high-frequency, oscillatory behaviour could also be tuned. By identifying the angle, where the oscillations vanish, one can determine θ_{tilt}. Once in the tilt direction (perpendicular to the one before), the location of the Fourier transformed peaks are directly linked to the parameter value β. Fig. 3.7 shows the location of the peak(s) as a function of tilt parameter in the direction of the tilt. Extracting β is straightforward in the moderate-tilt limit, $\beta \leq 0.35$, via the splitting of the two peaks in $\mathcal{F}[i_{\mathrm{abs}}(\omega')](t)$. In the large-tilt region, however, there is only one peak. To extract the exact value of β, one should have an independent value for the Fermi velocity. Note that it is not straigtforward to measure the Fermi velocity, as the density of states $\rho(\epsilon) = \epsilon/2\pi v_x v_y \hbar^2 (1-\beta^2)^{3/2}$

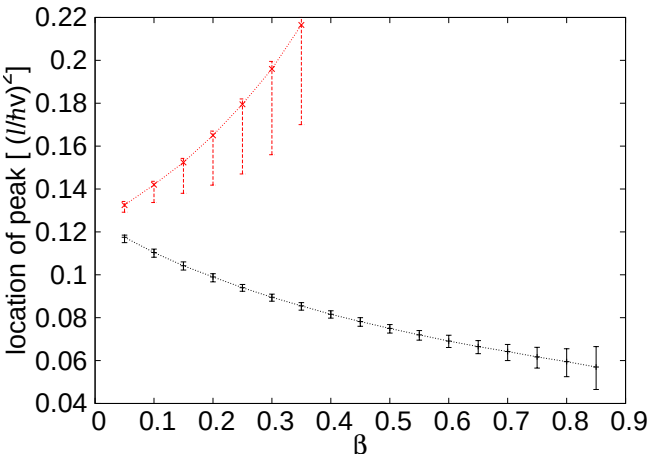

Figure 3.7: The location of the peak(s) in the Fourier-transformed rescaled absorption spectrum $\mathcal{F}[i_{\text{abs}}(\omega')](t)$ for linearly polarized light with $\theta = \theta_{\text{tilt}}$ as a function of the tilt parameter β for a 2D Weyl material. Error bars indicate the FWHM assuming a Lorentzian broadening.

does not depend on the velocity solely, but is also a function of β, which we wish to determine, see Ref. [47]. Thus it is more useful to plot the location of the peak in units of $(\ell/\hbar v^*)^2$, where $v^* = \sqrt{v_x v_y}(1-\beta^2)^{3/4}$, see Fig. 3.8. The velocity v^* is measurable directly in thermodynamics or low-frequency magneto-optics.

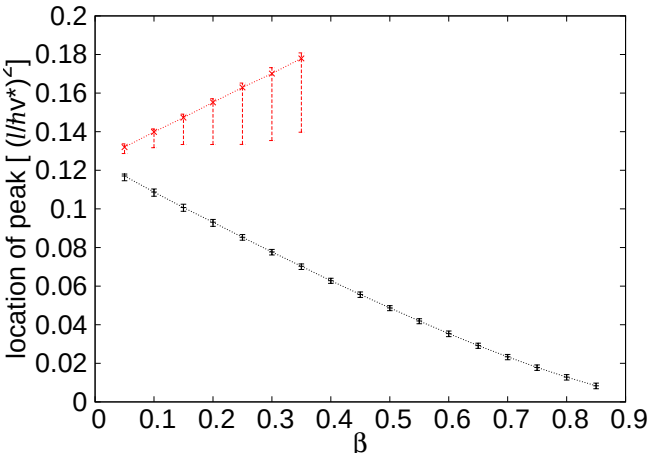

Figure 3.8: The same as in Fig. 3.7, but the location of the peak(s) are given in units $(\ell/\hbar v^*)^2$.

Finally, we consider the issue of the number of available LLs. For graphene the available number of LLs is high enough to see the above oscillations in the absorption, the question of cutoff does not arise. However, the number of Landau levels within

the range of validity of the Weyl Hamiltonian is limited, we examine the robustness of our results against the change of the Landau level cutoff. We estimated that the number of available Landau levels as $320/B$.[5] The inset of Fig. 3.6(b) shows the effect of an arbitrary change of the magnetic field with this particular cutoff. By lowering the available number of LLs, the oscillatory behaviour remains visible in the $i^{\mathrm{W}}_{\mathrm{abs}}(\omega)$ curves. The relevant peaks of $\mathcal{F}[i_{\mathrm{abs}}(\omega')]$ also survive, though with reduced height. We can see that the oscillatory behaviour of $i^{\mathrm{W}}_{\mathrm{abs}}$ is present for as few as 25 LLs ($B = 12.8\mathrm{T}$). We conclude that our previous predictions are valid up to $B \approx 6.5\mathrm{T}$, which is a safe choice of the magnetic field.

3.4 Concluding Remarks and Future Perspectives

In conclusion, the pseudo-relativistic nature of electrons in graphene in crossed electric and magnetic fields, and in 2D Weyl materials such as α-(BEDT-TTF)$_2$I$_3$ manifests itself in unique magneto-optical properties. A large number of transitions beyond the usual dipolar ones become possible. Their coalescence at high frequencies is the fingerprint of the broken rotation invariance in both cases either due to the particular tilt or that of the electric field, which results in an oscillatory behaviour of the absorption coefficient measured as a function of the frequency. We have pointed out that the oscillations show a strong β dependence, this feature may be expoited to determine the actual β parameter only by measuring the magneto-optical response under linearly polarized incident radiation.

In graphene, this effect might be observed easier than the earlier predicted Landau level collapse in Ref. [87], because the magneto-optical effect is present in the low-β range where the change of the Landau level energies is still small. Note that here the the electric field is an experimentally tunable parameter, therefore experiments are expected to verify our theory. However, a complication may arise due to screening of the external electric field. Here, as the LL energies are k dependent, see Eq. 2.16, the Landau levels may intersect the Fermi energy even in the middle of the sample, leading to an additional screening effect similar to that of the edge states at the boundaries of

[5]The detailed discussion of the derivation is presented in Sec. 4.2.2

the sample, see Ref. [28] and [83]. The detailed analysis of the screening effect due to the k dependent LLs is delegated to future work.

We note that an upper limit to the achievable β-values in graphene is set by the condition that the potential energy change over a magnetic length should be less then the energy difference between adjecent LLs to avoid tunneling current along the parallel electric field. For the $n = 0, 1$ Landau levels, this means $eE_{\parallel}\ell < \epsilon_1^{\mathrm{E}_{\parallel}} - \epsilon_0^{\mathrm{E}_{\parallel}} = \frac{\hbar v_F \sqrt{2}}{\ell}(1 - \beta^2)^{3/4}$, which sets $\beta < 0.75$.

In α-(BEDT-TTF)$_2$I$_3$ and potentially other quasi-2D organic materials with massless Dirac cones, see Sec. 2.4.4, on the other hand, a quantitative analysis of this fingerprint, in combination with other information on Fermi velocities if the tilt turns out to be large, helps us determine the tilt parameter of the massless Dirac cones. In this context, however, the size of the window of the pressure cell may set an upper limit to the wave lenght of the incident light. We propose therefore to extend our present calculations and determine the response measured in Raman spectroscopy.

Finally, we notice that the same magneto-optical features should appear in strained graphene, where uniaxial strain yields tilted Dirac cones (see Ref.[47]) that are predicted to show a clear signature also in Raman spectroscopy, see[6].

Chapter 4

Magnetoplasmons - Density Oscillations in Magnetic Field

4.1 Introduction

In the previous chapter we examined the magneto-optical properties of α-(BEDT-TTF)$_2$I$_3$ in a magnetic field and graphene in a crossed electric and magnetic fields assuming non-interacting electrons. In this chapter we aim to examine the collective excitations of α-(BEDT-TTF)$_2$I$_3$. For this we shall consider electron-electron interactions within the *random phase approximation*. Our objective is to calculate the density-density response function, hand in hand with the dynamical dielectric function, which lead us to the spectrum of collective excitations.

4.1.1 General Formalism of the Density Response Function

Consider a perturbative externel field given by its Fourier transformed amplitude $V_{\text{ext}}(\mathbf{k}, \omega)$ acting on the system of interacting electron gas and suppose that we are in a *linear response* regime.[1] As the external potential couples to the density of the electron system one of the quantites of crucial importance is the retarded density-

[1]Detailed discussion about the linear response theory and the various approximations of the interacting electron gas is available in many excellent textbooks. In the subsequent chapters I mainly rely on Ref. [46] by G. F. Giuliani and G. Vignale, Ref. [142] by J. Sólyom or Ref. [43] by A. L. Fetter and J. D. Walecka, though this list is far from being complete. In connection with the collective excitations of electron systems, see also the Ref. [18], [19] and [20].

density response function denoted as $\chi(\mathbf{k},\omega)$ and defined as

$$n_{\text{ind}}(\mathbf{k},\omega) = \chi(\mathbf{k},\omega)V_{\text{ext}}(\mathbf{k},\omega). \tag{4.1}$$

The calculation of the density-density response function $\chi(\mathbf{k},\omega)$ means the description of an interacting electron system, for which certain approximation methods are needed. The most frequently used approximation scheme is the random phase approximation (RPA), where χ is approximated as follows:

$$\chi^{\text{RPA}}(\mathbf{k},\omega) = \frac{\chi^{(0)}(\mathbf{k},\omega)}{\epsilon_r^{\text{RPA}}(\mathbf{k},\omega)} \equiv \frac{\chi^{(0)}(\mathbf{k},\omega)}{1 - v(\mathbf{k})\chi^{(0)}(\mathbf{k},\omega)}, \tag{4.2}$$

where we introduced the dynamical dielectric function $\epsilon_r^{\text{RPA}}(\mathbf{k},\omega)$ and $v(\mathbf{k}) = e^2/2\epsilon_r\epsilon_0 k$ is the bare Coulomb interaction in 2D and $k = |\mathbf{k}|$. $\chi^{(0)}(\mathbf{k},\omega)$ is the density-density response function of the non-interacting electron gas, usually called the Lindhard-function.[2] In diagrammatic perturbation theory the bare bubble diagram describes the interactionless propagation of an electron-hole pair, that is an electron and a hole disappears at a certain place but another electron-hole pair is created simultaneously in another place. To determine $\chi^{(0)}$ the usual procedure is to calculate the non-interacting, time-ordered response function, which is:

$$\chi^{\text{T}}(\mathbf{k},\omega) = -\frac{i}{\hbar}\text{Tr}\int\frac{\mathrm{d}E}{2\pi}\int\frac{\mathrm{d}\mathbf{p}}{(2\pi)^2}\mathcal{G}^{(0)}\left(\mathbf{p},E\right)\mathcal{G}^{(0)}\left(\mathbf{p}+\mathbf{k},E+\omega\right). \tag{4.3}$$

here $\mathcal{G}^{(0)}(\mathbf{k},\omega)$ denotes the time-ordered, non-interacting Green's function. The retarded response function and the time-ordered response function relate to each other in the following way:

$$\begin{aligned}\text{Re}\chi^{(0)}(\mathbf{k},\omega) &= \text{Re}\chi^{\text{T}}(\mathbf{k},\omega)\\ \text{Im}\chi^{(0)}(\mathbf{k},\omega) &= \text{sgn}(\omega)\text{Im}\chi^{\text{T}}(\mathbf{k},\omega).\end{aligned} \tag{4.4}$$

A practically relevant property of the electron system which is simply deducable from the bare density-density response function is the particle-hole excitation contin-

[2] This quantity may also be referred to as the bare or non-interacting polarization function or even free polarization bubble.

uum or excitation spectrum (PHES). The PHES is a well defined segment of the $\omega - \mathbf{k}$ space where $\mathrm{Im}\chi^{(0)}(\mathbf{k},\omega) \neq 0$ and where it is possible to excite elementary electron-hole pairs.[3] Naturally, the PHES may also be characterized by $\mathrm{Im}\epsilon_r(\mathbf{k},\omega) \neq 0$. The PHES is delimited by boundaries to be determined for each particular system.

Furthermore, the poles of the density-density response function determine the frequencies of the collective modes in an interacting many-body system. Besides the particle-hole excitations present in the PHES, where $\mathrm{Im}\chi^{(0)} \neq 0$, collective density oscillations appear where both the imaginary and real part of the dielectric function vanishes. These density fluctuations, called plasmons, appear at the long wavelength limit, at higher energies than the boundaries of the PHES. The spectral weight of the electron-hole excitations is greatly reduced, part of the spectral weight is transferred to the plasmon mode. Further properties of an interacting electron gas, such as static sreening, may also be deduced from the density-density response functions.

In the following chapter we apply the RPA to approximate the total polarizability of aI3 assuming perpendicular magnetic field. First we review existing calculations of $\chi^{\mathrm{RPA}}(\mathbf{k},\omega)$ and $\epsilon_r^{\mathrm{RPA}}(\mathbf{k},\omega)$ for conventional 2DEG and for graphene. In the main part of the chapter we present a similar calculation for a more complex setup of aI3, thus we extend existing zero-field calculation of this material. In addition, we compare our results with graphene and analyse the effect of tilt and anisotropy of the Dirac cones on the collective modes of the layered organic compound.

4.1.2 Magnetoplasmons in Two-Dimensional Systems

First, we review the calculation of the dynamical dielectric function and the density-density response function in a conventional 2DEG with a parabolic dispersion relation and m_Q effective mass. First, we summarize the zero-magnetic field results, then we review the non-zero field case.

The PHES is delimited by parabolic boundary lines

$$\omega_{\pm}^{Q}(\mathbf{k}) = \frac{\hbar^2}{2m_Q}k^2 \pm \frac{\hbar^2 k_Q^F}{m_Q}k, \tag{4.5}$$

[3]Note that for isotropic materials this reduces to a $\omega - k$ plane, where $k = |\mathbf{k}|$.

where $k = |\mathbf{k}|$ and the superscript Q stands for *quadratic*, see Fig. 4.1(a).

In zero magnetic field the bare polarization function for 2DEG was first determined by Stern in Ref. [145]. The PHES consists of intraband excitations, the only possible excitation in the case of a parabolic band. Note that within the RPA the boundaries of the PHES are identical with that of the noninteracting boundaries $\omega^Q_\pm(\mathbf{k})$.

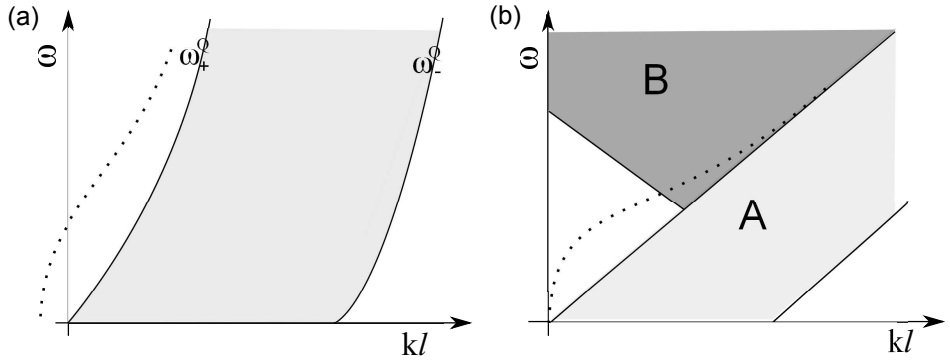

Figure 4.1: Panel (a): The shaded region corresponds to the PHES of the parabolic band of a conventional 2DEG. The demarcating lines of Eq. 4.5 are marked with solid lines. The plasmon mode is marked with a dotted line. Panel (b): The PHES of graphene. Intraband and interband excitations are marked separately. The plasmon mode is also shown. The forbidden region is also marked.

As argued in [46], the imaginary part of the bare polarization function in zero magnetic field presents some structure, e.g. a higher spectral weight in the small energy region near the ω^Q_+. The $k \to 0$ limit of the plasmon mode, determined from the expansion of χ^{RPA} in [145], disperses as $\sqrt{k}$. The plasmon mode touches the PHES at some critical value of k_c, disperses parallel to the boundary line, and is slowly Landau-damped due to the particle-hole pairs.[4]

For non-zero magnetic fields the eigenvalues and eigenfunctions of the 2DEG are given in Eq. 2.2 and 2.3. The non-interacting polarization was determined in Refs. [66] and [80] and given as follows

$$\chi^{(0)}_Q(\mathbf{k},\omega) = \frac{1}{2\pi\ell^2} \sum_{n' \le n^F_Q} \sum_{n > n^F_Q} \left(\frac{|F_{n,n'}(\mathbf{k})|^2}{\omega - \epsilon^Q_n + \epsilon^Q_{n'} + i\delta} + \frac{|F_{n',n}(\mathbf{k})|^2}{-\omega - \epsilon^Q_n + \epsilon^Q_{n'} - i\delta} \right) \tag{4.6}$$

In App. D we first calculate the bare Green's functions, see D.1, then by Eq. 4.3

[4]This is in contrary to the 3D case, where the plasmon mode is heavily damped when entering the PHES at k_c, see Ref. [46].

we determine the bare polarization function, see App. D.2. The corresponding form factor $F_{n',n}(\mathbf{k})$ is defined in App. E.1. Fig. 4.2 shows the non-interacting and the RPA polarization functions. Note that the color bar represents magnitude of Imχ.

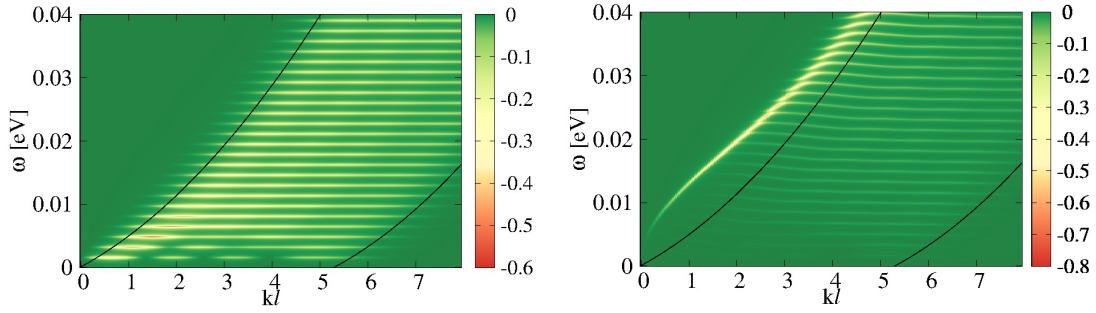

(a) $\mathrm{Im}\chi_{\mathrm{Q}}^{(0)}$ (b) $\mathrm{Im}\chi_{\mathrm{Q}}^{\mathrm{RPA}}$

Figure 4.2: Polarization function for 2DEG. We use the following parameters: $\epsilon_r = 10$, $m_{\mathrm{Q}} = 0.3m_0$, $B = 4$ T, $\delta = 0.1\hbar\omega_c$, $n_Q^F = 3$, the latter is the highest filled Landau level. The black curves denote the boundaries of the PHES calculated using Eq. 4.5.

Due to the Landau level quantization the PHES is chopped into horizontal lines that are equally spaced, separated by $\hbar\omega_c$, as it is well visible in Fig. 4.2(a). Here we choose a disorder broadening $\delta = 0.1\hbar\omega_c$, which determines the width of each horizontal lines. Though the spectral weight is quite homogeneously distributed, there is a considerable *island* structure present in the particle-hole excitations in the lowest energy range: here the horizontal lines are splitted into several parts, the number of parts are determined by the filling factor. The detailed discussion of the origin of this particular feature is given in Ref. [132].

The electron-electron interaction causes the appearance of a collective mode above the PHES, see Fig. 4.2(b). This mode, which is the plasmon mode modified by the magnetic field, is referred to as the upper-hybrid mode (UHM).[5] An approximation for the dispersion relation of the UHM is given in Ref. [27] and [145]. We note that besides the UHM with certainly the highest spectral weight, the horizontal lines may be interpreted as magnetoexcitons, bound particle-hole pairs with well-defined center of mass momentum k. The notion of magnetoexcitons was first introduced in Ref.

[5]Note that the same mode may also be referred to as magnetoplasmon, however we stick to the convention of using the term upper-hybrid mode instead.

[66]. This chapter is, however, devoted to the examination of the UHM as the latter collective mode is the best captured within the RPA.

Let us now consider monolayer graphene. A detailed review of the PHES and the collective modes of graphene is given in [48].

For zero magnetic field, the polarizability of graphene was first investigated by Shung in Ref. [140]. His primary interest was to examine the dielectric function and plasmon structure of graphene intercalation compounds, which consists of a series of (one or more) graphene and intercalated layers. As an intermediate step he considered a single graphene layer, and calculated the dielectric function $\epsilon_r(\mathbf{k}, \omega)$, and determined its PHES as well as the plasmon modes. Besides Ando examined graphene and its static screening and impurity scattering in Ref. [5], he emphasized the absence of backscattering, and examined its consequences. Wunsch *et al.* and Hwang *et al.* determined the dielectric function within the RPA, the plasmon mode and its decay rate, see Ref. [60] and [165].

To proceed, let us consider the particle-hole excitation spectrum in more detail, see Fig. 4.1(b). It consists of two different types of excitations, one is the intraband excitations (A), also available in 2DEG, the other is the interband excitations (B). Note that the first is only present in doped graphene.

The bare polarizability is not homogeneously distributed within the PHES, contrary to the 2DEG. Here, the chirality factor plays a crucial role, making most of the spectral weight center around the line $\omega = v_F k$. Within the RPA, the plasmon mode appears with the same $\sqrt{k}$ type dispersion relation as for 2DEG. The plasmon enters the interband excitation region and is damped there. Our considerations so far are valid for doped graphene. For the discussion about the complications that arise due to the vanishing density of states at the Dirac point in undoped graphene, see [44].

Consider now doped graphene in non-zero magnetic field. In Fig. 4.3 we reproduce the non-interacting density-density response function $\chi_{\mathrm{G}}^{(0)}$ and also the density-density response within RPA $\chi_{\mathrm{G}}^{\mathrm{RPA}}$. As shown in panel (a), the PHES is also chopped into horizontal lines, but due to the Landau level quantization of Eq. 2.10, these lines are not equidistantly spaced, rather their density increases even at moderate excitation energies, so they overlap even at small disorder broadening. Furthermore, each hori-

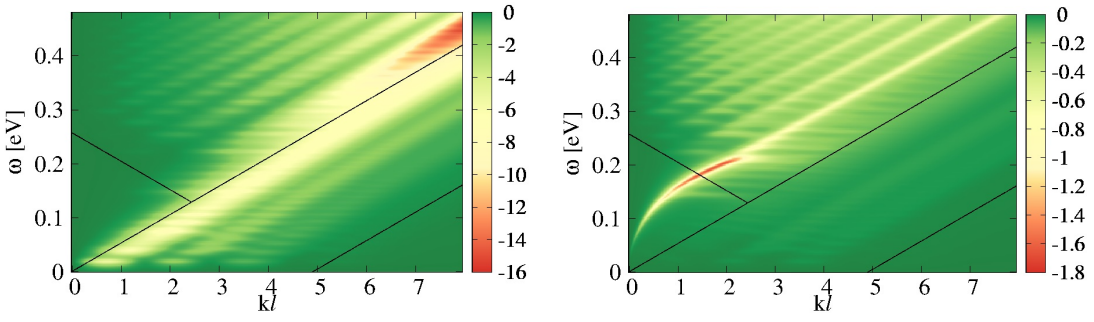

(a) $\mathrm{Im}\chi_{\mathrm{G}}^{(0)}$ (b) $\mathrm{Im}\chi_{\mathrm{G}}^{\mathrm{RPA}}$

Figure 4.3: The density-density response function for graphene. The figures are reproduced from Ref. [132] with the parameters $\epsilon_r = 1$, $n_G^F = 3$ and B = 4 T.

zontal line is split into several parts, referred to as islands. The appearance of these islands is similar in nature to the case of 2DEG, however, due to the non-equidistant Landau level spacing they do not merge, but remain separated for all horizontal lines. These two effects together with the chirality factor lead to the appearance of linear magnetoplasmons visible in χ^{RPA}. Though these modes are essentially a coalescence of magnetoexcitons, their high spectral weight justifies their identification as a distinct mode. In χ^{RPA} the UHM is also visible, starts in the forbidden region, and ends in the interband region.

4.2 Magnetoplasmons in α-(BEDT-TTF)$_2$I$_3$: the Continuum Model

The calculation of polarization function in aI3, considering its linear valleys only, is a non-trivial extension of the isotropic graphene-case, as here due to the anisotropy and tilt one shall consider the $\omega - \mathbf{k}$ space instead of the usual $\omega - k$ plane. Considering one of the anisotropic Dirac cones in zero magnetic field, which is undoubtedly an unphysical situation, one expects the occurrence of the plasmon mode just like in graphene, however with an angle dependent dispersion. Indeed, this expectation is verified by Nishine *et al.* in Ref. [112]. However, the presence of two oppositely tilted Dirac cones, which is the physically relevant situation, necessitates the investigation of their interplay. This leads us to the question of the number of plasmon modes and

their mutual damping characteristics. This issue was discussed in Ref. [113]. Indeed, Nishine *et al.* identified a new plasmon mode and interpreted its appearance in terms of the *plasmon filtering effect*.

In this chapter our aim is twofold. First we extend the existing zero-field calculation, comprising both Dirac cones, to the non-zero magnetic field case. We give a comprehensive explanation for the appearance of the new plasmon mode in terms of *intervalley-damping*. Second we include the massive valley and determine how its presence affect the polarization of the linear valleys. This inclusion leads us the so called *three-valley model*. By doping and/or the magnetic field it is possible to switch on and off the massive valley, therefore it might be possible to experimentally verify its presence.

4.2.1 The Particle-Hole Excitation Spectrum at $B = 0$ T Field

Nishine *et al.* discussed the dynamical dielectric function and the density-density response function of aI3 in [112] and [113]. They detemined the $\chi^{(0)}(\mathbf{k},\omega)$ and $\chi^{\mathrm{RPA}}(\mathbf{k},\omega)$ in a semi-analitic calculation. Dealing only with one of the cones they determined the angle dependence of the boundaries of the PHES, and extensively discussed the effect of tilt and anisotropy on the various quantities, including the optical conductivity and screening. They found an angle dependent $\hbar\omega \sim \sqrt{k}$ behaviour for the plasmon mode. Considering the two cones together they calculated the collective modes within RPA. They observed a new mode besides the regular one at an intermediate and large k range, whose presence and spectral weight depend strongly on the angle. They interpreted this as the cooperation between the two cones and called it a plasmon filtering effect: certain angles filter the new mode more effectively than others. As we shall see later in Sec. 4.3, the non-zero magnetic field results show essentially the same phenomena. Our basic premise, however, is that each valley has its own proper plasmon mode, and we give a comprehensive interpretation in terms of the damping effect between valleys named as *intervalley-damping*.

Regarding the possibility of particle-hole excitations, the (ω, k) plane can be divided into several regions. The regions of possible intraband (A) and interband (B) particle-hole excitations are separated by the boundary line ω_{res}. Due to the opposite tilt, the

various regions and their boundaries differ for the two cones in any general directions. Both regions are divided into subregions, as explained below.

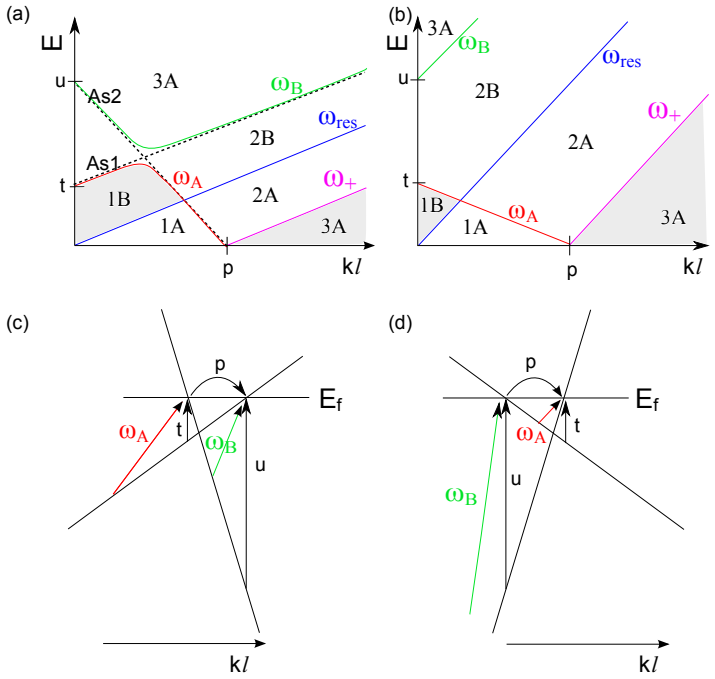

Figure 4.4: The regions and subregions of the (ω, k) plane from the point of view of (a) cone R, and (b) cone L in a particular direction $\theta = \theta_{\text{tilt}}$. (c,d) Cuts of cones R and L in the same direction. In the direction $\theta = \theta_{\text{tilt}} + \pi$, the cones L and R are interchanged, such that the panels (a,c) would correspond to cone L and (b,d) to cone R. The distinguished energies t, u, momentum p, and asymptotes $As1, As2$ are indicated. The gray shading indicates the forbidden regions 1B and 3A, where there are no particle-hole excitations in the absence of electron-electron interactions.

Figures 4.4(a) and (b) depict the (ω, k) plane in the direction $\theta = \theta_{\text{tilt}}$, where $\theta = \arctan(k_y/k_x)$ is the angle of the momentum. In this direction the steepness of cone R is minimal, while that of cone L is maximal. First consider cone R in this direction [Figs 4.4(a) and (c)]. Zero-energy excitations must have a momentum transfer less than the major axis p of the ellipsoidal Fermi surface. Excitations with higher momenta require a minimal energy, which defines the upper boundary ω_+ of the forbidden subregion 3A, where $\text{Im}\chi_R^{(0)} = 0$.

Excitations with zero momentum transfer must be interband. For $k = 0$, there are two special energies. The smallest one is denoted t in Fig. 4.4. Below this energy no $k = 0$ excitation is possible. If we increase the total momentum of the particle-hole

pair in the positive manner, we must move the hole in the $-k$ direction [see arrow at ω_A in Fig 4.4(c)]. Then the excitation energy increases, which explains the rise of the boundary line ω_A for small momenta. By thus decreasing the hole's wave vector, one follows the asymptote $As1$ in Fig 4.4(a), which ultimately merges into the boundary line ω_B.

Starting from u, one can decrease the excitation energy with positive total momentum; this branch corresponds to ω_B and follows asymptote $As2$ at small momenta, which merges into ω_A in the intraband region. At larger values of the momentum, ω_B asymptotically follows $As1$. The reason why the boundaries ω_A and ω_B deviate from the asymptotes $As1, As2$ and do not intersect each other is due to the 2D nature of the excitations, i.e., one needs to consider transitions outside of the one-dimensional cut examined so far. Between ω_A and ω_{res} no particle-hole excitations exist, thus region 1B is forbidden, just like 3A for intraband excitations.

If one considers excitations of cone L in the same momentum direction, the shapes of boundaries ω_B and ω_A differ considerably [Fig 4.4(b)]. The smallest energy of a $k = 0$ excitation is still t. However, in contrast to cone R, it is possible to decrease the energy from t by moving the hole in the $-k$ direction [Fig 4.4(d)], and the corresponding branch defines boundary ω_A. Starting from u one can only increase the excitation energy with a negative total momentum, and one thus obtains the branch corresponding to ω_B. Naturally, the two cones are related by time-reversal symmetry, which also changes the sign of $\mathbf{k}$. The role of the R and L cones are therefore interchanged in the $\theta_{\text{tilt}} + \pi$ direction, and the regions of cone R (L) are then those in Fig. 4.4(b,d) [Fig. 4.4(a,c)].

4.2.2 Approximations and Methods

The Three-Valley Model

Consider the first Brillouin zone of aI3 in Fig. 2.5(b). In our *three-valley model* we incorporate the two linear valleys at R and L as well as the massive valley at X. We divide the Brillouin zone into regions where the linear dispersion relation (in a circle around R and L), the quadratic approximation (in a circle around X), or none of these is valid. As we are interested in low-energy, low momentum excitations in this chapter,

we can safely neglect those part of the Brillouin zone that are outside of either the linear or the quadratic approximations, see also the discussion below.

Assume that the linear approximation is valid around R and L separately in a circular region, whose radius is chosen as about 1/8 of the side of the first Brillouin zone [$\approx 2\pi/(1\text{ nm})$]. This picture is consistent with the band structure obtained in Refs. [3], [70] and [74]. As it was mentioned in Chap. 2, there are several available parameter sets to describe the tilted cones. To be specific, we will use Kobayashi *et al.*'s estimate of the velocity parameters, see [75]:

$$v_0^x = -9.4\ 10^4\ \tfrac{\mathrm{m}}{\mathrm{s}},\quad v_0^y = -8.32\ 10^4\ \tfrac{\mathrm{m}}{\mathrm{s}},\quad v_x = 3.45\ 10^5\ \tfrac{\mathrm{m}}{\mathrm{s}},\quad v_y = 2.45\ 10^5\ \tfrac{\mathrm{m}}{\mathrm{s}}, \tag{4.7}$$

which yield $\beta = 0.437$, $\alpha = 1.18$, $\lambda = 0.89$, and $\theta_{\mathrm{tilt}} = 51.14°$. We emphasize that we are focusing on qualitative features that hardly depend on this particular choice. Using these velocities the energy cutoff E_L^c and the number of available LLs n_L^c are

$$E_L^c \approx 0.16\text{ eV}, \qquad n_L^c \approx 320/B\ [\mathrm{T}]. \tag{4.8}$$

We estimate furthermore the Fermi wave vector. Based on Monteverde *et al.*'s electron density data in Ref. [101], k_L^F in the linear valleys is tiny, $k_L^F = \sqrt{4\pi\rho_L/g_L} \approx 2\times 10^6$ m^{-1}, using $g_L = 4$ for valley and spin degeneracy.

The quadratic approximation is valid in a circle around point X, with a radius that is estimated as 17.5 % of the side of the first Brillouin zone. The massive valley is taken as isotropic with an effective mass

$$m_Q \approx 0.3 m_0, \tag{4.9}$$

see [101]. The valley is hole-like, a paraboloid of revolution open from below. The Hamiltonian of the massive band is $\hat{H}_{\mathrm{Q}} = E_{\mathrm{offset}} - \frac{(-i\hbar\nabla + e\mathbf{A})^2}{2m_Q}$ and the Landau level spectrum is given by $\epsilon_n^{\mathrm{Q}} = E_{\mathrm{offset}} - \hbar\omega_c\left(n+\frac{1}{2}\right)$, where ω_c defined before. Notice that these nonnegative integers actually number hole LLs. Combining the carrier densities measured by Monteverde *et al.* in [101] with Eq. 4.7 and 4.9, the top of the massive

band is about

$$E_{\text{offset}} \approx 0.46 \text{ meV} \tag{4.10}$$

above the Dirac point of the massless valleys. Similar calculations yield the cutoff energy E_Q^c and the number of LLs is n_Q^c as

$$E_Q^c \approx 0.15 \text{ eV}, \tag{4.11}$$

$$n_Q^c \approx 390/B \text{ [T]}. \tag{4.12}$$

The Fermi mometum k_Q^F of the massive band is $k_Q^F = \sqrt{4\pi\rho_Q/g_Q} \approx 2 \times 10^7 \text{ m}^{-1}$, using $g_Q = 2$ for spin degeneracy.

Polarizability of the Total System

We identify the collective modes in RPA using Eq. 4.2. $\chi^{(0)}$ is calculated from Eqs. 4.3 and 4.4. In Eq. 4.3, $\chi^{\text{T}}(\mathbf{k}, \omega)$ picks up a contribution only if $(\mathbf{p}, E)$ and $(\mathbf{p}+\mathbf{k}, E+\omega)$ specify one filled and one empty state. As we will restrict our attention to $\omega < \min(E_Q^c, E_L^c) \approx 0.15$ eV, we can ignore the cases when both of these points are outside the vicinities of the L, R and X points, respectively, assuming that the Fermi energy is near the contact points. We can also ignore the cases where the states $(\mathbf{p}, E)$ and $(\mathbf{p}+\mathbf{k}, E+\omega)$ are in distinct valleys, as long as we focus on small momenta $k < K \equiv \min(k_Q^c, k_L^c)$. This approximation is justified because the Coulomb interaction intervenes in the dielectric function $\epsilon^{\text{RPA}}(\mathbf{k}, \omega)$, and suppresses intervalley contributions in comparison to intravalley contributions at fixed ω by a factor $v(K)/v(k_F) = k_F/K \ll 1$ near the characteristic Fermi momentum k_F. Furthermore, for small doping $\mu \ll \min(E_Q^c, E_L^c)$, we can also ignore the transitions that involve a state in the range of validity of the linear/quadratic approximations and a state outside of this domain. Thus we can safely approximate the bare polarizability for our limited purposes as the sum of the contributions of intravalley particle-hole pairs:

$$\chi^{(0)}(\mathbf{k}, \omega) \approx \chi_L^{(0)}(\mathbf{k}, \omega) + \chi_R^{(0)}(\mathbf{k}, \omega) + \chi_Q^{(0)}(\mathbf{k}, \omega), \tag{4.13}$$

where $\chi_{\mathrm{V}}^{(0)}(\mathbf{k},\omega)$ is the polarizability contribution from intravalley transitions in valley V, with $V = L, R, Q$.

For illustration purposes, we consider occasionally the polarizability, the dielectric function and the density-density response functions stemming from only one or two valleys, even if such model systems are unphysical. Thus $\epsilon_V^{\mathrm{RPA}}(\mathbf{k},\omega)$ and $\chi_V^{\mathrm{RPA}}(\mathbf{k},\omega)$ are defined in terms of $\chi_V^{(0)}(\mathbf{k},\omega)$ in an obvious manner, where V is either L, R, or Q for the respective valley. Moreover, we also consider cases with only two valleys taken into account. Sometimes this is a physically relevant situation, e.g., when the system is electron-doped or charge-neutral and the magnetic field is large, sometimes a theoretical contrast. Then we define $\chi_{V_1+V_2}^{(0)}(\mathbf{k},\omega) = \chi_{V_1}^{(0)}(\mathbf{k},\omega) + \chi_{V_2}^{(0)}(\mathbf{k},\omega)$ and again $\epsilon_{V_1+V_2}^{\mathrm{RPA}}(\mathbf{k},\omega)$ and $\chi_{V_1+V_2}^{\mathrm{RPA}}(\mathbf{k},\omega)$ follow in analogy to Eq. 4.2.

Polarizability of the Linear Valleys

Based on Eq. 4.13 the determination of the density-density response of aI3 is reduced to the calculation of $\chi_Q^{(0)}(\mathbf{k},\omega)$ and $\chi_{L/R}^{(0)}(\mathbf{k},\omega)$. The polarizability of the quadratic valley is already presented in Eq. 4.6 and in App. D and App. E.1. In this chapter we calculate the bare polarizability of the linear valleys. The crucial difference with respect to the 2DEG is that now one must take into account the matrix structure of the Green's functions, which appears due to the spinorial wave function.

The field operators are ($\xi = \pm 1$) are given in terms of the spinorial wave functions

$$\Psi_\xi(\tilde{\mathbf{r}},t) = \sum_n \int \mathrm{d}q \Phi_{n,q}^\xi(\tilde{\mathbf{r}}) e^{-it\epsilon_n^{\mathrm{W}}} c_{\xi,n,q}, \tag{4.14}$$

$$\Psi_\xi^\dagger(\tilde{\mathbf{r}},t) = \sum_n \int \mathrm{d}q [\Phi_{n,q}^\xi(\tilde{\mathbf{r}})]^\dagger e^{-it\epsilon_n^{\mathrm{W}}} c_{\xi,n,q}^\dagger. \tag{4.15}$$

Note that $[\Phi_{n,q}^\xi(\tilde{\mathbf{r}})]^\dagger$ is a row vector. Here $c_{\xi,n,q}$ denotes the annihilation operator of particles in ξ valley, n Landau level index and q momentum; spin index is suppressed for simplicity. We use the orbitals that Eqs. B.1 and B.3 specified in the rotated, rescaled coordinate system of Eq. 2.32. Even if the computation is more convenient in the rotated, rescaled coordinate system, the figures of Sec. 4.3 are presented in the non-rotated, non-rescaled coordinate system.

First we compute the time-ordered Green's function, which is by definition

$$\begin{aligned}\mathcal{G}_{\xi}^{(0)}(\tilde{\mathbf{r}},\tilde{\mathbf{r}}',t) &= -i\left\langle \mathcal{T}\Psi_{\xi}(\tilde{\mathbf{r}},t)\otimes\Psi_{\xi}^{\dagger}(\tilde{\mathbf{r}}',0)\right\rangle \\ &= -i\Theta(t)\sum_{n',n}\int \mathrm{d}q\int \mathrm{d}q'\Phi_{n,q}^{\xi}(\tilde{\mathbf{r}})\otimes[\Phi_{n',q'}^{\xi}(\tilde{\mathbf{r}})]^{\dagger}e^{-it\epsilon_n^{\mathrm{W}}}\langle c_{\xi,n,q}c_{\xi,n',q'}^{\dagger}\rangle \\ &\quad +i\Theta(-t)\sum_{n',n}\int \mathrm{d}q\int \mathrm{d}q'\Phi_{n,q}^{\xi}(\tilde{\mathbf{r}})\otimes[\Phi_{n',q'}^{\xi}(\tilde{\mathbf{r}})]^{\dagger}e^{-it\epsilon_n^{\mathrm{W}}}\langle c_{\xi,n',q'}^{\dagger}c_{\xi,n,q}\rangle.\end{aligned} \tag{4.16}$$

Note that the time-ordered Green's function has a matrix structure, $\otimes$ denotes standard outer product of a column and a row vector. It is convenient to introduce the center of mass and relative coordinates, $\tilde{\mathbf{R}}=(\tilde{\mathbf{r}}+\tilde{\mathbf{r}}')/2$ and $\Delta\tilde{\mathbf{r}}=\tilde{\mathbf{r}}-\tilde{\mathbf{r}}'$. Then the Green's function is

$$\mathcal{G}_{\xi}^{(0)}(\tilde{\mathbf{R}},\tilde{\mathbf{p}},E)=\sum_{n}\int \mathrm{d}q\int \mathrm{d}\Delta\tilde{\mathbf{r}}e^{i\tilde{\mathbf{p}}\Delta\tilde{\mathbf{r}}}\frac{\Phi_{n,q}^{\xi}(\tilde{\mathbf{R}}+\frac{\Delta\tilde{\mathbf{r}}}{2})\otimes[\Phi_{n,q}^{\xi}(\tilde{\mathbf{R}}-\frac{\Delta\tilde{\mathbf{r}}}{2})]^{\dagger}}{E-\epsilon_n^{\mathrm{W}}+i\delta\mathrm{sgn}(\epsilon_n^{\mathrm{W}}-\epsilon_F)}. \tag{4.17}$$

The time-ordered response function in the rotated, rescaled coordinates is

$$\chi_{\xi}^{\mathrm{T}}(\tilde{\mathbf{k}},\omega)=-i\mathfrak{T}\mathfrak{r}\int\frac{\mathrm{d}E}{2\pi}\int\frac{\mathrm{d}\tilde{\mathbf{p}}}{(2\pi)^2}\mathcal{G}_{\xi}^{(0)}(\tilde{\mathbf{R}},\tilde{\mathbf{p}}-\frac{\tilde{\mathbf{k}}}{2},E)\mathcal{G}_{\xi}^{(0)}(\tilde{\mathbf{R}},\tilde{\mathbf{p}}+\frac{\tilde{\mathbf{k}}}{2},E+\omega). \tag{4.18}$$

Note that in the evaluation of Eq. 4.18 one can essentially follow the derivation applied in the case of 2DEG, however, here we have to take care of the matrix structure of the Green's function and execute the trace. The evaluation of the trace leads to the following equivalent expression

$$\begin{aligned}\chi_{\xi}^{\mathrm{T}}(\tilde{\mathbf{k}},\omega) &= \int\frac{\mathrm{d}\tilde{\mathbf{p}}}{(2\pi)^2}\sum_{n,n'}\int \mathrm{d}q\int \mathrm{d}q'\frac{\Theta(\epsilon_{n'}^{\mathrm{W}}-\epsilon_F)-\Theta(\epsilon_n^{\mathrm{W}}-\epsilon_F)}{\omega+\epsilon_n^{\mathrm{W}}-\epsilon_{n'}^{\mathrm{W}}+i\delta\mathrm{sgn}(\omega)}\times \\ &\quad\times\int \mathrm{d}\Delta\tilde{\mathbf{r}}[\Phi_{n',q'}^{\xi}(\tilde{\mathbf{R}}+\frac{\Delta\tilde{\mathbf{r}}}{2})]^{\dagger}e^{i(\tilde{\mathbf{p}}-\frac{\tilde{\mathbf{k}}}{2})\Delta\tilde{\mathbf{r}}}\Phi_{n,q}^{\xi}(\tilde{\mathbf{R}}+\frac{\Delta\tilde{\mathbf{r}}}{2})\times \\ &\quad\times\int \mathrm{d}\Delta\tilde{\mathbf{r}}'[\Phi_{n,q}^{\xi}(\tilde{\mathbf{R}}+\frac{\Delta\tilde{\mathbf{r}}'}{2})]^{\dagger}e^{i(\tilde{\mathbf{p}}+\frac{\tilde{\mathbf{k}}}{2})\Delta\tilde{\mathbf{r}}'}\Phi_{n',q'}^{\xi}(\tilde{\mathbf{R}}+\frac{\Delta\tilde{\mathbf{r}}'}{2}).\end{aligned}$$

To proceed, first we execute the matrix multiplication, then we evaluate the integrals with respect to $\Delta\tilde{\mathbf{r}}$ (see App. E.2 for the derivation), finally we apply Eq. 4.4, which amounts to a simple sign change. Then we arrive at the non-interacting polarization

function

$$\chi_{\xi}^{(0)}(\tilde{\mathbf{k}},\omega)=\frac{1}{2\pi\alpha^2\ell^2}\sum_{n'\leq n_L^F}\sum_{n>n_L^F}\left(\frac{|\mathcal{F}^{\xi}_{n,n'}(\tilde{\mathbf{k}})|^2}{\omega-\epsilon_n^{\mathrm{W}}+\epsilon_{n'}^{\mathrm{W}}+i\delta}+\frac{|\mathcal{F}^{\xi}_{n',n}(\tilde{\mathbf{k}})|^2}{-\omega-\epsilon_n^{\mathrm{W}}+\epsilon_{n'}^{\mathrm{W}}-i\delta}\right). \quad (4.19)$$

The corresponding form factors $\mathcal{F}^{\xi}_{n,n'}(\tilde{\mathbf{k}})$ are defined as follows

$$\begin{aligned}\mathcal{F}^{\xi}_{n',n}(\tilde{\mathbf{k}})=&\frac{1}{2}F^{n',n,\xi}_{|n'|,|n|}(\tilde{\mathbf{k}})+\frac{1}{2}\mathrm{sgn}(n)\mathrm{sgn}(n')F^{n',n,\xi}_{|n'|-1,|n|-1}(\tilde{\mathbf{k}})\\&+\frac{\xi\beta}{2}\mathrm{sgn}(n)F^{n',n,\xi}_{|n'|,|n|-1}(\tilde{\mathbf{k}})+\frac{\xi\beta}{2}\mathrm{sgn}(n')F^{n',n,\xi}_{|n'|-1,|n|}(\tilde{\mathbf{k}})\end{aligned} \quad (4.20)$$

for $n,n'\neq 0$. Similarly for $n\neq 0=n'$,

$$\mathcal{F}^{\xi}_{0,n}(\tilde{\mathbf{k}})=\frac{1}{\sqrt{2}}F^{0,n,\xi}_{0,|n|}(\tilde{\mathbf{k}})+\frac{\xi\beta}{\sqrt{2}}\mathrm{sgn}(n)F^{0,n,\xi}_{0,|n|-1}(\tilde{\mathbf{k}}); \quad (4.21)$$

and finally, for $n=n'=0$,

$$\mathcal{F}^{\xi}_{0,0}(\tilde{\mathbf{k}}) \;=\; F^{0,0,\xi}_{0,0}(\tilde{\mathbf{k}}). \quad (4.22)$$

Here we have introduced the functions $F^{n',n,\xi}_{|n'|,|n|}(\tilde{\mathbf{k}})$, which are defined in App. E.2. It is easy to check that $F^{n',n,\xi}_{|n'|,|n|}(\tilde{\mathbf{k}})=\left[F^{n',n,\xi}_{|n|,|n'|}(-\tilde{\mathbf{k}})\right]^*$. Note finally that $\chi_L^{(0)}(\mathbf{k},\omega)$ and $\chi_R^{(0)}(\mathbf{k},\omega)$ are related by the change of the sign of the tilt β.

4.2.3 Interaction Strength

Here we make a short comment on the possible appearance of correlated phases, including Wigner crystal phase in aI3, which might be the case when the interaction energy overcomes the magnitude of the kinetic energy. We characterize the relative strength of the interaction for each carrier type by the ratio between the interaction energy scale $E_{\mathrm{int}}=e^2/(4\pi\epsilon_0\epsilon_r l)$ and the kinetic energy scale E_{kin} at the characteristic length scale $l\approx 1/k^F$. The kinetic energy scale depends on the carrier type.

For the massive carriers, $E_{\mathrm{kin}}\propto l^{-2}$, and the ratio r_s depends on the Fermi wave vector,

$$r_s=\frac{E_{\mathrm{int}}}{E_{\mathrm{kin}}}=\frac{m_Q}{a_0\epsilon_r m_0 k_Q^F}\approx\frac{300}{\epsilon_r}. \quad (4.23)$$

For the estimate we have used the Fermi momentum as estimated for a specific sample in Subsec. 4.2.2. This ratio is traditionally called the Wigner-Seitz radius.

In contrast to the parabolic bands, the kinetic energy of massless Dirac carriers scales in the same manner as the interaction energy, $E_{\text{int}} \propto l^{-1}$, hence there is no characteristic length such as the Bohr radius. Indeed, the ratio between interaction and kinetic energy is independent of the electron density, and it may be characterized by a *fine structure constant* of $\alpha-(\text{BEDT-TTF})_2\text{I}_3$

$$\alpha_{\alpha-(\text{BEDT-TTF})_2\text{I}_3} = \frac{\alpha c}{\sqrt{v_x v_y}\epsilon_r} \approx \frac{20}{\epsilon_r}, \tag{4.24}$$

where $\alpha \approx 1/137$ is the fine structure constant of quantum electrodynamics. The origin of the rather large value of the ratio between the interaction and the kinetic energy is that the average Fermi velocity $\sqrt{v_x v_y} \approx 10^5$ m/s is an order of magnitude smaller than the corresponding velocity in graphene, see Ref. [75].

In view of this high value of the energy ratio for both the massless and massive carriers in aI3, one may expect the formation of correlated phases, such as the Wigner crystal. For the conventional 2D electron gas, $r_s \gtrsim 37$ is required to reach the Wigner crystal phase of the massive carriers [155]. This would require in turn a dielectric constant $\epsilon_r < 10$. To the best of our knowledge there is no available experimental value for ϵ_r in aI3, but we expect it to be such as to rule out the Wigner crystal. In the linear valleys, the high value of the dielectric constant compensates for the small Fermi velocity, in which case, just like in graphene, one would not expect an instability of the semimetalic phase [32], [78]. Throughout the following calculations in Sec. 4.3 we assume that the Wigner crystal can be discarded, and use $\epsilon_r = 10$.

4.3 Results and Discussion

The PHES and the collective modes of aI3 at low energies are determined by the two massless Dirac cones and the massive hole pocket. The way the three valleys contribute to the density-density response depends on the doping and the perpendicular magnetic field. For significant electron doping the massive band is full at zero temperature and

only the massless carriers contribute to the transport independently of the magnetic field. We discuss this case in Subsec. 4.3.1. In significantly hole-doped samples all valleys contribute. We consider this situation in Subsec. 4.3.2.

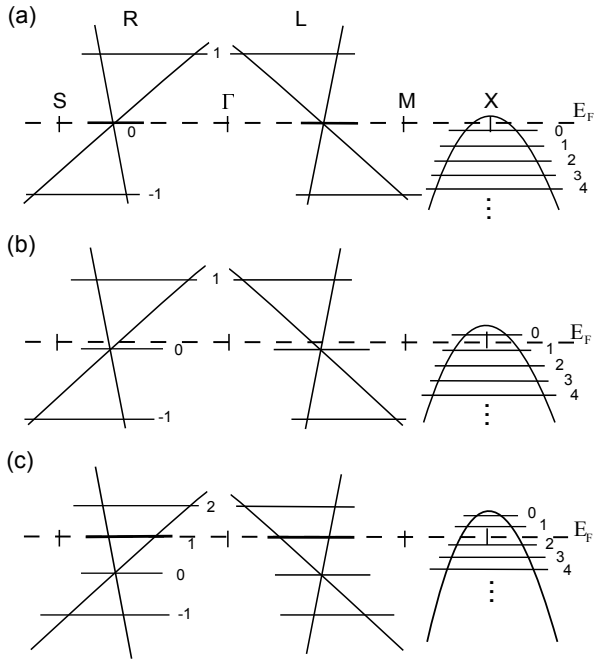

Figure 4.5: Schematic view of the Landau level structure of the two Dirac cones and the massive valley, with the chemical potential at charge neutrality indicated. (a) $B > B_{00} \approx 2.5$ T, (b) $B_{11} < B < B_{00}$, and (c) $B \lesssim B_{11} \approx 0.06$ T.

At charge neutrality the situation is more delicate. Then in zero magnetic field the chemical potential is between the Dirac point and the top of the massive band. By turning on the magnetic field, the central four-fold degenerate $n = 0$ LL of the massless valleys is fixed at the Dirac points, but the energy $E_{\text{offset}} - \hbar\omega_c/2$ of the topmost $n = 0$ LL of the massive valley decreases. Let B_{nm} be the field when the m-th LL of the massive valley coincides with the n-th LL of the conical valleys.

- For $B > B_{00}$, the $n = 0$ LL of the Dirac valleys is half-filled and the completely electron-filled massive valley is inert, see Fig. 4.5(a). The response is entirely due to the massless valleys and is discussed together with the electron-doped case in Subsec. 4.3.1.

- In the interval $B_{11} < B < B_{00}$ the chemical potential lies between the $n = 0$ LL of the linear band and the $n = 0$ LL of the massive band ($n_L^F = 0$, $n_Q^F = 1$),

as depicted in Fig. 4.5(b). The excess electrons in the massless valleys (two per flux quanta) exactly compensate for the excess holes in the massive pocket. Now all valleys contribute to the density-density response, this case is investigated in Subsec. 4.3.2.

- For $B \lesssim B_{11}$, the $n = 1$ LL of the massive valley becomes empty and the four-fold degenerate $n = 1$ LL of the massless Dirac valleys is half-filled; the chemical potential is set somewhere in the (naturally broadened) $n = 1$ LL of the massless Dirac fermions, see Fig. 4.5(c). Here again all the three valleys contribute, Subsec. 4.3.2 applies.

Combining Eqs. 4.7 and 4.9, we estimate $B_{11} \approx 0.06$ T and $B_{00} \approx 2.5$ T.

4.3.1 Response of the Massless Carriers

With a significant electron-doping in mind, we set $n_L^F = 2$ and $n_Q^F = 0$, i.e., the massive band is full and inert for all realistic values of the magnetic field B. We first examine the response of a single tilted massless Dirac cone with the intention to highlight the direction-dependent effects. Although this model is not directly related to a concrete physical situation, it reveals some basic phenomena associated with the tilt of the Dirac cones, such as the direction-dependent dispersion of the plasmon mode. This preliminary analysis within the single-cone approximation thus helps us understand the effect of the Coulomb coupling between the two different valleys, discussed in the second part of this subsection. Notice that for the electron-doped case the latter is actually the total density-density response.

The response of a single cone

Figures 4.6(a) and 4.6(b) show $\mathrm{Im}\chi_R^{\mathrm{RPA}}$ and $\mathrm{Im}\chi_L^{\mathrm{RPA}}$ in the direction of R's smallest velocity $\theta = \theta_{\mathrm{tilt}}$, where we have also plotted the boundaries $\omega_+^{R/L}$, $\omega_A^{R/L}$, $\omega_B^{R/L}$, and $\omega_{res}^{R/L}$, the latter corresponding to the frequency ω_{res} for the right and the left cone, respectively. The zero-field boundaries correctly describe the regions of allowed transitions also for non-zero magnetic fields since the wave vector in the PHES is that of (neutral) electron-hole pairs. It therefore remains a good quantum number also in the

presence of a magnetic field. Furthermore, we consider a finite broadening (inverse quasiparticle lifetime) $\delta = 0.1\hbar\sqrt{v_x v_y}/\ell$. Whereas treating δ as an energy-independent constant is a crude approximation,[6] we use it here only as a phenomenological parameter that renders the structure of the PHES more visible.

As shown in Fig. 4.6(a), the UHM is present with a considerable spectral weight in the originally forbidden region 1B of cone R in its tilting direction $\theta = \theta_{\text{tilt}}$. For cone L, on the other hand, the spectral weight in region 1B in the same direction is definitely smaller, contrary to the naive expectations. The low spectral weight is due to the high value of the dielectric constant $\epsilon_r \approx 10$ we choose on the basis of Sec. 4.2.3. In Fig. 4.7 we have plotted a zoom of $\text{Im}\chi_L^{\text{RPA}}$ in region 1B for different values of ϵ_r. It is apparent that the spectral weight could be increased considerably by lowering the dielectric constant ϵ_r, the reason is that the weakening of the bare interaction pushes the zeros of the RPA dielectric function to higher momenta at fixed energy; eventually the UHM is forced to the borderline of region 1B for cone L in the given direction. All in all, in the physically relevant situation low spectral weight is expected. For cone R the tendency is similar but less significant.

After leaving region 1B, the UHM merges into the linear magnetoplasmon mode in region 2B. The concentration of the spectral weight near ω_{res} is in accordance with the $B = 0$ limit in [112] and the $B \neq 0$ behavior of graphene in [48]. Recall that the UHM arises due to the modification of the classical plasmons by cyclotron motion, see [27]. It does not require interband excitations, thus it forms by a transfer of spectral weight from the intraband PHES to the originally forbidden region 1B.

Observing the high energies in Fig. 4.6 we recognize the regular *island* structures, which is the alternation of the parts with high and low spectral weight in the (ω, k)-plane. Their structure in momentum space is exactly of the same origin as in the case of nontilted cones discussed in [132]. The islands appear as the underlying Laguerre polynomials of the form factors in Eqs. 4.20 to 4.22 between deep-lying and high-energy Landau levels have many zeros.

To summarize, the density-density response of a generic massless Dirac cone in

[6] As a consequence of this crude treatment $\text{Im}\chi_{R/L}^{(0)} \leq 0$ fails in generic directions in region 3A. But, $\text{Im}\chi_{R+L}^{(0)} \leq 0$ and $\text{Im}\chi_{R+L}^{\text{RPA}} \leq 0$, as required.

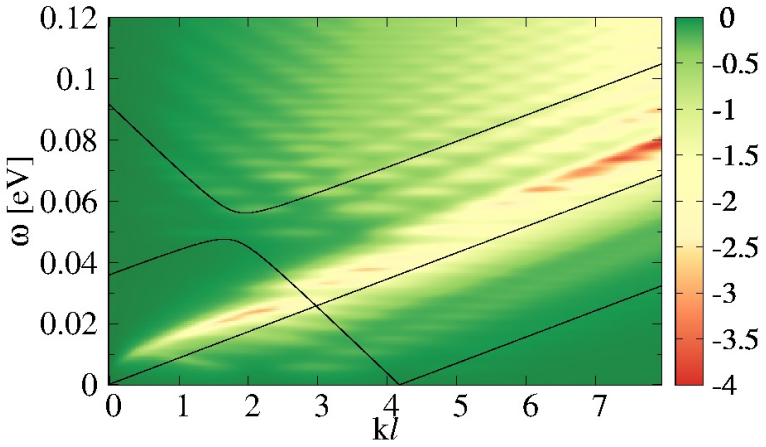

(a) $\mathrm{Im}\chi_R^{\mathrm{RPA}}$ in $\theta = \theta_{\mathrm{tilt}}$ or $\mathrm{Im}\chi_L^{\mathrm{RPA}}$ in $\theta = \theta_{\mathrm{tilt}} + \pi$

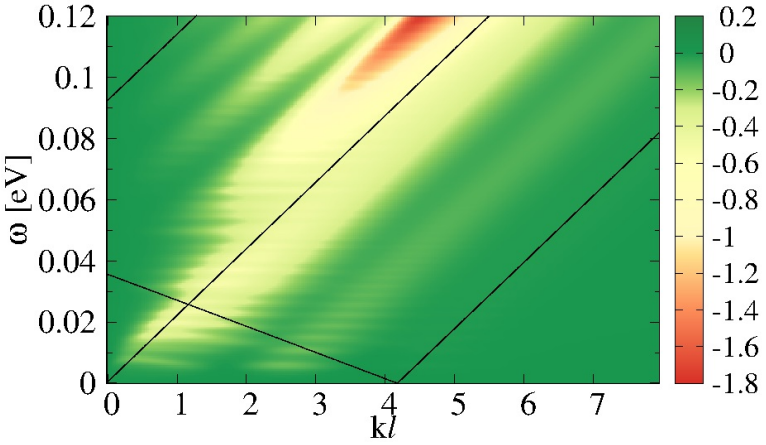

(b) $\mathrm{Im}\chi_L^{\mathrm{RPA}}$ in $\theta = \theta_{\mathrm{tilt}}$ or $\mathrm{Im}\chi_R^{\mathrm{RPA}}$ in $\theta = \theta_{\mathrm{tilt}} + \pi$

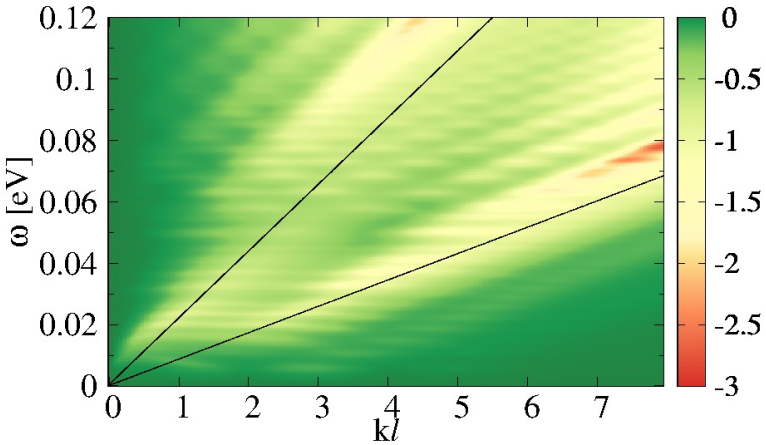

(c) $\mathrm{Im}\chi_{L+R}^{\mathrm{RPA}}$ in $\theta = \theta_{\mathrm{tilt}}$

Figure 4.6: The imaginary part of the density-density response of massless carriers, divided by the density of states at the Fermi energy. The topmost filled Dirac Landau level is $n_L^F = 2$, the other parameters are $B = 4$ T and $\epsilon_r = 10$. The first two panels consider the cones individually, while panel (c) shows $\mathrm{Im}\chi_{L+R}^{\mathrm{RPA}}$, which is the response of the total system for electron doping, or for $B > B_{00} \approx 2.5$ T at charge neutrality. The straight lines are the boundaries of regions relevant at $B = 0$. Notice that in panel (c), we have only depicted the lines $\omega_{res}^{R/L}$ for the two cones, as a guide to the eye.

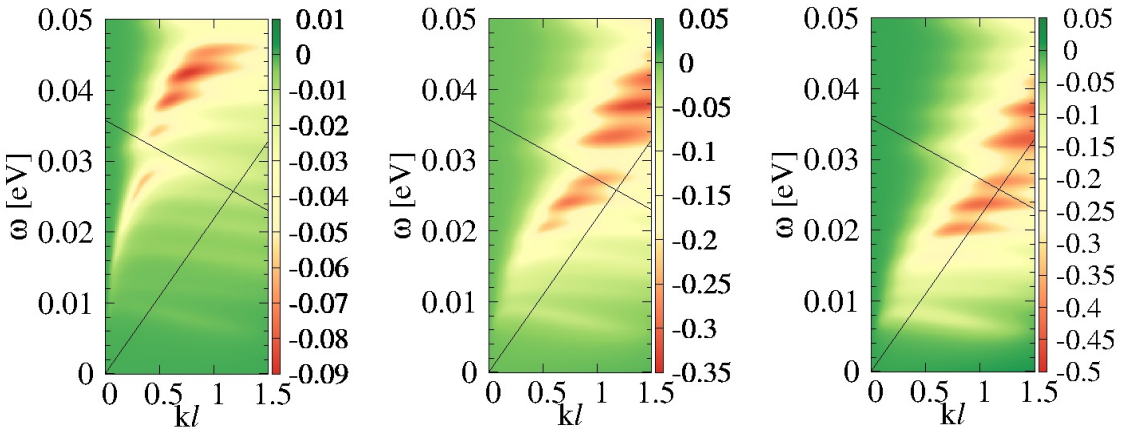

(a) $\epsilon_r = 1$ (b) $\epsilon_r = 4$ (c) $\epsilon_r = 7$

Figure 4.7: The dependence of the upper hybrid mode of massless Dirac fermions on the background dielectric constant ϵ_r. We show $\mathrm{Im}\chi_L^{\mathrm{RPA}}$ in $\theta = \theta_{\mathrm{tilt}}$ direction, which is the direction opposite to cone L's maximal tilt, for different ϵ_r. The physical parameters are the same as in Fig. 4.6(b), which depicts $\epsilon_r = 10$.

a perpedicular magnetic field exhibits an UHM and linear magnetoplasmons with anisotropic velocities, as a plausible generalization of the graphene case.

Both Cones Considered

Fig. 4.6(c) shows $\mathrm{Im}\chi_{L+R}^{\mathrm{RPA}}$ for both cones in a fixed direction $\theta = \theta_{\mathrm{tilt}}$ of the momentum plane. The UHM of cone R disappears, though it was the most dominant part of the response in the single-cone approximation. The UHM of cone L is still present, though with a reduced spectral weight in its own forbidden region. Its linear magnetoplasmon mode manifests itself, although at high energies (R's region 2B) it is surrounded by the interband particle-hole excitations of cone R, which have a modest spectral weight in the single cone approximation. Both modes are approximately in the same place as they were when only one cone was considered.

For interpretation, compare Fig. 4.4(c), where we sketch the (ω, k) plane in a fixed direction $\theta = \theta_{\mathrm{tilt}}$. The forbidden region of cone L lies entirely in that of cone R, hence no damping results from particle-hole excitations of either cones here. The picture is dramatically different for cone R: its forbidden region overlaps with the damped region of cone L, i.e., the UHM of cone R is strongly damped by particle-hole excitations in cone L. For this reason, the UHM of cone R disappears entirely. In the opposite direc-

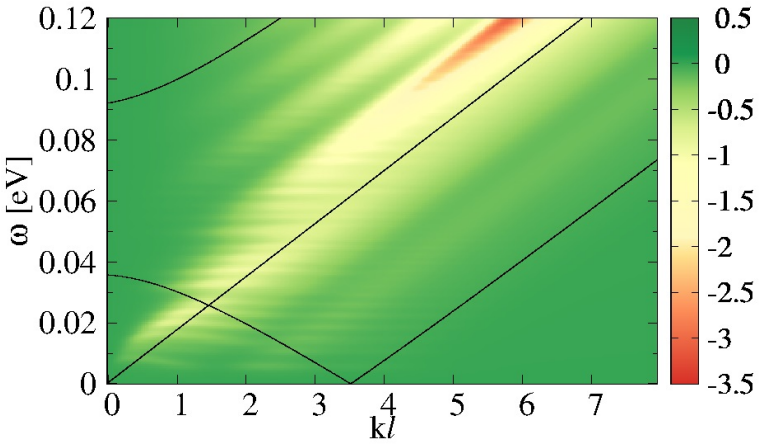

(a) $\mathrm{Im}\chi_R^{\mathrm{RPA}}$ in $\theta = \theta_{\mathrm{tilt}} + \pi/2$ or $\mathrm{Im}\chi_L^{\mathrm{RPA}}$ in $\theta = \theta_{\mathrm{tilt}} + 3\pi/2$

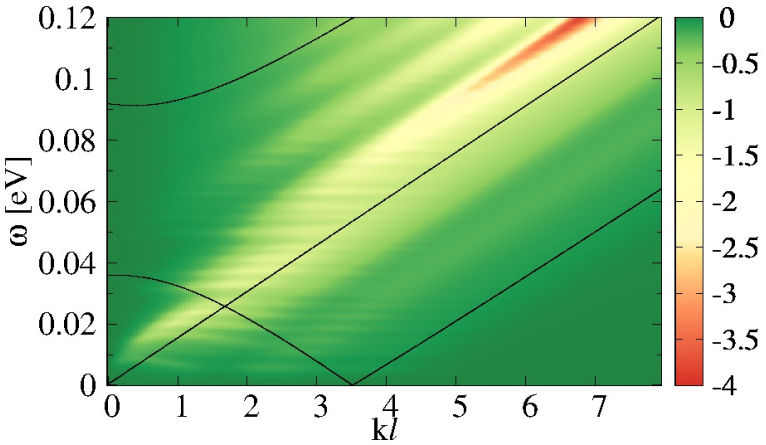

(b) $\mathrm{Im}\chi_L^{\mathrm{RPA}}$ in $\theta = \theta_{\mathrm{tilt}} + \pi/2$ or $\mathrm{Im}\chi_R^{\mathrm{RPA}}$ in $\theta = \theta_{\mathrm{tilt}} + 3\pi/2$

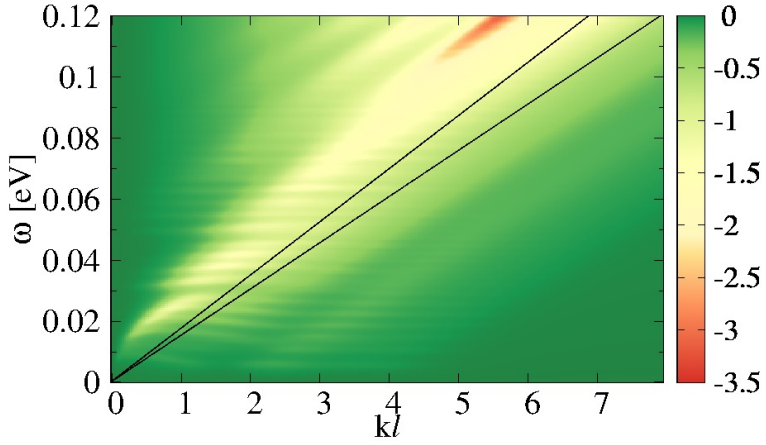

(c) $\mathrm{Im}\chi_{L+R}^{\mathrm{RPA}}$ in $\theta = \theta_{\mathrm{tilt}} + \pi/2$

Figure 4.8: The same as for Fig. 4.6, but for the direction perpendicular to the tilt.

tion the roles of L and R are, of course, interchanged. Therefore, the interaction of the two cones leads to a strong direction-dependent damping, which results in the complete suppression of the UHM of one cone where the other has particle-hole excitations of high spectral weight. This phenomenon, which we refer to as *intervalley damping*, is also visible in the imaginary part of the dielectric function (not shown).

The linear magnetoplasmons of each cone are situated in the particle-hole continuum of their own PHES respectively, where they are already damped. They do not overlap with each other in the (ω, k) plane in the shown direction $\theta = \theta_{\text{tilt}}$. Therefore, we expect the dominance of the one with higher spectral weight at a particular (ω, k). Figure 4.6(c) testifies the dominance of the linear magnetoplasmon mode of cone R in this direction, in agreement with its higher spectral weight in the single cone model. This explains the reappearance of the linear magnetoplasmons at larger momenta, and the disappearance of the linear magnetoplasmons of cone L for intermediate momenta.

Figure 4.8 shows the density-density response in the direction $\theta = \theta_{\text{tilt}} + \pi/2$, i.e., perpendicular to the direction of the minimal steepness of cone R or maximal steepness of cone L. The response of the individual cones are almost identical, see panels (a) and (b), and their forbidden regions practically coincide[7]. Intervalley damping is therefore absent in this direction. The UHM and the linear magnetoplasmon mode of the two-valley system in panel (c) are where they would be for a single cone; albeit with an increased amplitude.

In order to illustrate the phenomenon of intervalley damping in a more precise and quantitative manner, consider the bare polarizability in Eq. 4.13 of a multivalley model, which is generically written as

$$\chi^{(0)}(\mathbf{k}, \omega) = \sum_{V} \chi_V^{(0)}(\mathbf{k}, \omega), \tag{4.25}$$

where the sum runs over all different valleys. One may thus rewrite the RPA dielectric function as

$$\epsilon^{\text{RPA}}(\mathbf{k}, \omega) = \epsilon_{V_0}^{\text{RPA}}(\mathbf{k}, \omega) - v(\mathbf{k}) \sum_{V \neq V_0} \chi_V^{(0)}(\mathbf{k}, \omega), \tag{4.26}$$

[7]Perfect coincidence occurs at a nearby angle.

where $\epsilon^{\mathrm{RPA}}_{V_0}(\mathbf{k},\omega)$ is the RPA dielectric function within a single-valley model, where only the valley V_0 is taken into account. The single-valley model therefore yields a good approximation for the collective modes [given by the zeros of $\epsilon^{\mathrm{RPA}}(\mathbf{k},\omega)$] if

$$v(\mathbf{k}) \sum_{V \neq V_0} \chi^{(0)}_V(\mathbf{k},\omega) \simeq 0 \tag{4.27}$$

in the region of interest, i.e. for $\omega = \omega_{pl}(\mathbf{k})$ obtained from the solution $\epsilon^{\mathrm{RPA}}_{V_0}(\mathbf{k},\omega_{pl}) = 0$. This precisely means that the spectral weight for particle-hole excitations in the other valleys $V \neq V_0$ vanishes in this region, or else that the collective modes of V_0 survive in the forbidden regions of the other cones, as observed in our calculations.

Notice that the phenomenon of intervalley damping is absent if all individual polarizabilities $\chi^{(0)}_V(\mathbf{k},\omega)$ are identical, e.g., in the absence of a tilt of the (albeit anisotropic) Dirac cones. In this case, the RPA dielectric function in Eq. 4.26 simply becomes

$$\epsilon^{\mathrm{RPA}}(\mathbf{k},\omega) = 1 - g v(\mathbf{k}) \chi^{(0)}_V(\mathbf{k},\omega), \tag{4.28}$$

for g identical valleys. Therefore, $\epsilon^{\mathrm{RPA}}(\mathbf{k},\omega)$ has only a single zero, at a slightly larger frequency as compared to the single-valley approximation because of the enhanced coupling $v(\mathbf{k}) \to g v(\mathbf{k})$. This situation is encountered, e.g., when one takes into account the spin degeneracy in conventional electron systems ($g = 2$) or in graphene with non-tilted Dirac cones with a fourfold spin-valley degeneracy ($g = 4$). The tilt of the Dirac cones, or more generally the broken $\mathbf{k} \to -\mathbf{k}$ symmetry in a single valley, is thus the basic ingredient for the mechanism of intervalley damping.

4.3.2 Response within the Three-Valley Model

Undoped samples with $B < B_{00}$ and hole-doped samples allow us to study the contribution of the quadratic valley. In this subsection we investigate how this third valley damps the collective modes of the linear valleys, and how the collective mode of the massive valley appears alongside the excitations of the massless valleys. Recall from Sec. 4.1.2 that a 2D quadratic band has a plasmon mode that disperses $\propto \sqrt{k}$, and in a magnetic field, this mode becomes the gapped UHM, in the same manner as

for the linear bands.

Notice that the separation of the LLs scales as $\epsilon_n^{\mathrm{W}} \propto \sqrt{Bn}$ and $\epsilon_n^{\mathrm{Q}} \propto B$ for the massless and the massive carriers, respectively. One would therefore expect naively that the LLs of the quadratic valley are less dense in energy than those of the Dirac cones. However, due to the particular values of the Fermi velocities of the Dirac carriers and that of the band mass of the massive carriers, the LL separation of the massive carriers is much lower than that in the tilted Dirac cones in the magnetic-field range discussed here. Furthermore, the relative position of the collective modes of the massive and the massless valleys and the PHES of the three valleys are sensitive to both the magnetic field B and the doping level. Hence we discuss two representative cases, one at charge neutrality and relatively small magnetic fields $B < B_{00}$ (Fig. 4.9), and one at heavy hole-doping (Fig. 4.9). The two situations correspond to the sketches in Figs. 4.5(b) and (c), respectively.

We study the first case in Fig. 4.9, which depicts the density-density response at $n_L^F = 0$ and $n_Q^F = 1$, which is adequate at charge neutrality when $B_{11} < B < B_{00}$. We plot the direction $\theta = \theta_{\mathrm{tilt}}$, for which the difference between the velocities in the two cones is the most pronounced. In addition to the characteristic frequency $\omega_{res}^{R/L}$, we have also sketched the lines $\omega_+^Q(\mathbf{q})$ and $\omega_-^Q(\mathbf{q})$, which delimit the particle-hole continuum of the massive carriers.

As it is demonstrated in Figs. 4.9(a) and 4.9(b), where one of the cones is disregarded for visibility reasons, the particle-hole continuum of the quadratic valley lies well below the linear magnetoplasmon mode of the massless Dirac carriers in both cones. In other words, the particle-hole excitations of the massive carriers do not overlap with those of the Dirac valleys, and its spectral weight is comparable to the dominant linear magnetoplasmon modes of the latter. Thus the UHM of the massive holes cannot be damped either, as it lies at very small energies, well below the cyclotron frequency of the massless carriers.[8]

The total, physical density-density response in Fig. 4.9(c) indicates that the response of $\alpha-(\mathrm{BEDT\text{-}TTF})_2\mathrm{I}_3$ at low frequencies is determined by the massive carriers.

[8]The former is characterised by the energy scale $\epsilon_1^{\mathrm{Q}} \approx 0.001$ eV, while the latter by $\epsilon_1^{\mathrm{W}} \approx 0.015$ eV at $B = 2$ T.

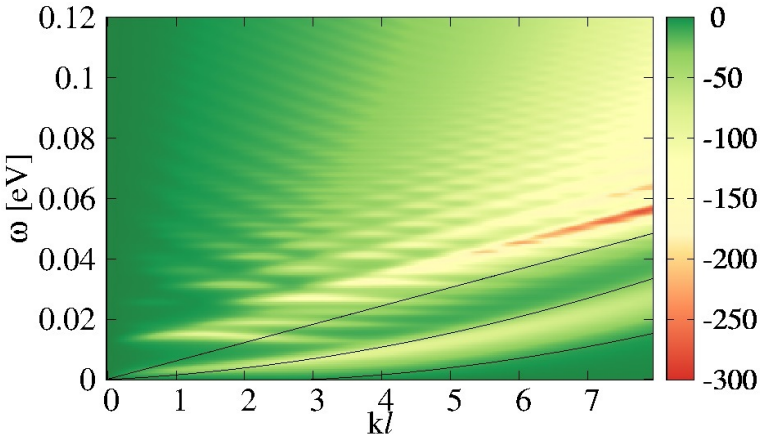

(a) $\mathrm{Im}\chi^{\mathrm{RPA}}_{R+Q}$

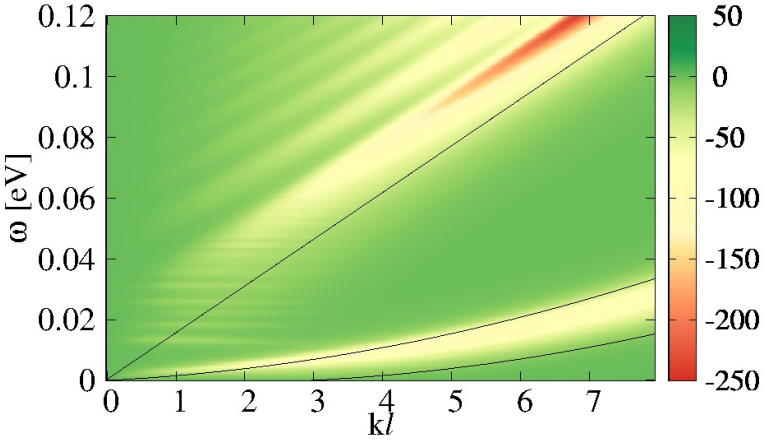

(b) $\mathrm{Im}\chi^{\mathrm{RPA}}_{L+Q}$

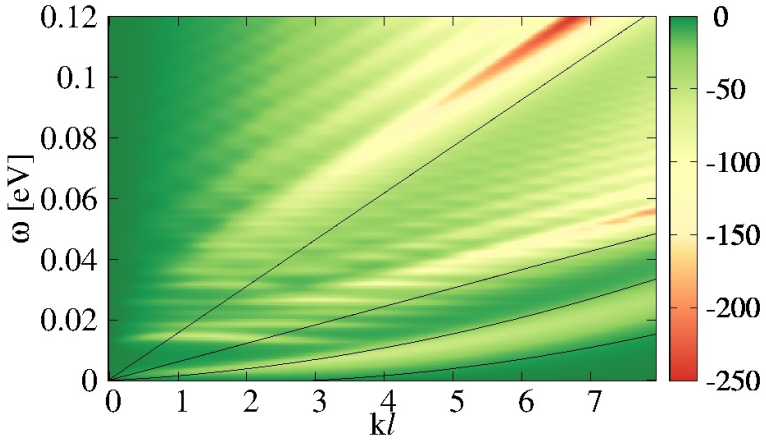

(c) $\mathrm{Im}\chi^{\mathrm{RPA}}$

Figure 4.9: The density-density response in direction $\theta = \theta_{\mathrm{tilt}}$ in momentum space. The topmost filled band is $n_L^F = 0$ in the massless valleys and $n_Q^F = 1$ in the massive valley. Other parameters are $B = 2$ T and $\epsilon_r = 10$. The units are s/m^2; normalization by the density of states is not applied. The straight line $\omega_{\mathrm{res}}^{R/L}$ is the boundary between the interband and intraband excitations of massless carriers, and the curved ones [$\omega_{\pm}^{Q}$ in Eq. 4.5] demarcate the particle-hole continuum of massive carriers for $B = 0$.

In the higher frequency range the Dirac carriers dominate, with intervalley-damped collective modes, as discussed above. The reason is the separation of energy scales at low momenta, and not any difference in the density of states.

Figure 4.10 shows the second case, a strongly hole-doped situation with $n_L^F = -2$ and $n_Q^F = 13$. Now the massive carriers are definitely involved in the damping. In direction $\theta = \theta_{\text{tilt}}$, the forbidden region 1B of cone R overlaps with the particle-hole continuum of the massive valley, see Fig. 4.10(a). Furthermore the UHM, which stems from the Dirac carriers, is found at a comparable energy as that associated with the massive carriers.[9] As a result, only one collective mode is discernible, which is damped once it enters the overlap region between the two lines ω_+^Q and ω_{res}^R, which is not a forbidden region for particle-hole excitations of the massive carriers. Furthermore, it is clear from Fig. 4.10(a) that the UHM avoids entering this region and rather approaches asymptotically the border ω_+^Q, as one expects for the UHM in a single-band model of massive carriers, for reference see [27, 46]. However, the situation is slightly more involved in the present case, where one observes a coupling between the UHM with the linear magnetoplasmons of the massless Dirac carriers, which gives rise to a modulation of the spectral weight along the UHM. This coupling is reminiscent to the so-called Bernstein modes discussed in the framework of graphene in a strong magnetic field in Ref.[134]. For cone L (or cone R in the $\theta = \theta_{\text{tilt}} + \pi$ direction), on the other hand, the forbidden region of the massive valley overlaps with the 1A intraband region of the massless valley. The UHM is therefore strongly damped and almost invisible at small momenta but reappears at $k\ell \gtrsim 4$, as visible in Fig. 4.10(b). This reappearance of the UHM, even if it occurs in a region of possible intraband particle-hole excitations of the massless Dirac carriers, may be understood from the particular chiral properties of the latter. Indeed, the spectral weight of particle-hole excitations, in the case of Dirac fermions, is concentrated around the lines ω_{res} due to the suppression of backscattering, ([5], [60], [78], [132], [140] and [165]) such that the UHM is barely damped once it is further away from ω_{res}.

In the regions where the allowed PHESs overlap, the one with the greater spectral

[9] At $B = 4$ T the cyclotron frequency is characterised by the energy scale $\epsilon_1^{\text{Q}} \approx 0.0023$ eV for the massive carriers, while by $\epsilon_1^{\text{W}} \approx 0.02$ eV for the massless ones.

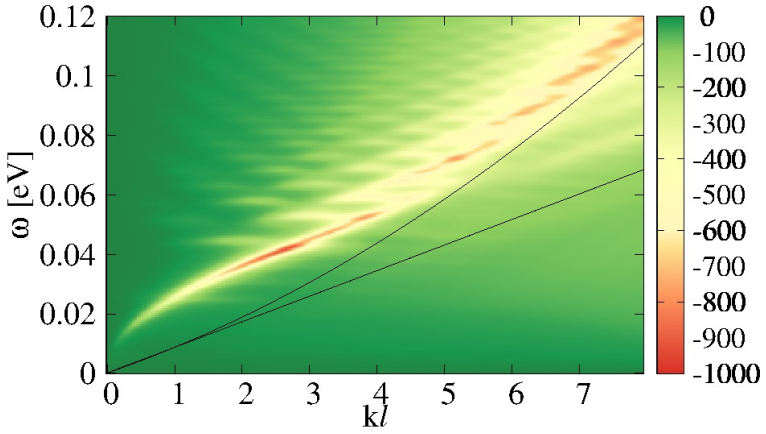

(a) $\mathrm{Im}\chi^{\mathrm{RPA}}_{R+Q}$

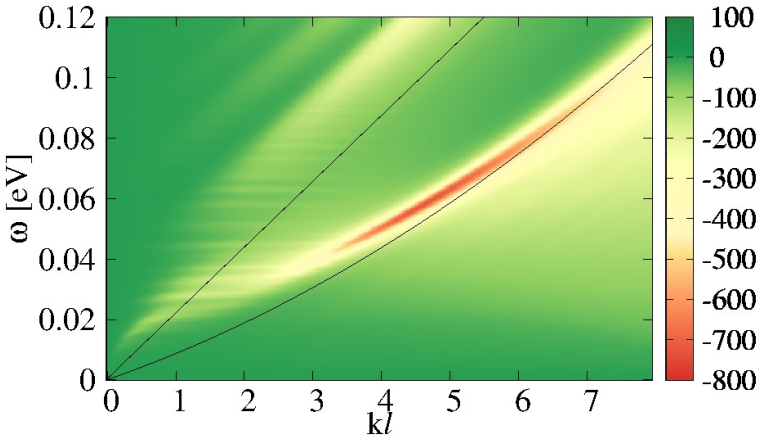

(b) $\mathrm{Im}\chi^{\mathrm{RPA}}_{L+Q}$

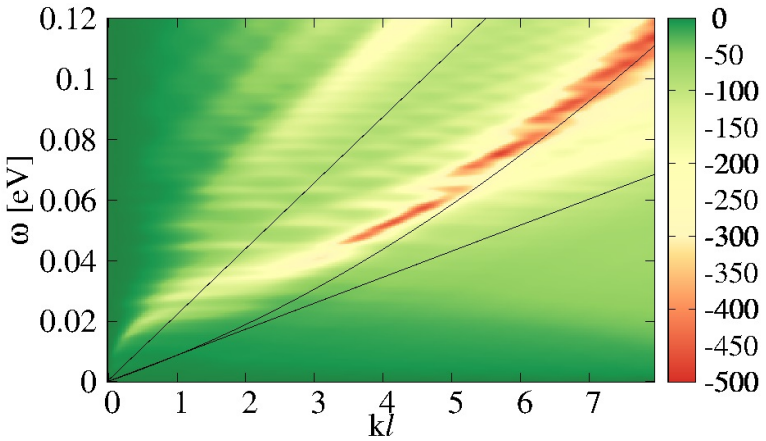

(c) $\mathrm{Im}\chi^{\mathrm{RPA}}$

Figure 4.10: The same as Fig. 4.9, but in a hole-doped sample. The topmost filled massless Landau level is $n_L^F = -2$, while among the massive LLs it is $n_Q^F = 13$. Other parameters are $B = 4$ T and $\epsilon_r = 10$. Notice that one of the curves demarcating the particle-hole continuum of the massive valley for $B = 0$, ω_-^Q in Eq. 4.5, is not visible because $2k_Q^F$ is outside of the presented momentum range.

weight dominates. This is visible in Fig. 4.10(a), where the particle-hole continuum of the massive valley is almost as bright as the more concentrated linear magnetoplasmon mode of the Dirac fermions. This also applies to the total, physical density-density response, Fig. 4.10(c), where the spectral weight is mostly concentrated on the excitations of the massive valley, although the linear magnetoplasmon of cone R become visible at large momenta.

4.3.3 Static Screening

The interplay between massless carriers in tilted anisotropic Dirac cones and massive holes in a roughly isotropic pocket gives rise to a remarkable doping-dependent angular dependence of the screening properties. Fig. 4.11 shows the real part of the

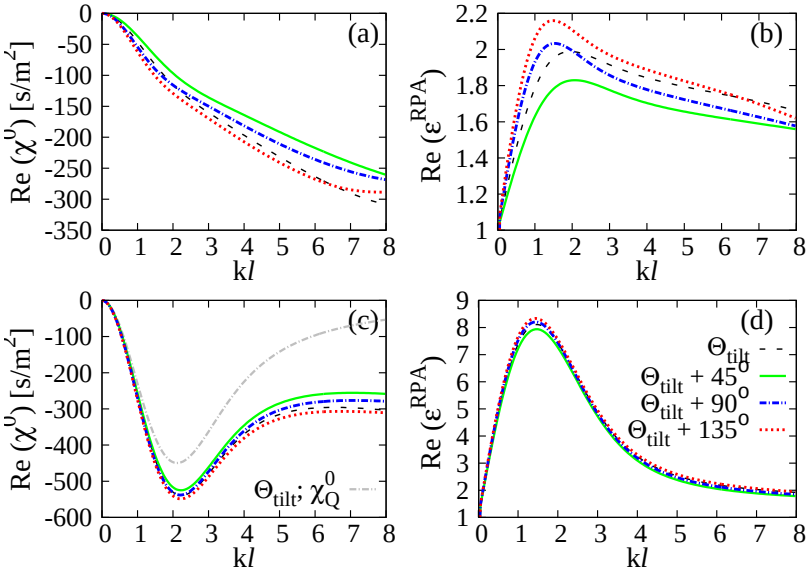

Figure 4.11: The static screening properties of $\alpha-(\text{BEDT-TTF})_2\text{I}_3$ at charge neutrality. Upper row: $B = 4$ T, the massive valley is completely filled and inert. Lower row: $B = 2$ T, the topmost Landau level of the massive valley is empty. Left panels: $\text{Re}\chi^{(0)}(\mathbf{k}, 0)$ in s/m^2, right panels: $\text{Re}\epsilon^{\text{RPA}}(\mathbf{k}, 0)$. We show several directions in the momentum plane, specified by the angle θ relative to θ_{tilt}, the tilting direction of cone R. The grey line in panel (c) shows the polarizability of the massive valley, which is dominant and suppresses any anisotropy due to the tilted Dirac cones if $B < B_{00}$.

static bare polarizability $\text{Re}\chi^{(0)}(\mathbf{k}, 0)$, and the dielectric function $\text{Re}\epsilon^{\text{RPA}}(\mathbf{k}, 0)$ in the RPA, respectively. For electron-doping or charge neutrality at $B > B_{00} \approx 2.5$ T,

the bare polarizability shown in panel (a) is entirely due to the linear bands. This anisotropy is naturally inherited by the RPA dielectric function depicted in panel (b), which means that screening due to the discussed bands is anisotropic. If the magnetic field is reduced, $B < B_{00}$, however, massive carriers can also be polarized at zero temperature. Because of their higher density of states at small energies, their contribution is dominant in the total polarizability, which shows a very weak angular dependence, see panel(c). As a result, screening is almost isotropic, see Fig. 4.11(d). The suppression of the anisotropic screening of the tilted cones by the massive valley naturally becomes stronger in hole-doped samples.

4.4 Conclusion

In this chapter we have studied the low-energy magnetic excitations and the collective modes of one conductive layer in aI3 within RPA. The low-energy band structure of this material under high pressure or uniaxial strain is well-described by our three-valley model, which assumes the presence of two tilted and anisotropic massless Dirac cones and a massive hole pocket, though there is some ambiguity regarding the band parameters and even the presence of massive carriers.

We have found that the tilt of the cones causes a direction-dependent intervalley damping of the upper hybrid modes of the Dirac valleys, while the linear magnetoplasmons are less affected. The magnetoplasmons of the massive band may coexist with those of the massless ones, depending on doping and the strength of the magnetic field. The latter also tunes the system between isotropic and anisotropic screening regimes.

Magnetoplasmons have been studied in graphene nanoribbons through infrared transmission spectroscopy in Ref. [131], besides infrared nano-imaging has been successfully used in Ref. [40], however, these type of experiments may be challenging under high pressure. On the other hand, the layered structure of these organic conductors recommends itself to inelastic light scattering experiments, which have successfully clarified the intrasubband plasmon modes of multilayer GaAs-(AlGa)As heterostructures. Details on the method and some early experiments are presented in [38],[63], [117] and [144].

Chapter 5

Magnetoexcitons - Bound Particle-Hole Pairs in Magnetic Field

5.1 Introduction

In this chapter we address the issue of the inter-Landau level excitations of bilayer graphene in the quantum Hall regime. As we have seen previously integer quantum Hall states in this material are fourfould degenerate due to spin and valley degeneracy, furthermore the $n = 0$ and 1 Landau levels are also degenerate, if Zeeman splitting is neglected, leading to an eightfold degenerate *central Landau band*. Thus IQH states appear at filling factor $\nu = \cdots, -8, -4, 4, 8, \cdots$ corresponding to Landau level indeces $n = \cdots, -3, -2, 1, 2, \cdots$. This peculiar Landau level structure is characteristic for bilayer graphene and served as a clue for its identification, see Ref. [115].

Besides the above IQH states with fully filled Landau levels, quantum Hall plateaus have also been observed at integer filling factors $\nu = 0, \pm 1, \pm 2$ and ± 3 through conductance measurements in Ref. [41], [36], [164] and [174] . Local compressibility measurements in [91] reinforced the above findings. In addition to those of the central Landau band, similar states have been observed in the $n = -2$ LL, see Ref. [8]. These states are all symmetry breaking states, they arise predominantly from many-body effects, notably due to the exchange interaction, single-body terms such as the Zeeman

energy play a secondary role. They are called quantum Hall ferromagnetic (QHF) states. Quantum Hall ferromagnetism emerge at odd integer fillings in two-component systems even if the Zeeman energy is tuned to zero. This observation straightforwardly generalizes for SU(n) systems [168].

If the chemical potential is in the gap between Landau bands, the filled and empty Landau bands are clearly separate, the low-energy excitations are magnetoexcitons.[1] The notion of these bound particle-hole pairs, which are obtained by promoting an electron from a filled Landau band to an empty band, and the resulting pair has zero net charge, was introduced and discussed in Ref. [23], [24], [66], [80] and [88]. In such states the hole and the particle are bound by the attractive Coulomb interaction, forming a dipole with a separation of $k\ell^2$ at center-of-mass wave-vector $\mathbf{k}$, where $k = |\mathbf{k}|$. They approach widely separated particle-hole pairs in the $k \to \infty$ limit. The latter limit determines the transport gap unless skyrmions form, see [42] and [143]. As the net charge of such an excitation is zero, taking appropriate linear combinations one obtains eigenstates of the total momentum.

In this chapter we examine magnetoexcitons of bilayer graphene both in case of fully filled Landau levels and QHF states. Because of the clear separation of the filled and empty Landau bands in the (mean-field) ground state, the excitations of both classes of quantum Hall systems are described in the same way. We exceed, however, the single particle picture and incorporate many body effects, e.g. screening of the interaction by Landau level mixing, that is we include the interaction-induced mixing of excitons between different Landau level pairs. This is inevitable as Henriksen *et al.* in [56] have found that fitting the single-body parameters does not fully explain the observed cyclotron resonance; Deacon *et al.* in [34] and Zou*et al.* in [175] have found a significant particle-hole asymmetry, whose origin is however still debated, see [138]. For inter-LL excitations, the many-body corrections to cyclotron resonance have been calculated by renormalization in [138] including the possible particle-hole symmetry-breaking terms but using the unscreened Coulomb interaction, with partial agreement

[1] Sometimes the intra-Landau level excitons are called spin waves or pseudospin waves, depending on the quantum numbers that distinguish the filled and the empty levels. The inter-LL excitons that conserve all quantum numbers are called magnetoplasmons, [25] and those that do not are dubbed spin-flip, valley-flip, or pseudospin-flip excitations, see [133]. We do not use these terms; the class of magnetoexcitons include all of these varieties.

with experiments of Ref. [56].

Some of these modes couple to circularly polarized light, as discussed in [2] in the $k \to 0$ limit. Here we study the finite wave-vector behavior of excitations, these may be observable in inelastic light scattering experiments, such as [39], [108], [124], [125], [126], [127], [128], [129] and [130].

The chapter is organized as follows. First, we briefly comment on the reasons why Kohn's theorem does not apply for bilayer graphene, then we review the adaptation of the mean-field theory of magnetoexcitons to the case of bilayer graphene. Afterwards, we study the excitations of the IQH states at filling factors $\nu = \pm 4, \pm 8, \pm 12$, then we discuss QHF states of the central Landau band. We conclude the chapter with an outlook on experiments and a short note on recent theoretical results.

5.2 A Note on Kohn's Theorem in Graphene and Bilayer Graphene

Kohn's theorem introduced in [76] states that interactions do not shift the cyclotron resonance in a parabolic band. It applies equally to 2D and 3D systems. It is not applicable to linear bands in monolayer graphene, see [133]. We will see that it also fails for bilayer graphene, even though the bands of $\hat{H}^{\xi}_{\mathrm{B}}$ in Eq. 2.24 start quadratically at low energies, and those of $\hat{H}^{\xi}_{\mathrm{B,\,eff.}}$ in Eq. 2.25 are exactly parabolic for $v_3 = u = 0$.

For the conventional 2DEG, Kohn's theorem follows because the interaction with a radiation field $\mathbf{A}^{\mathrm{rad}}$

$$\delta\hat{H}_{\mathrm{Q}} = \sum_i \frac{\mathbf{p}_i \cdot \mathbf{A}^{\mathrm{rad}}(\mathbf{r}_i)}{m_{\mathrm{Q}}},$$

where $\mathbf{p}_i$ is the canonical momentum that includes vector potential of the homogeneous magnetic field, is proportional to $P = P_x + iP_y$, where $P_x = \sum_i p_{i,x}$ and $P_y = \sum_i p_{i,y}$. P_x and P_y are generators of global translations, hence they commute with any translation-invariant interaction; moreover, $P, P^{\dagger}$ act as ladder operators among the eigenstates of the total kinetic energy, $\hat{H}_{\mathrm{Q}} = \sum_i \mathbf{p}_i^2/2m_{\mathrm{Q}}$. Therefore, $\delta\hat{H}_{\mathrm{Q}}$ connects eigenstates of the total Hamiltonian and conserves the interparticle interaction. $\mathbf{A}^{\mathrm{rad}}$ may be described classically or quantum mechanically; $[\delta\hat{H}_{\mathrm{Q}}, \hat{V}] = 0$ can also be checked directly, here

$\hat{V}(\mathbf{p})$ is the direct Coulomb interaction.

In the two-band model of bilayer graphene the interaction with the radiation field $\mathbf{A}^{\mathrm{rad}}$ is

$$\delta\hat{H}_{\mathrm{B,\,eff.}} \propto \sum_i \begin{pmatrix} 0 & [\mathbf{A}^{\mathrm{rad}}]^\dagger(\mathbf{r}_i)\pi_i^\dagger \\ \mathbf{A}^{\mathrm{rad}}(\mathbf{r}_i)\pi_i & 0 \end{pmatrix}$$

with $\mathbf{A}^{\mathrm{rad}} = A_x^{\mathrm{rad}} + iA_y^{\mathrm{rad}}$, see [2, 108]. It is straightforward to show that $\delta\hat{H}_{\mathrm{B,\,eff.}}$ maps a state $\Phi^{\mathrm{B}}_{n,q}$ to a linear combination of $\Phi^{\mathrm{B}}_{n+1,q'}$, $\Phi^{\mathrm{B}}_{n-1,q'}$, $\Phi^{\mathrm{B}}_{-n-1,q'}$ and $\Phi^{\mathrm{B}}_{-n+1,q'}$. If three out of these transitions are Pauli-blocked, we may end up in an eigenstate of the kinetic part of the many-body Hamiltonian, but $\delta\hat{H}_{\mathrm{B,\,eff.}}$ is no longer proportional to a linear combination of P_x and P_y. In fact, it no longer commutes with them. Thus the interaction energy may differ in the optically excited many-body state and the initial state.

5.3 Magnetoexcitons in Bilayer Graphene

Magnetoexcitons are created from the ground-state by operators

$$\hat{\Psi}^\dagger_{NN'}(\mathbf{k}) = \sqrt{\frac{2\pi\ell^2}{A}} \sum_p e^{ipk_y\ell^2} \hat{a}^\dagger_{Np}\hat{a}_{N'p-k_x}, \tag{5.1}$$

where $N = (n, \xi, \sigma)$ $[N' = (n', \xi', \sigma')]$ specifies the Landau band where the particle (hole) is created and A is the area of the sample, see [23], [24], [66], [80] and [88]. Each particle is characterized by its Landau level index n, valley index ξ and spin σ. These neutral excitations have a well-defined center-of-mass momentum $\mathbf{k}$.

Magnetoexcitons carry spin and pseudospin (valley) quantum numbers, as derived from the particle and hole Landau bands involved. While the projections S_z, P_z of the spin and the pseudospin are always good quantum numbers, their magnitudes S and P are well defined only for ground states that are spin or pseudospin singlets, respectively.

It is common practice to define the quantity

$$l_z = |n| - |n'|, \tag{5.2}$$

and consider it the *angular momentum quantum number* of the exciton, as done in [62], [66]. We emphasize that l_z is exactly conserved by the electron-electron interaction only in the $\mathbf{k} \to 0$ limit, where it is related to angular momentum. At any finite wave vector, transitions with different l_z may mix.

In the low magnetoexciton density limit the interaction between magnetoexcitons is neglected. The mean-field (Hartree-Fock) Hamiltonian of magnetoexcitons is well known from the literature, see [23], [24], [66], [80] and [88] and so is its adaptation to spinorial orbitals from Ref. [25],[62], [157]:

$$\begin{aligned} H^{(\tilde{N}\tilde{N}')}_{(NN')}(\mathbf{k}) &= \langle 0|\Psi_{\tilde{N}\tilde{N}'}(\mathbf{k})\hat{V}\Psi^{\dagger}_{NN'}(\mathbf{k})|0\rangle - \delta_{N\tilde{N}}\delta_{N'\tilde{N}'}\langle 0|\hat{V}|0\rangle \\ &= \delta_{N\tilde{N}}\delta_{N'\tilde{N}'}\left(E_{n\alpha\xi\sigma} - E_{n'\alpha'\xi'\sigma'} + \Delta(n,n')\right) + E^{(\tilde{N}\tilde{N}')}_{(NN')}(\mathbf{k}) + R^{(\tilde{N}\tilde{N}')}_{(NN')}(\mathbf{k}), \end{aligned} \tag{5.3}$$

where $N = (n, \xi, \sigma)$, etc., and $\delta_{NN'} = \delta_{\sigma\sigma'}\delta_{\xi\xi'}\delta_{nn'}$. $\hat{V}$ is the Coulomb interaction. The first term of the right hand side is the single-body energy difference of the N and N' states, which includes the wave vector independent exchange self-energy difference of the two states. While the exchange self-energy itself is infinite for any orbital, its difference between two states,

$$X_{N'N} = \frac{1}{(2\pi)^2}\int \mathrm{d}\mathbf{p} I^{N'N}_{N'N}(\mathbf{p}), \tag{5.4}$$

$$\Delta(N,N') = \sum_{M \text{ filled}} \left(X_{N'M} - X_{MN}\right), \tag{5.5}$$

is finite. This is a peculiarity of bilayer graphene in the absence of an interlayer bias u. A simple regularization procedure also works for the four-band model, the shift $\Delta(N,N')$ is analogous to the Lamb shift in quantum electrodynamics, as discussed in [139]. For monolayer graphene, a proper renormalization procedure is required, see [62], [138].

The next term is the direct dynamical interaction between the electron and the hole:

$$E^{(\tilde{N}\tilde{N}')}_{(NN')}(\mathbf{k}) = -\frac{1}{(2\pi)^2}\int \mathrm{d}\mathbf{q} e^{i\hat{\mathbf{z}}\cdot(\mathbf{q}\times\mathbf{k})} I^{N\tilde{N}}_{N'\tilde{N}'}(\mathbf{q}). \tag{5.6}$$

This term is diagonal both in spin and pseudospin, $\propto \delta_{\tilde{\sigma}\sigma}\delta_{\tilde{\xi}\xi}\delta_{\tilde{\sigma}'\sigma'}\delta_{\tilde{\xi}'\xi'}$, but not in Landau orbital indices. Finally, the last term in Eq. 5.3 is the exchange interaction between

the electron and the hole,

$$R^{(\tilde{N}\tilde{N}')}_{(NN')}(\mathbf{k}) = \frac{1}{2\pi\ell^2}\mathrm{Re}I^{NN'}_{\tilde{N}\tilde{N}'}(\mathbf{k}), \tag{5.7}$$

which is $\propto \delta_{\sigma\sigma'}\delta_{\xi\xi'}\delta_{\tilde{\sigma}\tilde{\sigma}'}\delta_{\tilde{\xi}\tilde{\xi}'}$, thus couples transitions that conserve the spin σ and the valley ξ of the electron and the hole individually. Sometimes we will call it the RPA contribution, as it is related to particle-hole annihilation and recreation processes.[2] Notice $R^{(\tilde{N}\tilde{N}')}_{(NN')}(\mathbf{k})$ vanishes in the $k \to 0$ limit.

We have used the notation

$$\begin{aligned} I^{N_2N_2'}_{N_1N_1'}(\mathbf{p}) = \quad & V^S(p)A^{(n_2')}_{\xi_2'}A^{(n_1)}_{\xi_1}A^{(n_1')}_{\xi_1'}A^{(n_2)}_{\xi_2}F^*_{|N_2||N_2'|}(\mathbf{p})F_{|N_1||N_1'|}(\mathbf{p}) \\ & +V^S(p)B^{(n_2')}_{\xi_2'}B^{(n_1)}_{\xi_1}B^{(n_1')}_{\xi_1'}B^{(n_2)}_{\xi_2}F^*_{|N_2|-2,|N_2'|-2,}(\mathbf{p})F_{|N_1|-2,|N_1'|-2}(\mathbf{p}) \\ & +V^D(p)A^{(n_2')}_{\xi_2'}B^{(n_1)}_{\xi_1}B^{(n_1')}_{\xi_1'}A^{(n_2)}_{\xi_2}F^*_{|N_2||N_2'|}(\mathbf{p})F_{|N_1|-2,|N_1'|-2}(\mathbf{p}) \\ & +V^D(p)B^{(n_2')}_{\xi_2'}A^{(n_1)}_{\xi_1}A^{(n_1')}_{\xi_1'}B^{(n_2)}_{\xi_2}F^*_{|N_2|-2,|N_2'|-2,}(\mathbf{p})F_{|N_1||N_1'|}(\mathbf{p}). \end{aligned}$$

The corresponding form factors are defined

$$F_{N'N}(\mathbf{q}) = \delta_{\sigma\sigma'}\delta_{\xi\xi'}\sqrt{\frac{n!}{(n')!}}\left(\frac{(-q_y+iq_x)\ell}{\sqrt{2}}\right)^{n'-n}L_n^{n'-n}\left(\frac{q^2\ell^2}{2}\right)e^{-q^2\ell^2/4} \tag{5.8}$$

if $n' \geq n$, else $F_{NN'}(\mathbf{q}) = F^*_{N'N}(-\mathbf{q})$. Here $|N|-2 \equiv (|n|-2,\xi,\sigma)$, $|N| = (|n|,\xi,\sigma)$, and $F_{N'N}(\mathbf{q})$ is related to the Fourier transform of the harmonic oscillator function $\phi_{n,q}(\mathbf{r})$ in Eq. 2.3. The difference between the intralayer Coulomb interaction $V^S(q) = 2\pi e^2/(4\pi\epsilon_0\epsilon_r q)$ and the interlayer one, $V^D(q) = e^{-qd}V^S(q)$ where $d \approx 0.335$ nm is the distance between the layers, is neglected as a first approximation. The $A^{(n)}_\xi$ and $B^{(n)}_\xi$ numbers correspond to the spinorial structure of the single-body states in Eq. 2.27: $A^1 = A^0 = 1$, $B^1 = B^0 = 0$, and $A^{(n)}_\xi = \mathrm{sgn}(n)B^{(n)}_\xi = 1/\sqrt{2}$ for $n \geq 2$. Notice that

$$E^{(\tilde{N}\tilde{N}')}_{(NN')}(\mathbf{k}) = E^{(NN')}_{(\tilde{N}\tilde{N}')}(\mathbf{k}) = E^{(\tilde{N}'\tilde{N})}_{(N'N)}(\mathbf{k}), \tag{5.9}$$

$$R^{(\tilde{N}\tilde{N}')}_{(NN')}(\mathbf{k}) = R^{(NN')}_{(\tilde{N}\tilde{N}')}(\mathbf{k}) = (-1)^{n+n'+\tilde{n}+\tilde{n}'}R^{(\tilde{N}'\tilde{N})}_{(N'N)}(\mathbf{k}), \tag{5.10}$$

[2] It is also called the depolarization term in [133].

which follow from the similar properties of $I^{N_2N_2'}_{N_1N_1'}(\mathbf{p})$.

The $k \to 0$ limit of the magnetoexciton dispersion determines the many-body contribution to the cyclotron resonance, which may be nonvanishing in graphene systems (see Sec. 5.2 and Refs. [133] and [138]).

The mean-field Hamiltonian matrix $H^{(\tilde{N}\tilde{N}')}_{(NN')}(\mathbf{k})$ in general mixes transitions among different electron-hole pairs, restricted only by conservation laws. Landau level mixing effectively screens the interaction. Nevertheless in Refs. [97] and [138] the magnetoexciton spectra are obtained using a screened model interaction instead of the bare Coulomb, not letting LL transitions mix. We believe such an approach is only suitable in the $k = 0$ limit, where an additional quantum number l_z also restricts LL mixing, and for intra-LL modes. At finite wave vector the mean-field theory with LL mixing removes spurious level crossings in the excitation spectra and provides insight into the orbital structure of the excitations. Technically, however, the infinite $H^{(\tilde{N}\tilde{N}')}_{(NN')}(\mathbf{k})$ matrix needs to be truncated.

5.4 Interaction Strength

The extent interactions may mix transitions involving different Landau level pairs depends on the interaction-to-kinetic energy ratio, parametrized by

$$r_s = \frac{e^2}{4\pi\epsilon_0\epsilon_r\ell}\Big/\hbar\omega_c \propto \frac{1}{\epsilon_r\sqrt{B}}. \tag{5.11}$$

Notice that $r_s \to 0$ in the $B \to \infty$ limit just like for the conventional two-dimensional electron gas. Realistically (10 T $\leq B \leq$ 40 T, $1 \leq \epsilon_r \leq 4$), $1 < r_s < 8$; this is by no means a small perturbation.

In the conventional 2DEG, LL mixing is suppressed at high fields because of the $B^{-1/2}$ scaling of the relative strength of interactions, while in monolayer graphene both the interaction and the kinetic energy scale with $B^{1/2}$, thus LL mixing is never suppressed. In bilayer graphene, the kinetic term of the Hamiltonian interpolates between quadratic at small momenta and linear at high momenta; thus, LL mixing gets suppressed only for the LL's with a small index, whose orbitals are built up from

low-momentum plane waves. For high-index LL's the ratio of interaction to kinetic energy is only weakly B dependent. At fixed magnetic field and filling factor, LL mixing in bilayer graphene is more significant than in a conventional 2DEG, because of the smaller dielectric constant and effective mass in bilayer graphene.

One can also compare the Coulomb energy scale, $e^2/(4\pi\epsilon_0\epsilon_r\ell)$ to the energy difference between adjacent Landau levels, $\hbar\omega_c\left(\sqrt{n(n-1)}-\sqrt{(n-1)(n-2)}\right)$. This may give the impression that LL mixing is more important at higher filling factors, but the amplitude of the undulations of the unmixed magnetoexciton dipersions also gets reduced in higher levels; leaving the issue of the generic progress of LL mixing with increasing filling factor open.

5.5 Integer Quantum Hall States

We first consider the IQH states, which occur when the highest LL is fully filled. Together with S_z and P_z, the magnitude of the spin S and of the pseudospin P are quantum numbers. (In the $\Delta_Z \to 0, u \to 0$ limit an SU(4) classification is also possible.) With the hole (n') and the electron (n) Landau orbitals fixed, the 16 possible transitions belong to 4 classes:

- A spin singlet, pseudospin singlet state:

$$\hat{\Psi}^{\dagger 00}_{nn'}(\mathbf{k}) = \frac{1}{2}\sum_{\xi}\sum_{\sigma}\hat{\Psi}^{\dagger}_{n\sigma\xi,n'\sigma\xi}(\mathbf{k}). \tag{5.12}$$

- A spin singlet, pseudospin triplet multiplet. The $P_z = 0$ member of this multiplet is

$$\hat{\Psi}^{\dagger 01}_{nn'}(\mathbf{k}) = \frac{1}{2}\sum_{\xi}\sum_{\sigma}\mathrm{sgn}(\xi)\hat{\Psi}^{\dagger}_{n\sigma\xi,n'\sigma\xi}(\mathbf{k}). \tag{5.13}$$

- A spin triplet, pseudospin singlet, which contains following the $S_z = 0$ state:

$$\hat{\Psi}^{\dagger 10}_{nn'}(\mathbf{k}) = \frac{1}{2}\sum_{\xi}\sum_{\sigma}\mathrm{sgn}(\sigma)\hat{\Psi}^{\dagger}_{n\sigma\xi,n'\sigma\xi}(\mathbf{k}). \tag{5.14}$$

- A nine-member multiplet that is triplet is both spin and valley. Its $S_z = 0 = P_z$

member is

$$\hat{\Psi}^{\dagger 11}_{nn'}(\mathbf{k}) = \frac{1}{2}\sum_{\xi}\sum_{\sigma}\mathrm{sgn}(\sigma)\mathrm{sgn}(\xi)\hat{\Psi}^{\dagger}_{n\sigma\xi,n'\sigma\xi}(\mathbf{k}). \tag{5.15}$$

Figure 5.1 depicts these modes for $\nu = -4$.

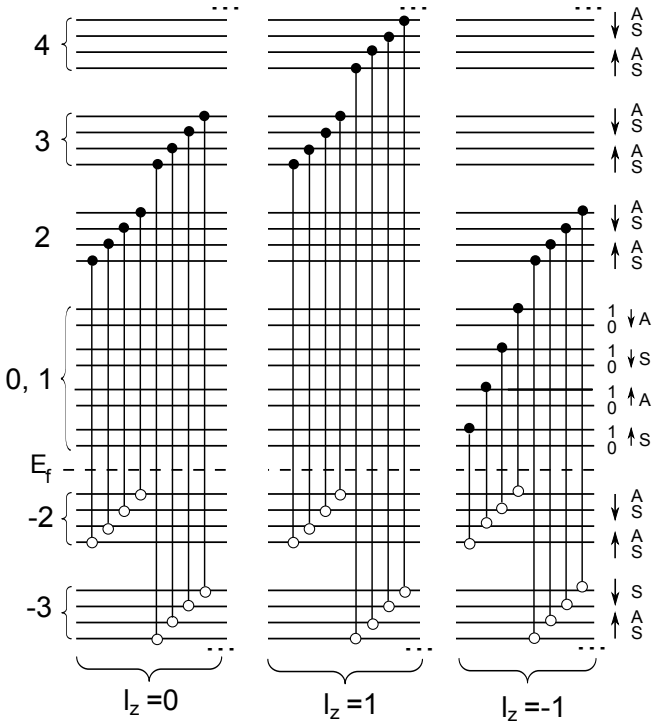

Figure 5.1: Magnetoexciton modes at the $\nu = -4$ integer quantum Hall effect in bilayer graphene. Only the optically relevant spin- and pseudospin-conserving modes are shown. In the $k \to 0$ limit, which is probed by purely optical experiments, the transitions in the infinite sequence at fixed $l_z = |n| - |n'|$ may mix; at $k > 0$, the excitations result from the mixing of all l_z sequences. The modes at $\nu = +4$ are obtained by particle-hole conjugation.

The exchange interaction between the electron and the hole contributes only to states generated by $\{\hat{\Psi}^{\dagger 00}_{nn'}\}_{nn'}$. In all other excitation modes the RPA term cancels or is prohibited by quantum numbers.[3] Thus in the absence of accidental degeneracies, we expect a collection of nondegenerate excitations and one of 15-fold degenerate excitations; the latter is decomposed as $4, 7, 4$ if $\Delta_Z > 0, u = 0$ and as $1, 2, 1, 2, 3, 2, 1, 2, 1$

[3]The RPA term cancels due sign alternation in modes $\hat{\Psi}^{\dagger 01}_{nn'}$, $\hat{\Psi}^{\dagger 10}_{nn'}$, and $\hat{\Psi}^{\dagger 11}_{nn'}$ One can easily check that the equal sign linear combination of the excitons created by the operators $(S\downarrow, S\uparrow)$ and $(A\downarrow, A\uparrow)$ is a pseudospin singlet, whereas the opposite sign linear combination is a member of a pseudospin triplet: Compare $P_-\hat{\Psi}^{\dagger}_{n\uparrow S,n'\uparrow S}|\mathrm{gs}\rangle$ with $\left(\Psi^{\dagger}_{n\uparrow S,n'\downarrow S} \pm \Psi^{\dagger}_{n\uparrow A,n'\downarrow A}\right)|\mathrm{gs}\rangle$, where P_- is the total pseudospin lowering operator and $|\mathrm{gs}\rangle$ is a ground state that is invariant for pseudospin rotation.

if $\Delta_Z, u > 0$.

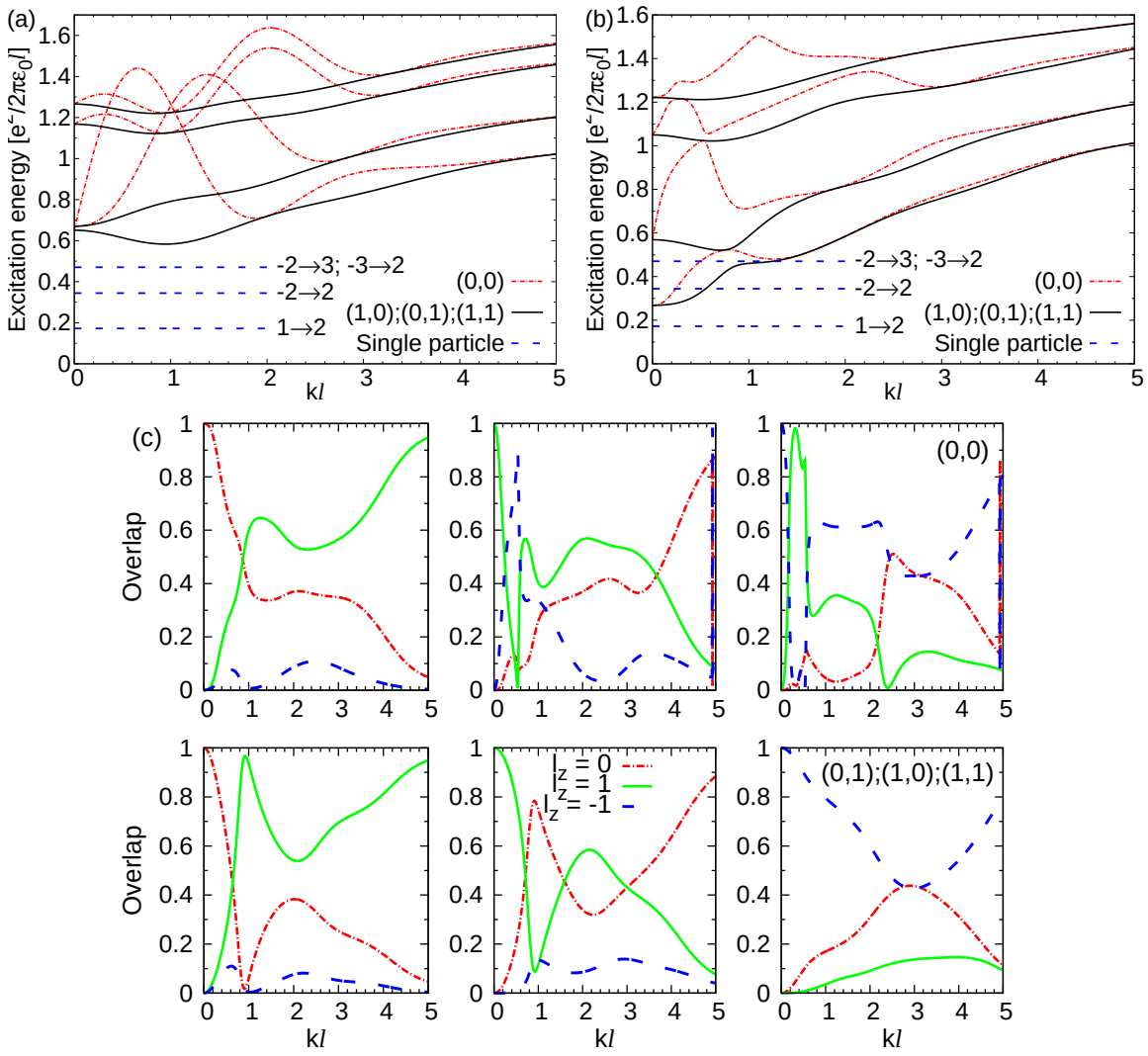

Figure 5.2: The excitations of the integer quantum Hall state at $|\nu| = 4$ and $B = 10$ T. Panel (a): spectra if Landau level mixing is neglected. Panel (b): The mixing of Landau levels is truncated at $L = 1$ and $M = 7$. Solid lines show the fifteen-fold degenerate excitations, which include three optically relevant $S_z = P_z = 0$ modes. Dashed lines show the spin and pseudospin singlets. Panel (c): the weight of the definite l_z projections in each curve in bottom-up order. The top row shows the spin and pseudospin singlets.

For $k = 0$, the mean-field Hamiltonian mixes magnetoexcitons with different electron and hole Landau levels at fixed l_z, and for $k > 0$ it also mixes different l_z subspaces. Restricting LL mixing to a fixed l_z subspace might give the impression that LL mixing is just a quantitative correction for the long wave length part of the lowest excitation curves, resulting in increased electron-hole binding energies, compare with [84] and

[106]. However, already the lowest excitations in the different l_z sectors mix strongly at finite wave vector. As the side panels of Fig. 5.2 show, the excitations have a large projection on the l_z subspaces different from their own l_z in the $k \to 0$ limit, and may eventually be contained in one of the other subspaces for large k; this is an unavoidable consequence of the elimination of crossings by LL mixing. The mixing of Landau levels is especially strong in the nondegenerate excitations, which are strongly affected by the exchange interaction between the electron and the hole (the RPA term) in the $k\ell \sim 1$ region. We allow the mixing of transitions restricted by $|l_z| \leq L$ and a maximum number M at each fixed l_z. Figure 5.2 shows transitions at $|\nu| = 4$ with $L = 1$ and $M = 7$, while Fig. 5.3 shows $|\nu| = 8$ and Fig. 5.4 $|\nu| = 12$, with the same truncation in both cases. We will use this truncation in all spectra shown in the rest of this chapter.[4] We also show the kinetic energy difference between the electron and the hole for comparison. Our mean field theory predicts an interaction shift comparable to this energy. This prediction will be revisited with methods beyond mean-field, this project is delegated to future work.

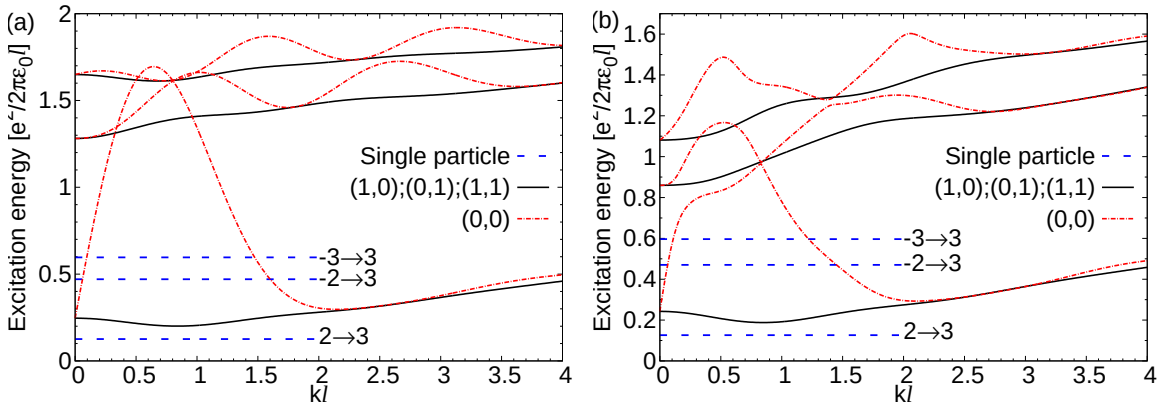

Figure 5.3: The excitations of the integer quantum Hall state at $|\nu| = 8$ at $B = 10T$. Panel (a): spectra if Landau level mixing is neglected. Panel (b): spectra with Landau level mixing.

The $k \to 0$ limit of the magnetoexcitons is commonly probed by optical absorption and electronic Raman scattering. The selection rules discussed in [2] and [108] ensure

[4] At $k = 0$ we have attempted an extrapolation of the excitation energies as a function of the cutoff M. The energies show a decreasing tendency, but fitting a power function has proved to be impossible, compare with [84]. We have chosen an ad-hoc cutoff at $M = 7$, with the understanding that small quantitative deviations are possible, especially at low energies. We have checked that using $M = 15$ does not fundamentally change the spectra.

that only the $\hat{\Psi}^{\dagger 00}_{nn'}$ mode and the $\hat{\Psi}^{\dagger 01}_{nn'}$, $\hat{\Psi}^{\dagger 10}_{nn'}$, and $\hat{\Psi}^{\dagger 11}_{nn'}$ modes of the 15-fold degenerate curve are active, $l_z = \pm 1$ is absorption, and $l_z = 0$ in Raman. Particle-hole conjugation relates $\nu = 4n$ to $\nu = -4n$ (n integer) with the sign of l_z reversed.

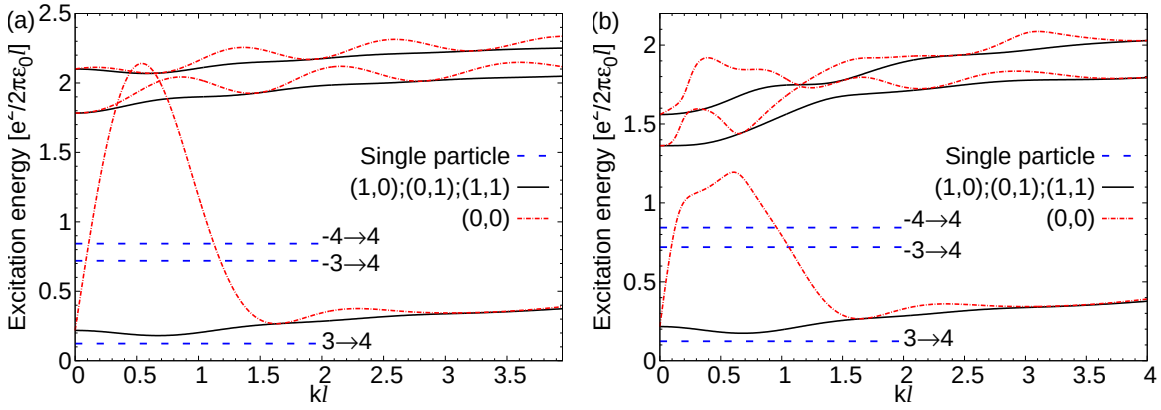

Figure 5.4: The excitations of the integer quantum Hall state at $|\nu| = 12$, at $B = 10T$. Panel (a): spectra if Landau level mixing is neglected. Panel (b): spectra with Landau level mixing.

5.6 Quantum Hall Ferromagnetic States

With an integer filling factor different from $\nu = \pm 4, \pm 8, \pm 12, \ldots$, a Landau band quartet ($|\nu| > 4$) or octet ($|\nu| < 4$) is partially filled in the single electron picture. The minimization of the interaction energy results in gapped states which break either spin rotation or pseudospin (valley) rotation symmetry, or both. These spontaneous symmetry breaking QHF states are discussed in [9],[10], [16], [30], [49], [50], [51], [157] and [168].

If either the Zeeman energy Δ_Z or the interlayer energy difference u is present, they affect the order how the Landau levels are filled, but exchange energy considerations are more crucial in most cases, see [9], [139]. The most convenient basis in pseudospin space may differ; we may introduce

$$\hat{a}_{nS\sigma p} = \cos\frac{\theta}{2}\hat{a}_{n,\xi=1,\sigma p} + \sin\frac{\theta}{2}e^{i\phi}\hat{a}_{n,\xi=-1,\sigma p}, \tag{5.16}$$

$$\hat{a}_{nA\sigma p} = \sin\frac{\theta}{2}\hat{a}_{n,\xi=1,\sigma p} - \cos\frac{\theta}{2}e^{i\phi}\hat{a}_{n,\xi=-1,\sigma p}. \tag{5.17}$$

With a proper choice of θ and ϕ, Eqs. 5.16 and 5.17 include states of definite valley, bonding and antibonding states, or intervalley phase coherent states. Corresponding magnetoexciton operators are defined in an obvious manner.

In particular, if $\Delta_Z > u$, the $\nu = 0$ QHF state is ferromagnetic and the choice of the pseudospin basis is irrelevant (Fig. 5.5). For $\nu = \pm 2$, both the $n = 0$ and $n = 1$ orbital Landau levels of identical spin and pseudospin are filled, where ϕ and θ are determined by electrostatics (Fig. 5.8). For odd ν, an interlayer phase coherent ($0 < \theta \leq \pi/2$) state exists for sufficiently small u, which yields to a layer polarized state ($\theta = 0$) at $\nu = -3$ and $\nu = 1$, and to a sequence of states with partial or full orbital coherence at $\nu = -1$ and $\nu = 3$, discussed in Refs. [10] and [30]. Notice that $\nu = -3$ and $\nu = 3$ are not related by particle-hole symmetry. This is best understood from Hund's rules derived by Barlas *et al.* in Ref. [9]: at $\nu = -3$ only one $n = 0$ orbital band is occupied, while at $\nu = 3$ only one $n = 1$ orbital band is empty. Côté *et al.* in [30] showed that at $\nu = 3$ orbitally coherent states dominate the phase diagram, whose inter-LL excitations are beyond the scope of this study. The case of $\nu = -3$ is depicted in Fig. 5.10.

Beyond S_z and P_z, the magnitudes P or S are quantum numbers at half-filling $\nu = 0$. All excitons include transitions between the non-central levels $|n| \geq 2$; the possibility of transitions from, to, or within the central Landau level octet depends on the ground state, which also resolves the transitions through the exchange self-energy differences; see Figs. 5.5, 5.8 and 5.10.

The excitations are grouped by their optical signature. Due to the small momenta of optical photons, valley flipping modes are optically inactive. In the $k \to 0$ limit l_z becomes a quantum number, and $l_z = \pm 1$ applies for single-photon absorption, and $l_z = 0, \pm 2$ in electronic Raman processes, with the $l_z = 0$ transitions being dominant. The angular momentum due to the helicity of the photons is transferred entirely to the orbital degree of freedom, see [2] and [108]. Optically inactive modes include Goldstone modes associated with the broken symmetry (outside the scope of our study) and generic dark modes.

5.6.1 $\nu = 0$

It is known that two QHF ground states exist: a spin-polarized one and a valley (layer) polarized one, as discussed in [9],[49], [50], [51], [72], [73], [157] and [164].[5] Their respective range of validity is determined by the ratio of the Zeeman energy Δ_Z to the energy difference between the valleys, which in turn is related to the potential difference u. (In fact, layer and pseudospin can be identified within the central Landau level octet.) For concreteness, we are discussing the ferromagnetic state. Here the magnitude of the pseudospin P is a good quantum number of the excitations. See Fig. 5.5 for the transitions that span the Hilbert space of the mean-field Hamiltonian.

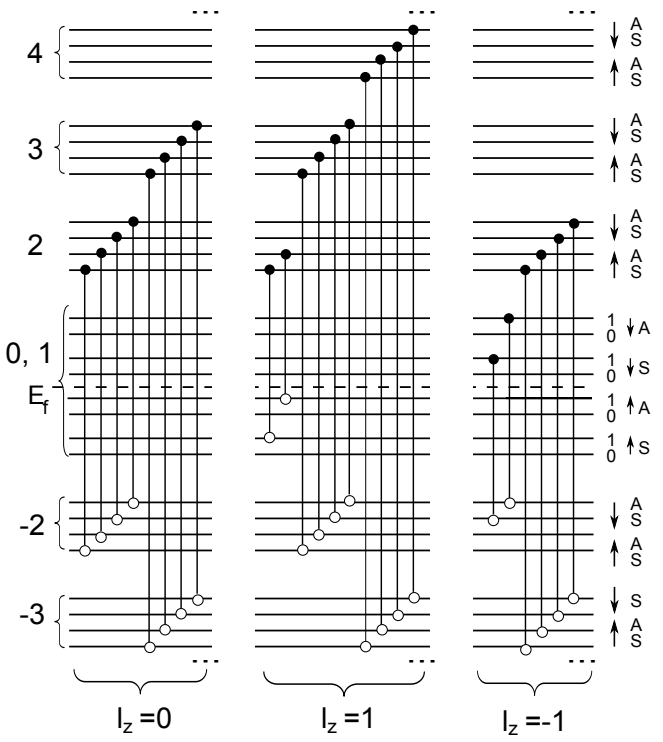

Figure 5.5: Magnetoexciton modes at the $\nu = 0$ quantum Hall ferromagnetic state in bilayer graphene. Only the optically relevant spin- and pseudospin-conserving modes are shown. In the $k \to 0$ limit, which is probed by photon absorption or electronic Raman, the transitions in the infinite sequence at fixed $l_z = |n| - |n'|$ may mix; at $k > 0$, the excitations result from the mixing of all l_z sequences.

[5] At certain values of the in-plane pseudospin anisotropy, which may arise due to electron-electron and electron-phonon interactions, two more phases are possible: a canted antiferromagnet and a partially layer polarized state, see Ref. [72]. These recently proposed states are beyond the scope of our study.

With the electron (n) and hole (n') Landau levels fixed, the $S_z = -1$ transitions consist of a pseudospin triplet $\Psi^\dagger_{nA\downarrow,n'S\uparrow}$, $\Psi^\dagger_{nS\downarrow,n'A\uparrow}$, $\frac{1}{\sqrt{2}}\left(\Psi^\dagger_{nS\downarrow,n'S\uparrow} - \Psi^\dagger_{nA\downarrow,n'A\uparrow}\right)$, and a singlet $\frac{1}{\sqrt{2}}\left(\Psi^\dagger_{nS\downarrow,S\uparrow} + \Psi^\dagger_{nA\downarrow,A\uparrow}\right)$. This group contains the intralevel transitions among the $n = 0, 1$ Landau bands; the Goldstone modes associated with the spin rotation symmetry breaking should be in this subspace. However, our approach is not appropriate for the description of Goldstone modes even at even filling factors, as we will discuss below.

The $S_z = 1$ pseudospin triplet, $\Psi^\dagger_{nA\uparrow,n'S\downarrow}$, $\Psi^\dagger_{nS\uparrow,n'A\downarrow}$, $\frac{1}{\sqrt{2}}\left(\Psi^\dagger_{nS\uparrow,n'S\downarrow} - \Psi^\dagger_{nA\uparrow,n'A\downarrow}\right)$, and pseudospin singlet $\frac{1}{\sqrt{2}}\left(\Psi^\dagger_{nS\uparrow,n'S\downarrow} + \Psi^\dagger_{A\uparrow,n'A\downarrow}\right)$, respectively, contains inter-LL transitions only.

The $S_z = 0$ sector consists of (i) two triplets, $\frac{1}{\sqrt{2}}\left(\Psi^\dagger_{nA\uparrow,n'A\uparrow} - \Psi^\dagger_{nS\uparrow,n'S\uparrow}\right)$, $\Psi^\dagger_{nA\uparrow,n'S\uparrow}$, $\Psi^\dagger_{nS\uparrow,n'A\uparrow}$, and $\Psi^\dagger_{nA\downarrow,n'S\downarrow}$, $\Psi^\dagger_{nS\downarrow,n'A\downarrow}$, $\frac{1}{\sqrt{2}}\left(\Psi^\dagger_{nS\downarrow,n'S\downarrow} - \Psi^\dagger_{nA\downarrow,n'A\downarrow}\right)$, which the RPA terms does not contribute to, and (ii) two singlets that are mixed by the RPA term: $\frac{1}{\sqrt{2}}\left(\Psi^\dagger_{nS\uparrow,n'S\uparrow} + \Psi^\dagger_{nA\uparrow,n'A\uparrow}\right)$ and $\frac{1}{\sqrt{2}}\left(\Psi^\dagger_{nS\downarrow,n'S\downarrow} + \Psi^\dagger_{nA\downarrow,n'A\downarrow}\right)$. Careful inspection reveals, however, that the two pseudospin singlets (ii) always appear in the mean-field Hamiltonian on equal footing, e.g., the $\frac{1}{\sqrt{2}}\left(\Psi^\dagger_{2S\uparrow,1S\uparrow} + \Psi^\dagger_{2A\uparrow,1A\uparrow}\right)$ transition is indistinguishable on the mean-field level from the $\frac{1}{\sqrt{2}}\left(\Psi^\dagger_{1S\downarrow,-2,S\downarrow} + \Psi^\dagger_{1A\downarrow,-2,A\downarrow}\right)$ transition. This follows by

$$E^{(2,1)}_{(2,1)} = E^{(1,-2)}_{(1,-2)}, \tag{5.18}$$

$$R^{(2,1)}_{(2,1)} = R^{(1,-2)}_{(1,-2)} = -R^{(1,-2)}_{(2,1)} = -R^{(2,1)}_{(1,-2)}, \tag{5.19}$$

and the following easily provable identity of the exchange self-energy cost:

$$\Delta(n,n') + X_{n'0} + X_{n'1} - X_{n,0} - X_{n,1} = \Delta(-n',-n). \tag{5.20}$$

(For $n = 1$ or $n' = 1$, no sign change is necessary.) Equation 5.20 simply expresses particle-hole symmetry, i.e., that the exchange self-energy cost of transitions related by particle-hole conjugation in a fixed component must be identical. See Fig. 5.6 for the transitions whose comparison yields Eq. 5.20.

The RPA terms are the same in each diagonal and off-diagonal position among equivalent transitions, thus they select the even and the odd linear combinations in

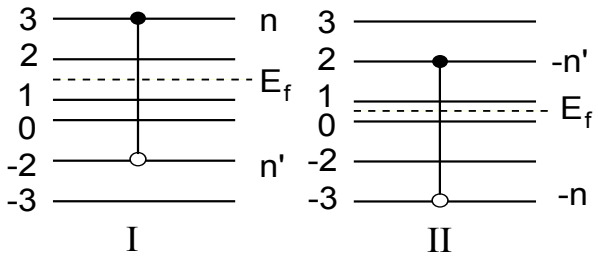

Figure 5.6: Imagine two transitions: (I) a particle in level n' is promoted to level n of a valley-spin component (left) of which the $n = 1$ Landau band is filled, and (II) $-n \to -n'$ of a component (right) of which the $n = 1$ band is empty. Particle-hole conjugation of (I) is the promotion of a hole from Landau level $-n'$ to $-n$, i.e., (II); the excitation energies must be the same. The consequence is Eq. 5.20; the formal proof is straightforward.

group (ii). The even combination, $\hat{\Psi}^{\dagger 00}_{nn'}(\mathbf{k})$ defined in Eq. 5.12, gets an RPA enhancement, while the RPA cancels from the alternating sign combinations, making it energetically equivalent to the $P_z = 0$ element of the triplets (i). Thus, eventually, the $S_z = 0, P_z = 0$ sector contains a three-fold degenerate curve and a nondegenerate mode.

Each of the four multiplets in the $S_z = 0$ sector contains a $P_z = 0$ mode, which is active in electronic Raman or IR absorption. Here the mixing of Landau levels results in more widely separated modes. The optically active excitations are shown in Fig. 5.7 with LL mixing taken into account. Notice that the $l_z = 1$ and $l_z = -1$ transitions have an equal weight in all modes, consistent with the particle-hole symmetry at $\nu = 0$.

In the $S_z = -1$ sector we find spin waves. Neglecting Landau level mixing, they give rise to a gapless and a gapped intra-LL mode [157], and a sequence of higher inter-LL modes; each of these is raised by the Zeeman energy and split by the valley energy difference in turn. The interaction, however, mixes these excitations, thus a clear-cut classification into intra-LL and inter-LL is no longer possible. Level repulsion unavoidably lowers the formerly gapless modes. This effect yields apparently negative excitation energies at small wavelength. Goldstone's theorem, however, ensures that a gapless spin-wave mode is associated with the breaking of the spin rotation symmetry. Consequently, the seemingly negative energy of the lowermost excitation with a large intra-LL component is an artifact of the combination of Hartree-Fock mean-field theory and LL mixing. The same anomaly occurs for monolayer graphene in [62] and [84] but it is less apparent when the particle-hole binding energy is plotted.

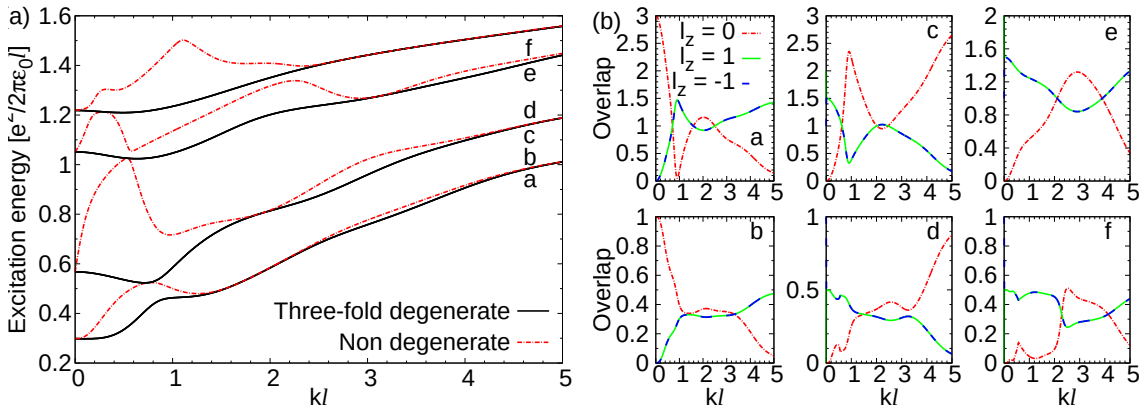

Figure 5.7: (a) Excitation spectra of the quantum Hall ferromagnet at $\nu = 0, \pm 2$ at $B = 10$ T. Only the optically relevant $S_z = P_z = 0$ modes are included. (b) The weight of the shown excitations on the definite l_z subspaces for $\nu = 0$ in bottom-up order. For degenerate curves the weight is summed. The quantum numbers of the $k \to 0$ limit are for curve a: $0^3; 1^0; -1^0$, curve b: $0^1; 1^0; -1^0$, curve c: $0^0; 1^2; -1^1$, curve d: $0^0; 1^0; -1^1$, curve e: $0^0; 1^2; -1^1$; and finally curve f: $0^0; 1^0; -1^1$.

5.6.2 $\nu = \pm 2$

The $\nu = \pm 2$ state breaks the spin and pseudospin rotational symmetries as the ground state fills the $n = 0$ and $n = 1$ orbitals of the most favorable spin-pseudospin component, $S\uparrow$. We restrict the discussion to spin and pseudospin preserving excitations. See Fig. 5.8 for the possible transitions.

It is easy to check that the mean-field Hamiltonian matrix is identical to the one at $\nu = 0$. For the $-n \to n$ transitions ($n \geq 2$ integer) this holds because the occupancy of the central Landau level octet is irrelevant as

$$X_{-n,0} + X_{-n,1} - X_{n,0} - X_{n,1} = 0. \tag{5.21}$$

The octet of $-(n+1) \to n$ and $-n \to (n+1)$ transitions gives rise to two quartets of equivalent transitions by Eqs. 5.18-5.20. While at $\nu = 0$ the $S\uparrow$ and $A\uparrow$ transitions of the former group bundle with the $S\downarrow$ and $A\downarrow$ transitions of the second group, now the $S\uparrow$ transition of the first group bundles with the $A\uparrow$, $S\downarrow$, and $A\downarrow$ transitions of the second group. The spectrum is still the one in Fig. 5.7(a). The orbital projection of the modes differs and is shown in Fig. 5.9 for $\nu = -2$. At $\nu = +2$ the sign of l_z changes in

all projections, which determines the helicity of the absorbed and inelastically scattered photons.

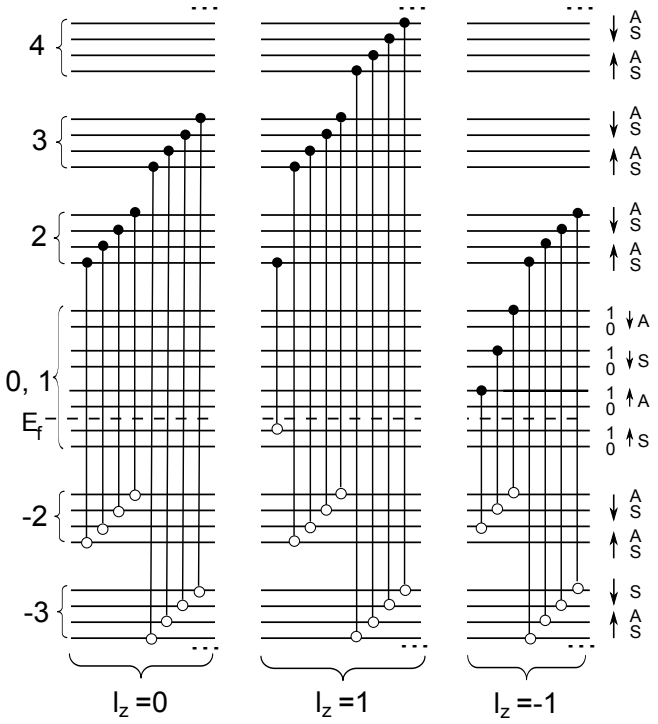

Figure 5.8: The spin- and pseudospin-conserving magnetoexciton modes at the $\nu = -2$ quantum Hall ferromagnetic state in bilayer graphene. The modes at $\nu = +2$ are obtained by particle-hole conjugation.

5.6.3 $\nu = -3$

Based on exchange energy considerations within the central Landau level octet, Hund's rule implies that the only occupied band is $(0, S\uparrow)$ at $\nu = -3$. The states in Eq. 5.16 progress from the layer balanced limit $\theta = \pi$ at $u = 0$ to the layer polarized state $\theta = 0$; this limit is achieved about $u = u_c \approx 0.001e^2/(4\pi\epsilon_0\epsilon_r\ell)$, which is only 0.082 meV at $B = 20$ T. For $0 < u < u_c$ there is interlayer phase coherence, see [10]. Thus magnetoexcitons exist on both side of u_c; the amount electrostatics raises energy of the pseudospin-flipping modes w.r.t. the pseudospin conserving modes saturates at $u = u_c$. Both the spin and the pseudospin symmetries are broken resulting in three Goldstone modes. Further, Barlas *et al.* in Ref. [10] showed that at finite u there is an instability to a stripe ordered phase with a rather small critical temperature. Our

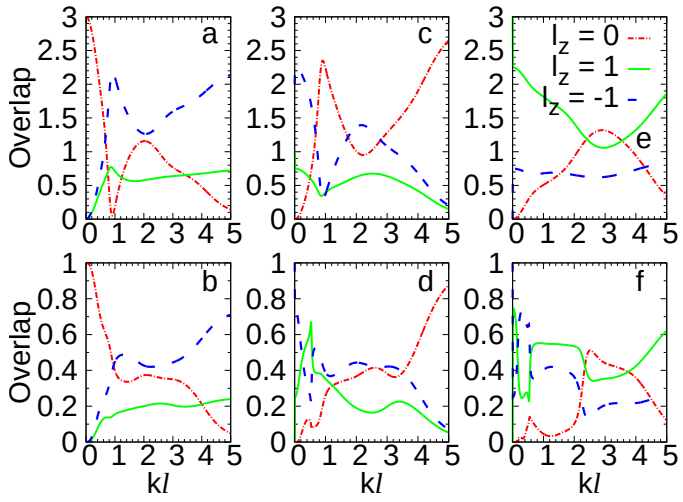

Figure 5.9: The projection of the excitations at $\nu = -2$ on the definite l_z subspaces. For degenerate curves the weight is summed. The spectrum at $\nu = \pm 2$ is identical to the one in the left panel of Fig. 5.7, the letters refer to the same curves. For $\nu = +2$ the sign of the $+l_z$ and $-l_z$ projections are interchanged w.r.t. $\nu = -2$. The quantum numbers of the $k \to 0$ limit are for curve a: $0^3; 1^0; -1^0$, curve b: $0^1; 1^0; -1^0$, curve c: $0^0; 1^1; -1^2$, curve d: $0^0; 1^0; -1^1$, curve e: $0^0; 1^3; -1^0$; and finally curve f: $0^0; 1^0; -1^1$.

following analysis applies only below this temperature. See Fig. 5.10 for the transitions that span the Hilbert space of the mean-field Hamiltonian.

Because of the degeneracy of $n = 0, 1$ orbitals, states in central Landau level octet at odd integer fillings involve fluctuations with in-plane electric dipole character [9]. The consequent collective modes have been studied in detail by Barlas *et al.* in [10] and Côté *et al.* in [30]. As we do not handle such dipolar interactions, we have omitted the predominantly intra-LL lowest curve from the spectra, and we have checked that the inter-LL excitation modes we keep contain the $0 \to 1$ magnetoexcitons with a negligible weight. Reassuringly, we always got a weight less than 0.1%.

As the $n = 0$ orbital is filled with $S \uparrow$ electrons in the mean-field ground state, for fixed electron (n) and hole (n') Landau levels the exchange self-energy cost of the $S \uparrow$ transition is higher than those of the other components. Also, in the $S \uparrow$ component an intralevel $0 \to 1$ transition is possible, which mixes with higher $S \uparrow$ transitions; see Fig. 5.10 for the restrictions on the possible transitions at this filling. The other three components, on the other hand, occur symmetrically in the mean-field Hamiltonian.

One can change basis from the excitons of type $S\downarrow$, $A\uparrow$ and $A\downarrow$ to

$$\hat{\Psi}^{\dagger d1}_{nn'} = \frac{1}{\sqrt{2}}\left(\Psi^{\dagger}_{nA\uparrow,n'A\uparrow} - \Psi^{\dagger}_{nA\downarrow,n'A\downarrow}\right), \tag{5.22}$$

$$\hat{\Psi}^{\dagger d2}_{nn'} = \frac{1}{\sqrt{6}}\left(\Psi^{\dagger}_{nA\uparrow,n'A\uparrow} + \Psi^{\dagger}_{nA\downarrow,n'A\downarrow} - 2\Psi^{\dagger}_{nS\downarrow,n'S\downarrow}\right), \tag{5.23}$$

$$\hat{\Psi}^{\dagger r}_{nn'} = \frac{1}{\sqrt{3}}\left(\Psi^{\dagger}_{nA\uparrow,n'A\uparrow} + \Psi^{\dagger}_{nA\downarrow,n'A\downarrow} + \Psi^{\dagger}_{nS\downarrow,n'S\downarrow}\right). \tag{5.24}$$

The RPA contribution cancels from $\hat{\Psi}^{\dagger d1}_{nn'}(\mathbf{q})$ and $\hat{\Psi}^{\dagger d2}_{nn'}(\mathbf{q})$, which give rise to doubly degenerate excitations. $\hat{\Psi}^{\dagger r}_{nn'}(\mathbf{q})$ has an RPA contribution. Its mixture with the distinguished $S\uparrow$ excitations produces nondegenerate curves. In higher energy excitations, on the other hand, the weight of the $0 \to 1$ transition of the $S\uparrow$ component becomes extremely small, thus the equivalence of the four components will be approximately restored, yielding threefold quasi-degenerate and nondegenerate curves.

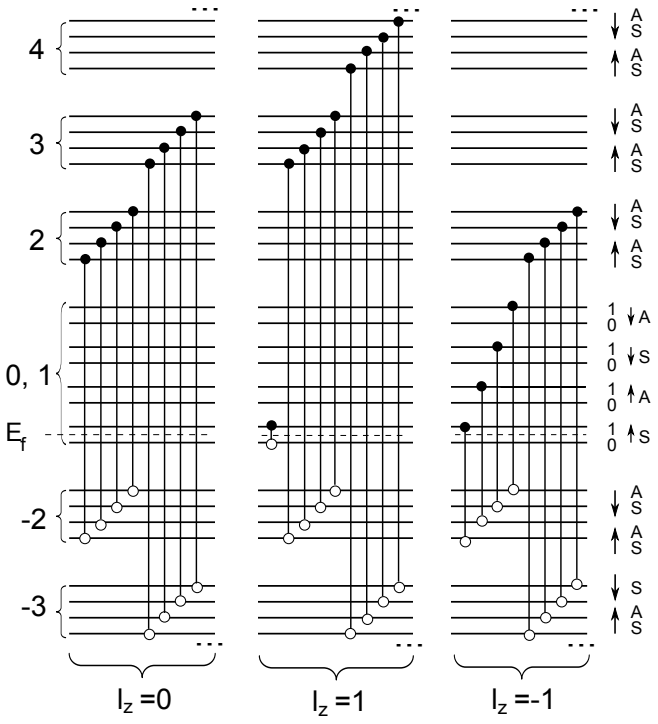

Figure 5.10: The optically spin- and pseudospin-conserving magnetoexciton modes at the $\nu = -3$ quantum Hall ferromagnetic state in bilayer graphene. Notice that the $S\downarrow$, $A\uparrow$ and $A\downarrow$ transitions occur symmetrically, i.e., the same electron and hole Landau levels are allowed and the same self-energy cost is picked up from the exchange with the filled levels.

See Fig. 5.11 for the dispersion of the active excitations. The small graphs show that the projection to definite l_z subspaces changes abruptly at nonzero wave vector. Notice that at higher energies $\gtrsim 1e^2/(4\pi\epsilon_0\epsilon_r\ell)$ the double degenerate curves occur in the vicinity of a nondegenerate one, indicating the approximate restoration of the equivalence of components in this limit.

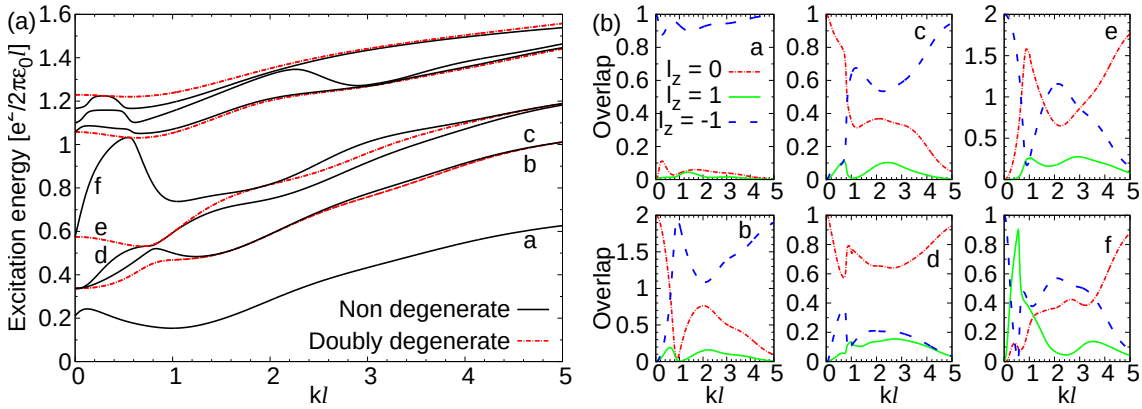

Figure 5.11: (a) Excitation spectrum of the quantum Hall ferromagnet in the $\nu = -3$ at $B = 10$ T. Only the optically relevant $S_z = P_z = 0$ modes are included. (b) The weight of the shown excitations on the definite l_z subspaces in bottom-up order. For degenerate curves, the weight is summed.

5.6.4 $\nu = 1$

Just like at $|\nu| = 3$, the state at $\nu = -1$ is not the particle-hole conjugate of the state $\nu = 1$. We do not study $\nu = -1$ because of the relevance of orbitally coherent states, discussed in [11].

At $\nu = 1$ the interlayer coherent and layer polarized QHF states both have magnetoexcitons. The possible transitions in the mean-field Hamiltonian are obtained trivially by raising the Fermi level by four levels in Fig. 5.10. Now the $S\downarrow$ electrons are distinguished by the possibility of an intralevel $0 \to 1$ transition, and their higher self-energy. The other three components occur symmetrically in the mean-field Hamiltonian. The argument is similar to the case of $\nu = -3$; for the two $1 \to 2$ transitions of spin-$\uparrow$ electrons and the $-2 \to 1$ transitions of the spin-$\downarrow$ electrons, one uses $R^{(2,1)}_{(1,0)} = -R^{(1,-2)}_{(1,0)}$ and Eq. 5.20. When subsequent $l_z = \pm 1$ transitions are included, the $-n \to (n+1)$ transition of $A\downarrow$ is equivalent to the $-(n+1) \to n$ transition of

$S\uparrow$ and $A\uparrow$, while the $-n \to (n+1)$ transition of $A\uparrow$ and $S\uparrow$ is equivalent to the $-(n+1) \to n$ transition of $A\downarrow$. The convenient basis change is similar to Eqs. 5.22 to 5.24, with $S\uparrow$ replaced by $A\downarrow$.

There is only a slight difference between the inter-Landau level excitation spectra at $\nu = -3$ and $\nu = 1$: the exchange self-energy cost of the distinguished transition ($S\uparrow$ at $\nu = -3$ and $S\downarrow$ at $\nu = 1$) relative to the three equivalent ones is $X_{n'0} - X_{n0}$ at $\nu = -3$ and $X_{n'1} - X_{n1}$ at $\nu = 1$. As this difference is already small for the lowest transitions and then decreases, we omit the $\nu = 1$ spectrum; its difference from Fig. 5.11(a) is comparable to the line width.

5.7 Conclusion

We have calculated the inter-Landau level magnetoexcitons in the integer quantum Hall states as well as the quantum Hall ferromagnets at filling factor $\nu = -3, \pm 2, 0, 1$ of bilayer graphene. We have found that the spinorial structure of the orbitals together with the enhanced electron-hole exchange interaction effects in this multicomponent system gives rise to rather complex dispersions; these are related both to the shape of the Fourier transform of Landau orbitals and to the elimination of crossings by the mixing of Landau levels, which is significant because the scale of the Coulomb energy is comparable to the cyclotron energies.

The $k \to 0$ limit of the excitation can be probed by optical absorption and electronic Raman experiments, see [2], [39] and [108]. Unlike for the conventional two-dimensional electron gas with a quadratic dispersion,where Kohn's theorem applies, the excitations in a quantizing magnetic field do acquire an interaction shift; the magnitude of such a shift is one of our experimental predictions.

The wave-vector dependence of the magnetoexcitons can be probed in resonant inelastic light scattering experiments of [126] where momentum conservation breaks down mainly because of ineffectively screened charged impurities. In semiconducting samples this technique has been successfully applied to the study of spin-conserving and spin-flipping excitations at integers as in [126], of the long wave-length behavior of the low-lying [125] and higher [130] excitations of fractional quantum Hall states, and

of magnetoroton minima at $\nu = 2$ [124] and [127], and at fractions [128]. In graphene, the magnetophonon resonance was observed by this method [129].

The mixing of transitions that involve different Landau levels is strong in the experimentally accessible range. This mixing smoothens the dispersion relations via level repulsion, and at finite wavelength causes a strong mixing of the modes that have different angular momenta in the zero wavevector limit. In particular, we have found that the anticrossings due to Landau level mixing result in a number of undulations in the magnetoexciton dispersions, whose van Hove singularities must give a strong signal [126].

On the theory side, we have found that the classification of magnetoexciton modes at finite wave vectors by the *angular momentum quantum number* is problematic, that the screening effects—which we have handled via Landau level mixing—are significant, and that this framework is not quite suitable for studying the Goldstone modes such as spin waves in the symmetry-breaking QHF states.

We note here that Shizuya in Ref. [139] derives a modified version of Hund's rule considering the exchange field due to all filled levels, not just those in the central Landau level octet. While this makes no difference for even filling factors, at $\nu = -3$ the predicted mean-field ground state fills a band of states which are equal linear combinations of $n = 1$ and $n = 0$ Landau orbitals. Ref. [158] confirmed that this novel version of the Hund's rule respects particle-hole symmetry and derived the corresponding ground states. The calculation of the excitations of such ground states is delegated to future work.

Thesis Statements

1. I have solved the eigenvalue problem of α-(BEDT-TTF)$_2$I$_3$ in a perpendicular magnetic field, if the material is placed in high hydrostatic pressure or uniaxial strain, that is the zero-gap state phase is realised, making use of the relativistic covariant nature of the underlying Dirac equation. I have drawn parallel between graphene in crossed magnetic and in-plane electric fields and the zero-gap state phase of α-(BEDT-TTF)$_2$I$_3$. I have pointed out that the electric field in the former system and the tilt in the latter one play essentially the same role, leading to tilted Dirac cones in both systems [III].

2. Handling graphene in a crossed magnetic and an electric fields and α-(BEDT-TTF)$_2$I$_3$ in a magnetic field together I have calculated the frequency dependence of the absorption coefficient. I have found that besides the dipolar optical transitions $\propto \delta_{|n|,|n|\pm1}$ in circularly polarized light, plenty of other optical transitions are possible due to rotational symmetry breaking. I have analyzed the structure of the emerging novel transitions, and I have shown that it leads to an oscillatory behaviour of the high-frequency tail of the absorption coefficient, which might be measurable in both systems. I have proposed a procedure to deduce experimental value for the tilt parameter in α-(BEDT-TTF)$_2$I$_3$ [III].

3. I have determined the collective excitations of α-(BEDT-TTF)$_2$I$_3$ in its zero-gap state phase in a perpendicular magnetic field within the random phase approximation. Assuming the presence of both massive and massless carriers in the low-energy band structure, I have demonstrated that by magnetic field and doping one can tune the system between a case where only the linear valleys contribute to the band structure to a case where all three valleys contribute. I have discovered that

in an electron-doped case this angular dependence leads to an anisotropic damping between the valleys: the particle-hole excitations of one valley damp the plasmonic mode of the other valley, even though the latter is in its proper forbidden region. I have pointed out that in a hole-doped case the massive band dominates the collective excitations of the system, and it also participates the damping processes between the valleys. I have analyzed how doping can effectively tune the system between isotropic and anisotropic screening regimes [II].

4. I have calculated the magnetoexciton dispersion relation of bilayer graphene in a perpendicular magnetic field in a mean-field picture. I have enumerated the possible magnetoexcitons both in the integer quantum Hall regime, where the highest Landau level is fully filled, and in cases with other integer filling factors that correspond to symmetry-breaking quantum Hall ferromagnetic states. I have demonstated that the cyclotron resonance is modified considerably by the inclusion of the Coulomb interaction especially at finite wave-vector. I have also pointed out that Landau level mixing leads to the elimination of level crossings, and that the mixing of transitions is especially strong in the interediate k range, which is accessible experimentally by inelastic light scattering [I].

List of Publications

[I] J. Sári and C. Tőke, Phys. Rev. B **87**, 085432 (2013).

[II] J. Sári, C. Tőke, and M. O. Goerbig, Phys. Rev. B **90**, 155446 (2014).

[III] J. Sári, M. O. Goerbig, and C. Tőke, arXiv:1502.07072 (2015).

Appendix A

Monolayer Graphene in a Perpendicular Magnetic Field

Here we briefly reproduce the derivation of the eigenvalues and eigenstates of Eq. 2.9 for cone K ($\xi = 1$) following [111]. The corresponding time independent Schrödinger equation is $\hat{H}_{\rm G}^{\xi=1}\Phi(x,y) = \epsilon\Phi(x,y)$. Due to the gauge choice $\mathbf{A} = (A_x, A_y, A_z) = (-yB, 0, 0)$ we make the ansatz for the spinorial wavefunction $\Phi(x,y) = e^{ikx}(\varphi(y)\ \upsilon(y))^{\rm T}$, where T denotes the transpose. Then

$$\hat{H}_{\rm G}^{\xi=1}\Phi(x,y) = \hbar v_F[p_x\sigma_x + p_y\sigma_y]\Phi(x,y) = \hbar v_F[(k - \frac{y}{\ell^2})\sigma_x + q_y\sigma_y]e^{ikx}\begin{pmatrix}\varphi(y)\\ \upsilon(y)\end{pmatrix}.$$

To proceed we introduce the variable $\tilde{y} = y - k\ell^2$. After canceling the exponential from the Schrödinger equation, and introducing the bosonic ladder operators $a = \frac{1}{\sqrt{2}\ell}(\tilde{y} + i\ell^2 q_{\tilde{y}})$ and $a^\dagger = \frac{1}{\sqrt{2}\ell}(\tilde{y} - i\ell^2 q_{\tilde{y}})$, which satisfy $[a, a^\dagger] = 1$,

$$\begin{pmatrix}0 & a\\ a^\dagger & 0\end{pmatrix}\begin{pmatrix}\varphi(\tilde{y})\\ \upsilon(\tilde{y})\end{pmatrix} = -\frac{\epsilon}{v_F\sqrt{2\hbar eB}}\begin{pmatrix}\varphi(\tilde{y})\\ \upsilon(\tilde{y})\end{pmatrix} \equiv \epsilon'\begin{pmatrix}\varphi(\tilde{y})\\ \upsilon(\tilde{y})\end{pmatrix}. \tag{A.1}$$

We are diagonalizing the Hamiltonian by taking the square of both sides of Eq. A.1. After some algebra, we get two decoupled equations as follows:

$$(1 + a^\dagger a)\varphi(\tilde{y}) = \epsilon'^2 \varphi(\tilde{y}), \tag{A.2}$$

$$a^\dagger a \upsilon(\tilde{y}) = \epsilon'^2 \upsilon(\tilde{y}). \tag{A.3}$$

In Eq. A.3 one recognizes the standard equation of the harmonic oscillator with $m = eB\hbar$ and $\omega = 1/\hbar$. From this analogy the eigenvalues of the Hamiltonian in Eq. 2.9 are

$$\epsilon_n^{\mathrm{G}} = \mathrm{sgn}(n)\sqrt{2|n|}\frac{v_F\hbar}{\ell}, \tag{A.4}$$

where n is an integer. The eigenfunctions are given in terms of the harmonic oscillator eigenfunctions

$$\upsilon(\tilde{y}) \equiv \phi_{|n|}(\tilde{y}) = \phi_{|n|}(y - k\ell^2). \tag{A.5}$$

Similarly, Eq. A.2 leads to a hamonic oscillator equation with the same eigenvalue, but with eigenfunction $\varphi(\tilde{y}) \equiv \phi_{|n-1|}(y - k\ell^2)$. The spinorial wavefunction $\Phi(x, y)$ should be looked for in the form

$$\Phi^{\mathrm{G},\xi=1}_{|n|,k}(x, y) = \frac{1}{\sqrt{2}}\frac{e^{ikx}}{\sqrt{2\pi}}\begin{pmatrix} \alpha\phi_{|n-1|}(y - k\ell^2) \\ \beta\phi_{|n|}(y - k\ell^2) \end{pmatrix} \tag{A.6}$$

with parameters α and β to be determined. Substituting the wavefunction into the Hamiltonian Eq. A.1, one deduces $\alpha = -\mathrm{sgn}(n)\beta$, and from the normalization condition we find $\beta = -1$. The final result is

$$\Phi^{\mathrm{G},\xi=1}_{|n|,k}(x, y) = \frac{1}{\sqrt{2}}\frac{e^{ikx}}{\sqrt{2\pi}}\begin{pmatrix} \mathrm{sgn}(n)\phi_{|n-1|}(y - k\ell^2) \\ -\phi_{|n|}(y - k\ell^2) \end{pmatrix}. \tag{A.7}$$

Appendix B

Eigenfunctions of α-(BEDT-TTF)$_2$I$_3$

For $n \neq 0$ in cone R the Landau orbitals are

$$\Phi_{n,k}^{\xi=1}(\tilde{\mathbf{r}}) = \frac{1}{\sqrt{4(1+\lambda)}} \left[\begin{pmatrix} -\beta \\ 1+\lambda \end{pmatrix} \phi_{n,k}^{\xi=1}(\tilde{\mathbf{r}}) + \begin{pmatrix} -1-\lambda \\ \beta \end{pmatrix} \mathrm{sgn}(n) \phi_{n-1,k}^{\xi=1}(\tilde{\mathbf{r}}) \right], \tag{B.1}$$

while for the $n = 0$ Landau level

$$\Phi_{0,k}^{\xi=1}(\tilde{\mathbf{r}}) = \frac{1}{\sqrt{2(1+\lambda)}} \begin{pmatrix} -\beta \\ 1+\lambda \end{pmatrix} \phi_{0,k}^{\xi=1}(\tilde{\mathbf{r}}). \tag{B.2}$$

For $n \neq 0$ in cone L, the orbitals are

$$\Phi_{n,k}^{\xi=-1}(\tilde{\mathbf{r}}) = \frac{1}{\sqrt{4(1+\lambda)}} \left[\begin{pmatrix} 1+\lambda \\ -\beta \end{pmatrix} \phi_{n,k}^{\xi=-1}(\tilde{\mathbf{r}}) + \begin{pmatrix} -\beta \\ 1+\lambda \end{pmatrix} \mathrm{sgn}(n) \phi_{n-1,k}^{\xi=-1}(\tilde{\mathbf{r}}) \right], \tag{B.3}$$

while for the $n = 0$

$$\Phi_{0,k}^{\xi=-1}(\tilde{\mathbf{r}}) = \frac{1}{\sqrt{2(1+\lambda)}} \begin{pmatrix} -1-\lambda \\ \beta \end{pmatrix} \phi_{0,k}^{\xi=-1}(\tilde{\mathbf{r}}). \tag{B.4}$$

We have used the subformulas ($\xi = \pm 1$)

$$\phi^{\xi}_{n,k}(\tilde{\mathbf{r}}) = \frac{e^{ik\tilde{x}}}{\sqrt{2\pi}} \frac{\lambda^{1/4}}{(2^{|n|}|n|!\sqrt{\pi}\alpha\ell)^{1/2}} e^{-\mathrm{Y}^2_{n,\xi}/2} H_{|n|}(\mathrm{Y}_{n,\xi}) \tag{B.5}$$

and

$$\phi^{\xi}_{n-1,k}(\tilde{\mathbf{r}}) = \frac{e^{ik\tilde{x}}}{\sqrt{2\pi}} \frac{\lambda^{1/4}}{(2^{|n-1|}|n-1|!\sqrt{\pi}\alpha\ell)^{1/2}} e^{-\mathrm{Y}^2_{n,\xi}/2} H_{|n-1|}(\mathrm{Y}_{n,\xi}),$$

with the argument

$$\mathrm{Y}_{n,\xi} = \sqrt{\lambda}\tilde{y}/\alpha\ell - \sqrt{\lambda}\alpha\ell k - \xi\beta\sqrt{2|n|}\mathrm{sgn}(n). \tag{B.6}$$

Notice that $\mathrm{Y}_{n,\xi}$ depends on both the LL index (including its sign) and the cone index ξ. Note also that Eqs. B.5 and B.6 use the same $\mathrm{Y}_{n,\xi}$ expression.

Appendix C

Dimensionless Matrix Elements

The evaluation of Eq. 3.4 amounts to, besides the standard matrix multiplication, the evaluation of the following integral:

$$\int \mathrm{d}\mathbf{r}\phi^*_{n,k}(\mathbf{r})\phi_{n',k'}(\mathbf{r}) = \int \mathrm{d}\mathbf{r}\frac{\sqrt{\lambda}}{2\pi\ell}\frac{e^{-ix(k-k')}}{\sqrt{2^{|n|+|n'|}|n'|!|n|!\pi}}e^{-\mathrm{Y}_n^2/2}e^{-\mathrm{Y}_{n'}^2/2}H_{|n|}(\mathrm{Y}_n)H_{|n'|}(\mathrm{Y}_{n'})$$

where the harmonic oscillator functions are defined in Eqs. 2.19 and 2.21. The integral with respect to x is straightforwardly evaluated leading to $\delta(k-k')$. To proceed, it is convenient to introduce a new variable $y' = \sqrt{\lambda}y/\ell - \sqrt{\lambda}\ell k$. With some algebra

$$\int \mathrm{d}\mathbf{r}\phi^*_{n,k}(\mathbf{r})\phi_{n',k'}(\mathbf{r}) = \frac{\delta(k-k')}{\sqrt{2^{|n|+|n'|}|n'|!|n|!\pi}}e^{-\beta^2(|n|+|n'|)/2}e^{\beta^2\sqrt{|n||n'|}\mathrm{sgn}(n)\mathrm{sgn}(n')}\times$$
$$\times\int \mathrm{d}y' e^{-\left(y'-\beta(\mathrm{sgn}(n)\sqrt{|n|}+\mathrm{sgn}(n')\sqrt{|n'|})/\sqrt{2}\right)^2}H_{|n'|}(y'-\beta\mathrm{sgn}(n')\sqrt{2|n'|})H_{|n|}(y'-\beta\mathrm{sgn}(n)\sqrt{2|n|})$$

After another change of variable of $y'' = y' - \beta(\mathrm{sgn}(n)\sqrt{|n|} + \mathrm{sgn}(n')\sqrt{|n'|})/\sqrt{2}$ the integral may readily be evaluated using the identity 7.377 of Ref. [52] with Laguerre-Hermite polynomials:

$$\int_{-\infty}^{\infty}\mathrm{d}x e^{-x^2}H_m(x+y)H_n(x+z) = \begin{cases} 2^n\sqrt{\pi}m!z^{n-m}L_m^{n-m}(-2yz) & m \le n, \\ 2^m\sqrt{\pi}n!y^{m-n}L_n^{m-n}(-2yz) & m > n. \end{cases} \quad \text{(C.1)}$$

Then the final result reads

$$\int \mathrm{d}\mathbf{r}\phi^*_{n,k}(\mathbf{r})\phi_{n',k'}(\mathbf{r}) = \begin{cases} \delta(k-k')F^{n,n'}_{|n|,|n'|} & |n| \geq |n'|, \\ \delta(k-k')F^{n',n}_{|n'|,|n|} & |n| < |n'|. \end{cases}$$

Here we find it convenient to introduce the function $F^{s,p}_{q,r}$ with integers s, p, q, and r defined as follows

$$F^{s,p}_{q,r} = \sqrt{\frac{r!}{q!}} e^{-\left(z^p_s\right)^2/2} \left(z^p_s\right)^{q-r} \; L^{q-r}_r\left(\left(z^p_s\right)^2\right), \quad z^p_s = \beta(\mathrm{sgn}(p)\sqrt{p} - \mathrm{sgn}(s)\sqrt{s}) \tag{C.2}$$

for $q \geq r$, otherwise $F^{s,p}_{q,r} = F^{p,s}_{r,q}$.

Appendix D

Derivation of the Bare Polarization Function for Massive Carriers

D.1 Derivation of the Time Ordered Green's Function

The field operators are given in terms of the wavefunctions Eq. 2.3

$$\Psi_\sigma(\mathbf{r},t) = \sum_n \int \mathrm{d}q \phi_{n,q}(\mathbf{r}) e^{-it\epsilon_n^{\mathrm{Q}}} c_{\sigma,n,q}. \tag{D.1}$$

Here $c_{\sigma,n,q}$ is the annihilation operator of a particle with spin σ. We suppress spin to avoid clutter, the time ordered Green's function is given as

$$\begin{aligned}\mathcal{G}^{(0)}(\mathbf{r},\mathbf{r}',t) &= -i\langle \mathcal{T}\Psi(\mathbf{r},t)\otimes\Psi^\dagger(\mathbf{r}',0)\rangle \\ &= -i\Theta(t)\sum_{n',n}\int \mathrm{d}q \int \mathrm{d}q' \phi_{n,q}(\mathbf{r})\phi^*_{n',q'}(\mathbf{r}') e^{-it\epsilon_n^{\mathrm{Q}}} \langle c_{n,q} c^\dagger_{n',q'}\rangle \\ &\quad +i\Theta(-t)\sum_{n',n}\int \mathrm{d}q \int \mathrm{d}q' \phi_{n,q}(\mathbf{r})\phi^*_{n',q'}(\mathbf{r}') e^{-it\epsilon_n^{\mathrm{Q}}} \langle c^\dagger_{n',q'} c_{n,q}\rangle,\end{aligned} \tag{D.2}$$

where $\otimes$ denotes the outer product, $\mathcal{T}$ is the time ordering operator, see [43]. Due to simple scalar form of the wave function, $\mathcal{G}^{(0)}$ is also a scalar function. Using that $\langle c_{n,q} c^\dagger_{n',q'}\rangle = \delta_{n,n'}\delta(q-q')\Theta(\epsilon_n^{\mathrm{Q}} - \epsilon_F)$ and $\langle c^\dagger_{n',q'} c_{n,q}\rangle = \delta_{n,n'}\delta(q-q')(1-\Theta(\epsilon_n^{\mathrm{Q}} - \epsilon_F))$

with ϵ_F Fermi energy,

$$\mathcal{G}^{(0)}(\mathbf{r},\mathbf{r}',t) = -i\sum_n \int \mathrm{d}q \phi_{n,q}(\mathbf{r})\phi^*_{n,q}(\mathbf{r}')e^{-it\epsilon_n^{\mathrm{Q}}}\left[\Theta(t)\Theta(\epsilon_n^{\mathrm{Q}}-\epsilon_F)-\Theta(-t)(1-\Theta(\epsilon_n^{\mathrm{Q}}-\epsilon_F))\right].$$

Then using the definition $\Theta(t) = -\frac{1}{2\pi i}\int \mathrm{d}E e^{-iEt}/(E+i\delta)$ and making the possible simplifications

$$\begin{aligned}\mathcal{G}^{(0)}(\mathbf{r},\mathbf{r}',t) &= \frac{1}{2\pi}\sum_n \int \mathrm{d}q \int \mathrm{d}E \phi_{n,q}(\mathbf{r})\phi^*_{n,q}(\mathbf{r}')e^{-it(\epsilon_n^{\mathrm{Q}}+E)}\left[\frac{\Theta(\epsilon_n^{\mathrm{Q}}-\epsilon_F)}{E+i\delta}+\frac{1-\Theta(\epsilon_n^{\mathrm{Q}}-\epsilon_F)}{E-i\delta}\right]\\ &= \frac{1}{2\pi}\sum_n \int \mathrm{d}q \int \mathrm{d}E \phi_{n,q}(\mathbf{r})\phi^*_{n,q}(\mathbf{r}')e^{-it(\epsilon_n^{\mathrm{Q}}+E)}\frac{1}{E+i\delta\mathrm{sgn}(\epsilon_n^{\mathrm{Q}}-\epsilon_F)}.\end{aligned}$$

In the last equation we have explicitly evaluated the Heaviside functions. Introducing a new variable $E' = E+\epsilon_n^{\mathrm{Q}}$ and omitting the prime in the next step we can easily reorganize the equation. We get

$$\mathcal{G}^{(0)}(\mathbf{r},\mathbf{r}',t) = \frac{1}{2\pi}\int \mathrm{d}E e^{-itE}\sum_n \int \mathrm{d}q \frac{\phi_{n,q}(\mathbf{r})\phi^*_{n,q}(\mathbf{r}')}{E-\epsilon_n^{\mathrm{Q}}+i\delta\mathrm{sgn}(\epsilon_n^{\mathrm{Q}}-\epsilon_F)}. \tag{D.3}$$

Here we recognize the Fourier transformed $\mathcal{G}^{(0)}(\mathbf{r},\mathbf{r}',E)$. In the following it is convenient to use this form of the Green's function, in which we introduce the center of mass and relative coordinates as $\mathbf{R} = (\mathbf{r}+\mathbf{r}')/2$ and $\Delta\mathbf{r} = \mathbf{r}-\mathbf{r}'$. Then

$$\mathcal{G}^{(0)}(\mathbf{R},\Delta\mathbf{r},E) = \sum_n \int \mathrm{d}q \frac{\phi_{n,q}(\mathbf{R}+\frac{\Delta\mathbf{r}}{2})\phi^*_{n,q}(\mathbf{R}-\frac{\Delta\mathbf{r}}{2})}{E-\epsilon_n^{\mathrm{Q}}+i\delta\mathrm{sgn}(\epsilon_n^{\mathrm{Q}}-\epsilon_F)}. \tag{D.4}$$

After a Fourier transform according to $\Delta\mathbf{r}$ we arrive at

$$\mathcal{G}^{(0)}(\mathbf{R},\mathbf{p},E) = \sum_n \int \mathrm{d}q \int \mathrm{d}\Delta\mathbf{r} e^{i\mathbf{p}\Delta\mathbf{r}}\frac{\phi_{n,q}(\mathbf{R}+\frac{\Delta\mathbf{r}}{2})\phi^*_{n,q}(\mathbf{R}-\frac{\Delta\mathbf{r}}{2})}{E-\epsilon_n^{\mathrm{Q}}+i\delta\mathrm{sgn}(\epsilon_n^{\mathrm{Q}}-\epsilon_F)}. \tag{D.5}$$

D.2 Bare Polarization Function for 2DEG

In terms of the previously defined time-ordered Green's functions the time-ordered response function is

$$\chi^{\mathrm{T}}(\mathbf{k},\omega) = -i\mathfrak{T}\mathfrak{r}\int\frac{\mathrm{d}E}{2\pi}\int\frac{\mathrm{d}\mathbf{p}}{(2\pi)^2}\mathcal{G}^{(0)}(\mathbf{R},\mathbf{p}-\frac{\mathbf{k}}{2},E)\mathcal{G}^{(0)}(\mathbf{R},\mathbf{p}+\frac{\mathbf{k}}{2},E+\omega) \tag{D.6}$$

$$\begin{aligned}
&= -i\int\frac{\mathrm{d}\mathbf{p}}{(2\pi)^2}\sum_{n,n'}\int\mathrm{d}q\int\mathrm{d}q'\int\mathrm{d}\Delta\mathbf{r}\int\mathrm{d}\Delta\mathbf{r}' e^{i(\mathbf{p}-\frac{\mathbf{k}}{2})\Delta\mathbf{r}}e^{i(\mathbf{p}+\frac{\mathbf{k}}{2})\Delta\mathbf{r}'}\times \\
&\quad\times\phi_{n,q}(\mathbf{R}+\frac{\Delta\mathbf{r}}{2})\phi^*_{n,q}(\mathbf{R}-\frac{\Delta\mathbf{r}}{2})\phi_{n',q'}(\mathbf{R}+\frac{\Delta\mathbf{r}'}{2})\phi^*_{n',q'}(\mathbf{R}-\frac{\Delta\mathbf{r}'}{2})\times \qquad \text{(D.7)}\\
&\quad\times\int\frac{\mathrm{d}E}{2\pi}\frac{1}{E-\epsilon_n^{\mathrm{Q}}+i\delta\mathrm{sgn}(\epsilon_n^{\mathrm{Q}}-\epsilon_F)}\cdot\frac{1}{E+\omega-\epsilon_{n'}^{\mathrm{Q}}+i\delta\mathrm{sgn}(\epsilon_{n'}^{\mathrm{Q}}-\epsilon_F)}.
\end{aligned}$$

First, we evaluate the intergral with respect to E. We use the residue theorem after extending the integral to the complex plane and by closing the contour in the upper half plane anticlockwise. We recognize that the integrand has simple poles at $E_1 = \epsilon_n^{\mathrm{Q}} - i\delta\mathrm{sgn}(\epsilon_n^{\mathrm{Q}}-\epsilon_F)$ and $E_2 = -\omega+\epsilon_{n'}^{\mathrm{Q}} - i\delta\mathrm{sgn}(\epsilon_{n'}^{\mathrm{Q}}-\epsilon_F)$. Notice that the poles are either in the upper or the lower half plane depending on the value of the Landau level energy with respect to the Fermi energy. Then

$$\begin{aligned}
\int_E &\equiv \int\mathrm{d}E\frac{1}{E-\epsilon_n^{\mathrm{Q}}+i\delta\mathrm{sgn}(\epsilon_n^{\mathrm{Q}}-\epsilon_F)}\cdot\frac{1}{E+\omega-\epsilon_{n'}^{\mathrm{Q}}+i\delta\mathrm{sgn}(\epsilon_{n'}^{\mathrm{Q}}-\epsilon_F)} \\
&= 2\pi i\left[\frac{1-\Theta(\epsilon_n^{\mathrm{Q}}-\epsilon_F)}{\epsilon_n^{\mathrm{Q}}-\epsilon_{n'}^{\mathrm{Q}}+\omega+i\delta(1+\mathrm{sgn}(\epsilon_{n'}^{\mathrm{Q}}-\epsilon_F))}+\frac{1-\Theta(\epsilon_{n'}^{\mathrm{Q}}-\epsilon_F)}{-\omega-\epsilon_n^{\mathrm{Q}}+\epsilon_{n'}^{\mathrm{Q}}+i\delta(1+\mathrm{sgn}(\epsilon_n^{\mathrm{Q}}-\epsilon_F))}\right] \\
&= 2\pi i\left[\frac{(1-\Theta(\epsilon_n^{\mathrm{Q}}-\epsilon_F))\Theta(\epsilon_{n'}^{\mathrm{Q}}-\epsilon_F)}{\epsilon_n^{\mathrm{Q}}-\epsilon_{n'}^{\mathrm{Q}}+\omega+i2\delta}+\frac{(1-\Theta(\epsilon_{n'}^{\mathrm{Q}}-\epsilon_F))\Theta(\epsilon_n^{\mathrm{Q}}-\epsilon_F)}{-\omega-\epsilon_n^{\mathrm{Q}}+\epsilon_{n'}^{\mathrm{Q}}+i2\delta}\right].
\end{aligned}$$

We have got this expression by rewriting the signums in the denominator of the first line in terms of Heaviside functions. After some algebra, one can recover the last line. To proceed, we apply the the Sokhotski - Plemelj theorem:

$$\lim_{\delta\to 0^+}\frac{1}{x\pm i\delta} = \mathcal{P}\frac{1}{x}\mp i\pi\delta(x) \tag{D.8}$$

Here $\mathcal{P}$ denotes the Cauchy principal value. With these

$$\begin{aligned}
\int_E &= 2\pi i \left[\mathcal{P}\frac{(1-\Theta(\epsilon_n^{\mathrm{Q}}-\epsilon_F))\Theta(\epsilon_{n'}^{\mathrm{Q}}-\epsilon_F)}{\epsilon_n^{\mathrm{Q}}-\epsilon_{n'}^{\mathrm{Q}}+\omega} - i\pi\delta(\epsilon_n^{\mathrm{Q}}-\epsilon_{n'}^{\mathrm{Q}}+\omega)(1-\Theta(\epsilon_n^{\mathrm{Q}}-\epsilon_F))\Theta(\epsilon_{n'}^{\mathrm{Q}}-\epsilon_F) \right. \\
&\quad \left. + \mathcal{P}\frac{(1-\Theta(\epsilon_{n'}^{\mathrm{Q}}-\epsilon_F))\Theta(\epsilon_n^{\mathrm{Q}}-\epsilon_F)}{-\omega-\epsilon_n^{\mathrm{Q}}+\epsilon_{n'}^{\mathrm{Q}}} - i\pi\delta(-\omega-\epsilon_n^{\mathrm{Q}}+\epsilon_{n'}^{\mathrm{Q}})(1-\Theta(\epsilon_{n'}^{\mathrm{Q}}-\epsilon_F))\Theta(\epsilon_n^{\mathrm{Q}}-\epsilon_F) \right] \\
&= 2\pi i \left[\mathcal{P}\frac{1}{\epsilon_n^{\mathrm{Q}}-\epsilon_{n'}^{\mathrm{Q}}+\omega}(\Theta(\epsilon_{n'}^{\mathrm{Q}}-\epsilon_F)-\Theta(\epsilon_n^{\mathrm{Q}}-\epsilon_F)) \right. \\
&\quad \left. -i\pi\delta(\epsilon_n^{\mathrm{Q}}-\epsilon_{n'}^{\mathrm{Q}}+\omega)(\Theta(\epsilon_{n'}^{\mathrm{Q}}-\epsilon_F)+\Theta(\epsilon_n^{\mathrm{Q}}-\epsilon_F)-2\Theta(\epsilon_{n'}^{\mathrm{Q}}-\epsilon_F)\Theta(\epsilon_n^{\mathrm{Q}}-\epsilon_F)) \right] \\
&= 2\pi i(\Theta(\epsilon_{n'}^{\mathrm{Q}}-\epsilon_F)-\Theta(\epsilon_n^{\mathrm{Q}}-\epsilon_F)) \left[\mathcal{P}\frac{1}{\epsilon_n^{\mathrm{Q}}-\epsilon_{n'}^{\mathrm{Q}}+\omega} - i\pi\delta(\epsilon_n^{\mathrm{Q}}-\epsilon_{n'}^{\mathrm{Q}}+\omega)\mathrm{sgn}(\omega) \right] \\
&= 2\pi i \frac{\Theta(\epsilon_{n'}^{\mathrm{Q}}-\epsilon_F)-\Theta(\epsilon_n^{\mathrm{Q}}-\epsilon_F)}{\epsilon_n^{\mathrm{Q}}-\epsilon_{n'}^{\mathrm{Q}}+\omega+i\delta\mathrm{sgn}(\omega)}.
\end{aligned}$$

We have arrived at the final expression for the integral. We implement this result in χ^{T}, we regroup the elements, and use the fact that $\Delta\mathbf{r} = -\Delta\mathbf{r}'$. Then we arrive at

$$\chi^{\mathrm{T}}(\mathbf{k},\omega) = \int \frac{\mathrm{d}\mathbf{p}}{(2\pi)^2} \sum_{n,n'} \int \mathrm{d}q \int \mathrm{d}q' \frac{\Theta(\epsilon_{n'}^{\mathrm{Q}}-\epsilon_F)-\Theta(\epsilon_n^{\mathrm{Q}}-\epsilon_F)}{\omega+\epsilon_n^{\mathrm{Q}}-\epsilon_{n'}^{\mathrm{Q}}+i\delta\mathrm{sgn}(\omega)} \times \tag{D.9a}$$

$$\times \int \mathrm{d}\Delta\mathbf{r}\phi_{n',q'}^*(\mathbf{R}+\frac{\Delta\mathbf{r}}{2})e^{i(\mathbf{p}-\frac{\mathbf{k}}{2})\Delta\mathbf{r}}\phi_{n,q}(\mathbf{R}+\frac{\Delta\mathbf{r}}{2}) \times \tag{D.9b}$$

$$\times \int \mathrm{d}\Delta\mathbf{r}'\phi_{n,q}^*(\mathbf{R}+\frac{\Delta\mathbf{r}'}{2})e^{i(\mathbf{p}+\frac{\mathbf{k}}{2})\Delta\mathbf{r}'}\phi_{n',q'}(\mathbf{R}+\frac{\Delta\mathbf{r}'}{2}). \tag{D.9c}$$

The first integral can be executed after the appropriate change of variables: $\mathbf{z} = \mathbf{R}+\frac{\Delta\mathbf{r}}{2}$. Now we are in the position to apply Eq. E.4. Then

$$\begin{aligned}
&\int \mathrm{d}\Delta\mathbf{r}\phi_{n',q'}^*(\mathbf{R}+\frac{\Delta\mathbf{r}}{2})e^{i(\mathbf{p}-\frac{\mathbf{k}}{2})\Delta\mathbf{r}}\phi_{n,q}(\mathbf{R}+\frac{\Delta\mathbf{r}}{2}) \\
&\qquad = 4e^{-i(2\mathbf{p}-\mathbf{k})\mathbf{R}}\delta(q-q'+2p_y-k_y)F_{n',n}(-2\mathbf{p}+\mathbf{k})e^{-i(-2p_x+k_x)\ell^2\frac{q+q'}{2}}.
\end{aligned}$$

Similarly with the second integral:

$$\begin{aligned}
&\int \mathrm{d}\Delta\mathbf{r}'\phi_{n,q}^*(\mathbf{R}+\frac{\Delta\mathbf{r}'}{2})e^{i(\mathbf{p}+\frac{\mathbf{k}}{2})\Delta\mathbf{r}'}\phi_{n',q'}(\mathbf{R}+\frac{\Delta\mathbf{r}'}{2}) \\
&\qquad = 4e^{-i(2\mathbf{p}+\mathbf{k})\mathbf{R}}\delta(q'-q+2p_y+k_y)F_{n,n'}(-2\mathbf{p}-\mathbf{k})e^{i(2p_x+k_x)\ell^2\frac{q+q'}{2}}.
\end{aligned}$$

The time-ordered response function becomes:

$$\begin{aligned}\chi^{\mathrm{T}}(\mathbf{k},\omega) &= 16\int\frac{\mathrm{d}\mathbf{p}}{(2\pi)^2}\sum_{n,n'}\int\mathrm{d}q\int\mathrm{d}q'\frac{\Theta(\epsilon^{\mathrm{Q}}_{n'}-\epsilon_F)-\Theta(\epsilon^{\mathrm{Q}}_{n}-\epsilon_F)}{\omega+\epsilon^{\mathrm{Q}}_{n}-\epsilon^{\mathrm{Q}}_{n'}+i\delta\mathrm{sgn}(\omega)}F_{n',n}(-2\mathbf{p}+\mathbf{k})\times\\ &\times F_{n,n'}(-2\mathbf{p}-\mathbf{k})\delta(q-q'+2p_y-k_y)\delta(q'-q+2p_y+k_y)e^{i4p_x\ell^2\frac{q+q'}{2}}e^{-i4\mathbf{pR}}\\ &= 4\int\frac{\mathrm{d}\mathbf{p}}{(2\pi)^2}\sum_{n,n'}\int\mathrm{d}\Delta q\int\mathrm{d}Q\frac{\Theta(\epsilon^{\mathrm{Q}}_{n'}-\epsilon_F)-\Theta(\epsilon^{\mathrm{Q}}_{n}-\epsilon_F)}{\omega+\epsilon^{\mathrm{Q}}_{n}-\epsilon^{\mathrm{Q}}_{n'}+i\delta\mathrm{sgn}(\omega)}F_{n',n}(-2\mathbf{p}+\mathbf{k})\times\\ &\times F_{n,n'}(-2\mathbf{p}-\mathbf{k})\delta(\frac{\Delta q}{2}+p_y-\frac{k_y}{2})\delta(-\frac{\Delta q}{2}+p_y+\frac{k_y}{2})e^{i4p_x\ell^2Q}e^{-i4\mathbf{pR}}.\end{aligned}$$

Here we have applied the identity $\delta(ax)=\frac{1}{|a|}\delta(x)$, and in the last line we have introduced "centre of mass" coordinates: $\frac{q+q'}{2}=Q$ and $q-q'=\Delta q$. One can evaluate the integral with respect to Q, leading to $p_x=0$, while the rearrangement and the evaluation of the delta functions combined with the integral with respect to Δq leads to $p_y=0$. By denoting the highest filled Landau level n^F_Q

$$\begin{aligned}\chi^{\mathrm{T}}(\mathbf{k},\omega) &= \frac{1}{2\pi\ell^2}\sum_{n,n'}\frac{\Theta(\epsilon^{\mathrm{Q}}_{n'}-\epsilon_F)-\Theta(\epsilon^{\mathrm{Q}}_{n}-\epsilon_F)}{\omega+\epsilon^{\mathrm{Q}}_{n}-\epsilon^{\mathrm{Q}}_{n'}+i\delta\mathrm{sgn}(\omega)}F_{n',n}(\mathbf{k})F_{n,n'}(-\mathbf{k})\\ &= \frac{1}{2\pi\ell^2}\sum_{n,n'}\frac{\Theta(\epsilon^{\mathrm{Q}}_{n'}-\epsilon_F)-\Theta(\epsilon^{\mathrm{Q}}_{n}-\epsilon_F)}{\omega+\epsilon^{\mathrm{Q}}_{n}-\epsilon^{\mathrm{Q}}_{n'}+i\delta\mathrm{sgn}(\omega)}|F_{n',n}(\mathbf{k})|^2\\ &= \frac{1}{2\pi\ell^2}\sum_{n\le n^F_Q}\sum_{n'>n^F_Q}\frac{|F_{n',n}(\mathbf{k})|^2}{\omega+\epsilon^{\mathrm{Q}}_{n}-\epsilon^{\mathrm{Q}}_{n'}+i\delta\mathrm{sgn}(\omega)}-\sum_{n'\le n^F_Q}\sum_{n>n^F_Q}\frac{|F_{n',n}(\mathbf{k})|^2}{\omega+\epsilon^{\mathrm{Q}}_{n}-\epsilon^{\mathrm{Q}}_{n'}+i\delta\mathrm{sgn}(\omega)}.\end{aligned}$$

With the application of Eq. D.8 one eliminates the signum, finally we get:

$$\begin{aligned}\chi^{\mathrm{T}}(\mathbf{k},\omega) &= \frac{1}{2\pi\ell^2}\sum_{n\le n^F_Q}\sum_{n'>n^F_Q}\frac{|F_{n',n}(\mathbf{k})|^2}{\omega+\epsilon^{\mathrm{Q}}_{n}-\epsilon^{\mathrm{Q}}_{n'}+i\delta}-\sum_{n'\le n^F_Q}\sum_{n>n^F_Q}\frac{|F_{n',n}(\mathbf{k})|^2}{\omega+\epsilon^{\mathrm{Q}}_{n}-\epsilon^{\mathrm{Q}}_{n'}-i\delta}\\ &= \frac{1}{2\pi\ell^2}\sum_{n'\le n^F_Q}\sum_{n>n^F_Q}(\frac{|F_{n,n'}(\mathbf{k})|^2}{\omega-\epsilon^{\mathrm{Q}}_{n}+\epsilon^{\mathrm{Q}}_{n'}+i\delta}+\frac{|F_{n',n}(\mathbf{k})|^2}{-\omega-\epsilon^{\mathrm{Q}}_{n}+\epsilon^{\mathrm{Q}}_{n'}+i\delta}).\end{aligned}\tag{D.10}$$

To get the retarded response function we shall use the identities of Eq. 4.4, which amounts to the replacement of $i\delta$ to $-i\delta$ in the second term.

$$\chi^{(0)}_Q(\mathbf{k},\omega)=\frac{1}{2\pi\ell^2}\sum_{n'\le n^F_Q}\sum_{n>n^F_Q}(\frac{|F_{n,n'}(\mathbf{k})|^2}{\omega-\epsilon^{\mathrm{Q}}_{n}+\epsilon^{\mathrm{Q}}_{n'}+i\delta}+\frac{|F_{n',n}(\mathbf{k})|^2}{-\omega-\epsilon^{\mathrm{Q}}_{n}+\epsilon^{\mathrm{Q}}_{n'}-i\delta})\tag{D.11}$$

Appendix E

The Computation of Form Factors

E.1 Form Factor for 2DEG

We use here the definition of the Landau level wavefunctions given in Eq. 2.3 and $\mathbf{q} = (q_x, q_y)$. Then the integral to be evaluated is

$$\int \mathrm{d}\mathbf{r}\ \phi^*_{n',k'}(\mathbf{r}) e^{-i\mathbf{q}\cdot\mathbf{r}} \phi_{n,k}(\mathbf{r}) = \frac{1}{2\pi\ell\sqrt{\pi 2^{n+n'} n'! n!}} \int \mathrm{d}x e^{i(-q_x - k' + k)x} \times \\ \times \int \mathrm{d}y e^{-iq_y y} e^{-\frac{(y-k\ell^2)^2 + (y-k'\ell^2)^2}{2\ell^2}} H_n(\frac{y}{\ell} - k\ell) H_{n'}(\frac{y}{\ell} - k'\ell). \quad \text{(E.1)}$$

One can evaluate the integral with respect to x leading to a Dirac delta function, whereas the integral with respect to y can be simplified by introducing a new variable $y' = y - \frac{k+k'}{2}\ell^2$, and making use of the Dirac delta function. Then the expression becomes:

$$\int \mathrm{d}\mathbf{r}\ \phi^*_{n',k'}(\mathbf{r}) e^{-i\mathbf{q}\cdot\mathbf{r}} \phi_{n,k}(\mathbf{r}) = \\ \frac{\delta(-q_x - k' + k)}{2^{\frac{n+n'}{2}} \ell\sqrt{\pi n'! n!}} e^{-iq_y \frac{k+k'}{2}\ell^2} e^{-\frac{q_x^2 \ell^2}{4}} \int \mathrm{d}y' e^{-iq_y y' - \frac{y'^2}{\ell^2}} H_n(\frac{y'}{\ell} - \frac{q_x \ell}{2}) H_{n'}(\frac{y'}{\ell} + \frac{q_x \ell}{2}).$$

With the view to apply identity Eq. C.1 we introduce another new variable: $y'' = \frac{y'}{\ell} + \frac{iq_y\ell}{2}$, and we omit the tildes, then the integral becomes:

$$\frac{\delta(-q_x-k'+k)}{2^{\frac{n+n'}{2}}\sqrt{\pi n'!n!}}e^{-iq_y\frac{k+k'}{2}\ell^2-\frac{q_x^2\ell^2}{4}}\int \mathrm{d}y e^{-y^2-\frac{q_y^2\ell^2}{4}}H_n(y-\frac{iq_y\ell}{2}-\frac{q_x\ell}{2})H_{n'}(y-\frac{iq_y\ell}{2}+\frac{q_x\ell}{2})$$
$$= \begin{cases} \delta(-q_x-k'+k)2^{\frac{n'-n}{2}}\sqrt{\frac{n!}{n'!}}(\frac{q_x-iq_y}{2}\ell)^{n'-n}L_n^{n'-n}(\frac{|q|^2\ell^2}{2})e^{-iq_y\frac{k+k'}{2}\ell^2-\frac{|q|^2\ell^2}{4}} & n'\geq n, \\ \delta(-q_x-k'+k)2^{\frac{n-n'}{2}}\sqrt{\frac{n'!}{n!}}(\frac{-q_x-iq_y}{2}\ell)^{n-n'}L_{n'}^{n-n'}(\frac{|q|^2\ell^2}{2})e^{-iq_y\frac{k+k'}{2}\ell^2-\frac{|q|^2\ell^2}{4}} & n'<n. \end{cases}$$

We define the form factor $F_{n',n}$ with the following properties: if $n'\geq n$

$$F_{n',n}(\mathbf{q}) = \sqrt{\frac{n!}{n'!}}(\frac{q_x-iq_y}{\sqrt{2}}\ell)^{n'-n}L_n^{n'-n}(\frac{|q|^2\ell^2}{2})e^{-\frac{|q|^2\ell^2}{4}} \tag{E.2}$$

and if $n'<n$

$$F_{n,n'}(\mathbf{q}) = F^*_{n',n}(-\mathbf{q}) \tag{E.3}$$

With this notation the original integral may be given in a compact form:

$$\int \mathrm{d}\mathbf{r}\ \phi^*_{n',k'}(\mathbf{r})e^{-i\mathbf{q}\cdot\mathbf{r}}\phi_{n,k}(\mathbf{r}) = \delta(-q_x-k'+k)F_{n',n}(\mathbf{q})e^{-iq_y\frac{k+k'}{2}\ell^2}. \tag{E.4}$$

E.2 Form Factor for the Weyl System

Here we sketch the main steps of the derivation of the form factor for the Weyl materials in Eq. E.8, which is an important ingredient of the calculation of time-ordered response function $\chi^{\mathrm{T}}_{\xi}(\tilde{\mathbf{k}},\omega)$ in Eq. 4.18.

We start with the harmonic oscillator wave function of Eq. B.5 with the argument given in Eq B.6. One shall evaluate the following integral

$$\int_{\mathbf{r}} \equiv \int \mathrm{d}\mathbf{r}[\phi^{\xi}_{n',k'}(\mathbf{r})]^* e^{-i\mathbf{q}\cdot\mathbf{r}}\phi^{\xi}_{n,k}(\mathbf{r}) \tag{E.5}$$
$$= \int \mathrm{d}\mathbf{r}\frac{e^{-i(k'-k)x}}{2\pi\alpha\ell}\frac{\lambda^{1/2}}{(2^{|n'|+|n|}|n'|!|n|!\pi)^{1/2}}e^{-(\mathrm{Y}^2_{n',\xi}+\mathrm{Y}^2_{n,\xi})/2}e^{-i\mathbf{q}\cdot\mathbf{r}}H_{|n'|}(\mathrm{Y}_{n',\xi})H_{|n|}(\mathrm{Y}_{n,\xi}).$$

For simplicity we introduce new variables: $y' = y\sqrt{\lambda}/\alpha\ell$ and also $k_3 = \sqrt{\lambda}\alpha\ell k +$

$\xi\beta\sqrt{2|n|}\mathrm{sgn}(n)$ along with $k_4 = \sqrt{\lambda}\alpha\ell k' + \xi\beta\sqrt{2|n'|}\mathrm{sgn}(n')$. Then

$$\int_{\mathbf{r}} = \frac{1}{2\pi}\frac{1}{(2^{|n'|+|n|}|n'|!|n|!\pi)^{1/2}}\int \mathrm{d}x \int \mathrm{d}y' e^{-(y'-k_3)^2/2} e^{-(y'-k_4)^2/2} e^{-i(q_x x + q_y \ell\alpha y'/\sqrt{\lambda})} \times$$
$$\times\, e^{-ix(k_4-k_3)/\sqrt{\lambda}\ell\alpha} e^{-ix\xi\beta(\sqrt{2|n|}\mathrm{sgn}(n)-\sqrt{2|n'|}\mathrm{sgn}(n'))/\sqrt{\lambda}\ell\alpha} H_{|n'|}(y'-k_4)H_{|n|}(y'-k_3).$$

For simplicity we omit the prime in the following. We are in the position to execute the intergral with respect to x, leading to

$$\int \mathrm{d}x e^{-ix(k_4-k_3)/\sqrt{\lambda}\ell\alpha} e^{-ix\xi\beta(\sqrt{2|n|}\mathrm{sgn}(n)-\sqrt{2|n'|}\mathrm{sgn}(n'))/\sqrt{\lambda}\ell\alpha} e^{-iq_x x}$$
$$= 2\pi\delta\left((k_4 - k_3 - \xi\beta\mathrm{sgn}(n')\sqrt{2|n'|} + \xi\beta\mathrm{sgn}(n)\sqrt{2|n|}\ )/\sqrt{\lambda}\ell\alpha + q_x\right). \quad \text{(E.6)}$$

We aim to apply the indentity of Eq. C.1, therefore we introduce a new variable $y' = y - (k_4+k_3)/2 + i\ell\alpha q_y/2\sqrt{\lambda}$, and we omit the prime at the same time. With these changes and some algebra we arrive at a final form of the integral with respect to y:

$$\int \mathrm{d}y e^{-y^2} H_{|n'|}(y - iP + Q_{n',n,\xi}) H_{|n|}(y - iP - Q_{n',n,\xi})$$
$$= \begin{cases} 2^{|n'|}\sqrt{\pi}|n|!(-iP + Q_{n',n,\xi})^{|n'|-|n|} L_{|n|}^{|n'|-|n|}(2(Q_{n',n,\xi}^2 + P^2)) & |n'| \geq |n|, \\ 2^{|n|}\sqrt{\pi}|n'|!(-iP - Q_{n',n,\xi})^{|n|-|n'|} L_{|n'|}^{|n|-|n'|}(2(Q_{n',n,\xi}^2 + P^2)) & |n'| < |n|. \end{cases}$$

We used the shorthand notations in the above definitions

$$Q_{n',n,\xi} = \frac{q_x\sqrt{\lambda}\alpha\ell - \xi\beta\sqrt{2|n'|}\mathrm{sgn}(n') + \xi\beta\sqrt{2|n|}\mathrm{sgn}(n)}{2}, \quad \text{and} \quad P = \frac{\alpha\ell}{2\sqrt{\lambda}}q_y \quad \text{(E.7)}$$

The form factor for $|n'| \geq |n|$ are defined as

$$F_{|n'|,|n|}^{n',n,\xi}(\mathbf{q}) = \sqrt{\frac{|n|!}{|n'|!}}\sqrt{2}^{|n'|-|n|}\ (-iP + Q_{n',n,\xi})^{|n'|-|n|} L_{|n|}^{|n'|-|n|}(2(Q_{n',n,\xi}^2 + P^2)) e^{-(Q_{n',n,\xi}^2+P^2)}. \quad \text{(E.8)}$$

Similarly, for $|n| > |n'|$ the definition is

$$F_{|n'|,|n|}^{n',n,\xi}(\mathbf{q}) = \sqrt{\frac{|n'|!}{|n|!}}\sqrt{2}^{|n|-|n'|}\ (-iP - Q_{n',n,\xi})^{|n|-|n'|}\ L_{|n'|}^{|n|-|n'|}\left(2(Q_{n',n,\xi}^2 + P^2)\right) e^{-(Q_{n',n,\xi}^2+P^2)}. \quad \text{(E.9)}$$

The final result for the integral in Eq. E.5 is

$$\int \mathrm{d}\mathbf{r}[\phi^{\xi}_{n',k'}(\mathbf{r})]^* e^{-i\mathbf{q}\cdot\mathbf{r}}\phi^{\xi}_{n,k}(\mathbf{r}) = \\ \delta\left(k' - k + q_x\right) F^{n',n,\xi}_{|n'|,|n|}(\mathbf{q}) e^{-iq_y\ell\alpha\xi\beta(\mathrm{sgn}(n')\sqrt{2|n'|}+\mathrm{sgn}(n)\sqrt{2|n|})/2\sqrt{\lambda}} e^{-iq_y\ell^2\alpha^2(k'+k)/2}.$$

Bibliography

[1] D. S. L. Abergel, A. Russell, and V. I. Falko, Appl. Phys. Lett. **91**, 063125 (2007).

[2] D. S. L. Abergel and V. I. Falko, Phys. Rev. B **75**, 155430 (2007).

[3] P. Alemany, J. P. Pouget, and E. Canadell, Phys. Rev. B **85**, 195118 (2012).

[4] T. Ando, A. B. Fowler, and F. Stern, Rev. Mod. Phys. **54**, 437 (1982).

[5] T. Ando, J. Phys. Soc. Jpn. **75**, 074716 (2006).

[6] M. Assili, S. Haddad, and W. Kang, Phys. Rev. B **91**, 115422 (2015).

[7] S. Bae, H. K. Kim, Y. Lee, X. Xu, J.-S. Park, Y. Zheng, J. Balakrishnan, D. Im, T. Lei, Y. Il Song, Y. J. Kim, K. S. Kim, B. Özyilmaz, J.-H. Ahn, B. H. Hong, and S. Iijima, Nat. Nanotechnol. **5**, 574 (2010).

[8] W. Bao, Z. Zhao, H. Zhang, G. Liu, P. Kratz, L. Jing, J. Velasco, Jr., D. Smirnov, and C. N. Lau, Phys. Rev. Lett. **105**, 246601 (2010).

[9] Y. Barlas, R. Côté, K. Nomura, and A. H. MacDonald, Phys. Rev. Lett. **101**, 097601 (2008).

[10] Y. Barlas, R. Côté, J. Lambert, and A. H. MacDonald, Phys. Rev. Lett. **104** 096802 (2010).

[11] Y. Barlas, W.-Ch. Lee, K. Nomura, and A. H. MacDonald, Int. J. Mod. Phys. B **23**, 2634 (2009).

[12] D. N. Basov, M. M. Fogler, A. Lanzara, F. Wang, and Y. Zhang, Rev. Mod. Phys. **86**, 959 (2014).

[13] C. Bena and G. Montambaux, New J. Phys. **11**, 095003 (2009).

[14] K. Bender, I. Hennig, D. Schweitzer, K. Dietz, H. Endres, and H. J. Keller, Mol. Cryst. Liq. Cryst. **108**, 359 (1984).

[15] J. D. Bernal, Proc. Roy. Soc. A **106**, 749 (1924).

[16] V. E. Bisti and N. N. Kirova, Phys. Rev. B **84**, 155434 (2011).

[17] P. Blake, E. W. Hill, A. H. Castro Neto, K. S. Novoselov, D. Jiang, R. Yang, T. J. Booth, and A. K. Geim, Appl. Phys. Lett. **91**, 063124 (2007).

[18] D. Bohm and D. Pines, Phys. Rev. **82**, 625 (1951).

[19] D. Pines and D. Bohm, Phys. Rev. **85**, 338 (1952).

[20] D. Bohm and D. Pines, Phys. Rev. **92**, 609 (1953).

[21] L. G. Booshehri, C. H. Mielke, D. G. Rickel, S. A. Crooker, Q. Zhang, L. Ren, E. H. Hároz, A. Rustagi, C. J. Stanton, Z. Jin, Z. Sun, Z. Yan, J. M. Tour, and J. Kono, Phys. Rev. B **85**, 205407 (2012).

[22] A. Bostwick, T. Ohta, T. Seyller, K. Horn, and E. Rotenberg, Nat. Phys. **3**, 36 (2007).

[23] Yu. A. Bychkov, S. V. Iordanskii, and G. M. Eliashberg, Pis'ma Zh. Eksp. Teor. Fiz. **33**, 152 (1981) [Sov. Phys. JETP Lett. **33**, 143 (1981)].

[24] Yu. A. Bychkov and E. I. Rashba, Zh. Eksp. Teor. Fiz. **85**, 1826 (1980) [Sov. Phys. JETP **58**, 1062 (1983)].

[25] Yu. A. Bychkov and G. Martinez, Phys. Rev. B **77**, 125417 (2008).

[26] E. V. Castro, K. S. Novoselov, S. V. Morozov, N. M. R. Peres, J. M. B. Lopes dos Santos, J. Nilsson, F. Guinea, A. K. Geim, and A. H. Castro Neto, Phys. Rev. Lett. **99**, 216802 (2007).

[27] K. W. Chiu and J. J. Quinn, Phys. Rev. B **9**, 4724 (1974).

[28] D. B. Chklovskii, B. I. Shklovskii, and L. I. Glazman, Phys. Rev. B **46**, 4026 (1992).

[29] T. Choji, A. Kobayashi, and Y. Suzumura, J. Phys. Soc. Jpn. **80**, 074712 (2011).

[30] R. Côté, J. Lambert, Y. Barlas, and A. H. MacDonald, Phys. Rev. B **82**, 035445 (2010).

[31] J. Cserti and G. Dávid, Phys. Rev. B **74**, 172305 (2006).

[32] H. P. Dahal, Y. N. Joglekar, K. S. Bedell, and A. V. Balatsky, Phys. Rev. B **74**, 233405 (2006).

[33] S. Das Sarma, S. Adam, E. H. Hwang, and E. Rossi, Rev. Mod. Phys. **83**, 407 (2011).

[34] R. S. Deacon, K.-C. Chuang, R. J. Nicholas, K. S. Novoselov, and A. K. Geim, Phys. Rev. B **76**, 081406(R) (2007).

[35] H. Duan, N. Yan, R. Yu, C.-R. Chang, G. Zhou, H.-S. Hu, H. Rong, Z. Niu, J. Mao, H. Asakura, T. Tanaka, P. J. Dyson, J. Li, and Y. Li, Nat. Commun. **5**, 3093 (2014).

[36] H. J. van Elferen, A. Veligura, E. V. Kurganova, U. Zeitler, J. C. Maan, N. Tombros, I. J. Vera-Marun, and B. J. van Wees, Phys. Rev. B **85**, 115408 (2012).

[37] V. I. Fal'ko, Philos. Trans. R. Soc. A **366**, 205 (2008).

[38] G. Fasol, N. Mestres, H. P. Hughes, A. Fischer, and K. Ploog, Phys. Rev. Lett. **56**, 2517 (1986).

[39] C. Faugeras, M. Amado, P. Kossacki, M. Orlita, M. Kühne, A. A. L. Nicolet, Y. I. Latyshev, and M. Potemski, Phys. Rev. Lett. **107**, 036807 (2011).

[40] Z. Fei, A. S. Rodin, G. O. Andreev, W. Bao, A. S. McLeod, M. Wagner, L. M. Zhang, Z. Zhao, M. Thiemens, G. Dominguez, M. M. Fogler, A. H. Castro Neto, C. N. Lau, F. Keilmann, and D. N. Basov, Nature **487**, 82 (2012).

[41] B. E. Feldman, J. Martin, and A. Yacoby, Nat. Phys. **5**, 889 (2009).

[42] H. A. Fertig, L. Brey, R. Côté, A. H. MacDonald, A. Karlhede, and S. L. Sondhi, Phys. Rev. B **55**, 10671 (1997).

[43] A. L. Fetter and J. D. Walecka, *Quantum theory of many-particle systems* (McGraw-Hill Book Company, New York, 1971).

[44] S. Gangadharaiah, A. M. Farid, and E. G. Mishchenko, Phys. Rev. Lett. **100**, 166802 (2008).

[45] A. K. Geim and K. S. Novoselov, Nat. Mater. **6**, 183 (2007).

[46] G. F. Giuliani and G. Vignale, *Quantum Theory of the Electron Liquid* (Cambridge University Press, Cambridge, 2005).

[47] M. O. Goerbig, J.-N. Fuchs, G. Montambaux, and F. Piéchon, Phys. Rev. B **78**, 045415 (2008).

[48] M. O. Goerbig, Rev. Mod. Phys. **83**, 1193 (2011).

[49] E. V. Gorbar, V. P. Gusynin, and V. A. Miransky, Pis'ma Zh. Eksp. Teor. Fiz. **91**, 334 (2010) [JETP Lett. **91**, 314 (2010)].

[50] E. V. Gorbar, V. P. Gusynin, and V. A. Miransky, Phys. Rev. B **81**, 155451 (2010).

[51] E. V. Gorbar, V. P. Gusynin, V. A. Miransky, and I. A. Shovkovy, Phys. Rev. B **85**, 235460 (2012).

[52] I. S. Gradshteyn and I. M. Ryzhik, *Table of Integrals, Series, and Products*, edited by A. Jeffrey and D. Zwillinger (Elsevier/Academic Press, Amsterdam, 2007).

[53] W. Greiner, *Relativistic quantum mechanics: wave equations* (Springer, Berlin, 2000).

[54] F. Guinea, A. H. Castro Neto, and N. M. R. Peres, Phys. Rev. B **73**, 245426 (2006).

[55] M. Z. Hasan and C. L. Kane, Rev. Mod. Phys. **82**, 3045 (2010).

[56] E. A. Henriksen, Z. Jiang, L.-C. Tung, M. E. Schwartz, M. Takita, Y.-J. Wang, P. Kim, and H. L. Stormer, Phys. Rev. Lett. **100**, 087403 (2008).

[57] E. A. Henriksen, P. Cadden-Zimansky, Z. Jiang, Z. Q. Li, L.-C. Tung, M. E. Schwartz, M. Takita, Y.-J. Wang, P. Kim, and H. L. Stormer, Phys. Rev. Lett. **104**, 067404 (2010).

[58] E. A. Henriksen and J. P. Eisenstein, Phys. Rev. B **82**, 041412(R) (2010).

[59] T. Himura, T. Morinari, and T. Tohyama, J. Phys.: Condens. Matter **23**, 464202 (2011).

[60] E. H. Hwang and S. Das Sarma, Phys. Rev. B **75**, 205418 (2007).

[61] S. Ishibashi, T. Tamura, M. Kohyama, and K. Terakura, J. Phys. Soc. Jpn. **75**, 015005 (2006).

[62] A. Iyengar, J. Wang, H. A. Fertig, and L. Brey, Phys. Rev. B **75**, 125430 (2007).

[63] J. K. Jain and P. B. Allen, Phys. Rev. Lett. **54**, 2437 (1985).

[64] Z. Jiang, E. A. Henriksen, L. C. Tung, Y.-J. Wang, M. E. Schwartz, M. Y. Han, P. Kim, and H. L. Stormer, Phys. Rev. Lett. **98**, 197403 (2007).

[65] K. Kajita, T. Ojiro, H. Fujii, Y. Nishio, H. Kobayashi, A. Kobayashi, and R. Kato, J. Phys. Soc. Jpn. **61**, 23 (1992).

[66] C. Kallin and B. I. Halperin, Phys. Rev. B **30**, 5655 (1984).

[67] M. I. Katsnelson, K. S. Novoselov, and A. K. Geim, Nat. Phys. **2**, 620 (2006).

[68] M. I. Katsnelson, Eur. Phys. J. B **51**, 157 (2006).

[69] S. Katayama, A. Kobayashi, and Y. Suzumura, J. Phys. Soc. Jpn. **75**, 054705 (2006).

[70] S. Katayama, A. Kobayashi, and Y. Suzumura, J. Phys.: Conf. Series **132**, 012003 (2008).

[71] S. Katayama, A. Kobayashi, and Y. Suzumura, Eur. Phys. J. B **67**, 139 (2009).

[72] M. Kharitonov, Phys. Rev. Lett. **109**, 046803 (2012).

[73] S. Kim, K. Lee, and E. Tutuc, Phys. Rev. Lett. **107**, 016803 (2011).

[74] H. Kino and T. Miyazaki, J. Phys. Soc. Jpn. **75**, 034704 (2006).

[75] A. Kobayashi, S. Katayama, Y. Suzumura, and H. Fukuyama, J. Phys. Soc. Jpn. **76**, 034711 (2007).

[76] W. Kohn, Phys. Rev. **123**, 1242 (1961).

[77] R. Kondo, S. Kagoshima, N. Tajima, and R. Kato, J. Phys. Soc. Jpn. **78**, 114714 (2009).

[78] V. N. Kotov, B. Uchoa, V. M. Pereira, F. Guinea, and A. H. Castro Neto, Rev. Mod. Phys. **84**, 1067 (2012).

[79] E. V. Kurganova, A. J. M. Giesbers, R. V. Gorbachev, A. K. Geim, K. S. Novoselov, J. C. Maan, and U. Zeitler, Solid State Commun. **150**, 2209 (2010).

[80] I. V. Lerner and Yu. E. Lozovik, Zh. Eksp. Teor. Fiz. **78**, 1167 (1980) [Sov. Phys. JETP **51**, 588 (1981)].

[81] Z. Q. Li, E. A. Henriksen, Z. Jiang, Z. Hao, M. C. Martin, P. Kim, H. L. Stormer, and D. N. Basov, Phys. Rev. Lett. **102**, 037403 (2009).

[82] Z. Q. Li, E. A. Henriksen, Z. Jiang, Z. Hao, M. C. Martin, P. Kim, H. L. Stormer, and D. N. Basov, Nat. Phys. **4**, 532 (2008).

[83] K. Lier and R. R. Gerhardts, Phys. Rev. B **50**, 7757 (1994).

[84] Yu. E. Lozovik and A. A. Sokolik, Nanoscale Res. Lett. **7**, 134 (2012).

[85] G. Li, A. Luican, and E. Y. Andrei, Phys. Rev. Lett. **102**, 176804 (2009).

[86] M. Lotya, P. J. King, U. Khan, S. De, and J. N. Coleman, ACS Nano **4**, 3155 (2010).

[87] V. Lukose, R. Shankar, and G. Baskaran, Phys. Rev. Lett. **98**, 116802 (2007).

[88] A. H. MacDonald, J. Phys. C: Solid State Phys. **18**, 1003 (1985).

[89] K. F. Mak, M. Y. Sfeir, Y. Wu, C. H. Lui, J. A. Misewich, and T. F. Heinz, Phys. Rev. Lett. **101**, 196405 (2008).

[90] K. F. Mak, C. H. Lui, J. Shan, and T. F. Heinz, Phys. Rev. Lett. **102**, 256405 (2009).

[91] J. Martin, B. E. Feldman, R. T. Weitz, M. T. Allen, and A. Yacoby, Phys. Rev. Lett. **105**, 256806 (2010).

[92] E. McCann and V. I. Falko, Phys. Rev. Lett. **96**, 086805 (2006).

[93] E. McCann, Phys. Rev B **74**, 161403 (2006).

[94] J. W. McClure, Phys. Rev. **104**, 666 (1956).

[95] J. W. McClure, Phys. Rev. **108**, 612 (1957).

[96] P. Miró, M. Audiffred, and T. Heine, Chem. Soc. Rev. **43**, 6537 (2014).

[97] T. Misumi and K. Shizuya, Phys. Rev. B **77**, 195423 (2008).

[98] K. Miyagawa, M. Hirayama, M. Tamura, and K. Kanoda, J. Phys. Soc. Jpn. **79**, 063703 (2010).

[99] G. Montambaux, F. Piéchon, J.-N. Fuchs, and M. O. Goerbig, Eur. Phys. J. B **72**, 509 (2009).

[100] G. Montambaux, F. Piéchon, J.-N. Fuchs, and M. O. Goerbig, Phys. Rev. B **80**, 153412 (2009).

[101] M. Monteverde, M. O. Goerbig, P. Auban-Senzier, F. Navarin, H. Henck, C. R. Pasquier, C. Mézière, and P. Batail, Phys. Rev. B **87**, 245110 (2013).

[102] T. Mori, A. Kobayashi, Y. Sasaki, H. Kobayashi, G. Saito, and H. Inokuchi, Chem. Lett. **13**, 957 (1984).

[103] T. Mori, J. Phys. Soc. Jpn. **79**, 014703 (2010).

[104] T. Mori, J. Phys. Soc. Jpn. **82**, 034712 (2013).

[105] T. Morinari, T. Himura, and T. Tohyama, J. Phys. Soc. Jpn. **78**, 023704 (2009).

[106] S. A. Moskalenko, M. A. Liberman, P. I. Khadzhi, E. V. Dumanov, I. V. Podlesny, and V. Botan, Solid State Commun. **140**, 236 (2006).

[107] M. Mucha-Kruczyński, E. McCann, and V. I. Fal'ko, Solid State Commun. **149**, 1111 (2009).

[108] M. Mucha-Kruczyński, O. Kashuba, and V. I. Fal'ko, Phys. Rev. B **82**, 045405 (2010).

[109] K. Murata, S. Kagoshima, S. Yasuzuka, H. Yoshino, and R. Kondo, J. Phys. Soc. Jpn. **75**, 051015 (2006).

[110] R. R. Nair, P. Blake, A. N. Grigorenko, K. S. Novoselov, T. J. Booth, T. Stauber, N. M. R. Peres, and A. K. Geim, Science **320**, 1308 (2008).

[111] A. H. Castro Neto, F. Guinea, N. M. R. Peres, K. S. Novoselov, and A. K. Geim, Rev. Mod. Phys. **81**, 109 (2009).

[112] T. Nishine, A. Kobayashi, and Y. Suzumura, J. Phys. Soc. Jpn. **79** 114715 (2010).

[113] T. Nishine, A. Kobayashi, and Y. Suzumura, J. Phys. Soc. Jpn. **80** 114713 (2011).

[114] K.S. Novoselov, A. K. Geim, S. V. Morozov, D. Jiang, M. I. Katsnelson, I. V. Grigorieva, S. V. Dubonos, and A. A. Firsov, Nature **438**, 197 (2005).

[115] K. S. Novoselov, E. McCann, S. V. Morozov, V. I. Falko, M. I. Katsnelson, U. Zeitler, D. Jiang, F. Schedin, and A. K. Geim, Nat. Phys. **2**, 177 (2006).

[116] T. Ohta, A. Bostwick, T. Seyller, K. Horn, and E. Rotenberg, Science **313**, 951 (2006).

[117] D. Olego, A. Pinczuk, A. C. Gossard, and W. Wiegmann, Phys. Rev. B **26**, 7867 (1982).

[118] T. Osada, J. Phys. Soc. Jpn. **77**, 084711 (2008).

[119] T. Osada, J. Phys. Soc. Jpn. **80**, 033708 (2011).

[120] S. Park and R. S. Ruoff, Nat. Nanotechnol. **4**, 217 (2009).

[121] J. M. Pereira, Jr., F. M. Peeters, and P. Vasilopoulos, Phys. Rev. B **76**, 115419 (2007).

[122] N. M. R. Peres and E. V. Castro, J. Phys.: Condens. Matter **19**, 406231 (2007).

[123] N. M. R. Peres, Rev. Mod. Phys. **82**, 2673 (2010).

[124] A. Pinczuk, S. Schmitt-Rink, G. Danan, J. P. Valladares, L. N. Pfeiffer, and K. W. West, Phys. Rev. Lett. **63**, 1633 (1989).

[125] A. Pinczuk, B. S. Dennis, L. N. Pfeiffer, and K. West, Phys. Rev. Lett. **70**, 3983 (1993).

[126] A. Pinczuk, B. S. Dennis, L. N. Pfeiffer, and K. W. West, Semicond. Sci. Technol. **9**, 1865 (1994).

[127] M. A. Eriksson, A. Pinczuk, B. S. Dennis, S. H. Simon, L. N. Pfeiffer, and K. W. West, Phys. Rev. Lett. **82**, 2163 (1999).

[128] M. Kang, A. Pinczuk, B. S. Dennis, L. N. Pfeiffer, and K. W. West, Phys. Rev. Lett. **86**, 2637 (2001).

[129] J. Yan, S. Goler, T. D. Rhone, M. Han, R. He, P. Kim, V. Pellegrini, and A. Pinczuk, Phys. Rev. Lett. **105**, 227401 (2010).

[130] T. D. Rhone, D. Majumder, B. S. Dennis, C. Hirjibehedin, I. Dujovne, J. G. Groshaus, Y. Gallais, J. K. Jain, S. S. Mandal, Aron Pinczuk, L. Pfeiffer, and K. West, Phys. Rev. Lett. **106**, 096803 (2011).

[131] J. M. Poumirol, W. Yu, X. Chen, C. Berger, W. A. de Heer, M. L. Smith, T. Ohta, W. Pan, M. O. Goerbig, D. Smirnov, and Z. Jiang, Phys. Rev. Lett. **110**, 246803 (2013).

[132] R. Roldán, J.-N. Fuchs, and M. O. Goerbig, Phys. Rev. B **80**, 085408 (2009); R. Roldán, M. O. Goerbig and J.-N. Fuchs, Semicond. Sci. Technol. **25**, 034005 (2010).

[133] R. Roldán, J.-N. Fuchs, and M. O. Goerbig, Phys. Rev. B **82**, 205418 (2010).

[134] R. Roldán, M. O. Goerbig, and J.-N. Fuchs, Phys. Rev. B **83**, 205406 (2011).

[135] M. L. Sadowski, G. Martinez, M. Potemski, C. Berger, and W. A. de Heer, Phys. Rev. Lett. **97**, 266405 (2006).

[136] M. Sato, K. Miura, S. Endo, S. Sugawara, N. Tajuma, K. Murata, Y. Nishio, and K. Kajita J. Phys. Soc. Jpn **80**, 023706 (2011).

[137] G. W. Semenoff, Phys. Rev. Lett. **53**, 2449 (1984).

[138] K. Shizuya, Phys. Rev. B **81**, 075407 (2010).

[139] K. Shizuya, Phys. Rev. B **86**, 045431 (2012).

[140] K. W. K. Shung, Phys. Rev. B **34**, 979 (1986).

[141] J. C. Slonczewski and P. R. Weiss, Phys. Rev. **109**, 272 (1958).

[142] J. Sólyom, *Fundamentals of the Physics of Solids, Volume I-III* (Springer, Berlin, 2010).

[143] S. L. Sondhi, A. Karlhede, S. A. Kivelson, and E. H. Rezayi, Phys. Rev. B **47**, 16419 (1993).

[144] R. Sooryakumar, A. Pinczuk, A. Gossard, and W. Wiegmann, Phys. Rev. B **31**, 2578 (1985).

[145] F. Stern, Phys. Rev. Lett. **18**, 546 (1967).

[146] C.-Y. Su, A.-Y. Lu, Y. Xu, F.-R. Chen, A. N. Khlobystov, and L.-J. Li, ACS Nano **5**, 2332 (2011).

[147] S. Sugawara, M. Tamura, N. Tajima, R. Kato, M. Sato, Y. Nishio, and K. Kajita, J. Phys. Soc. Jpn. **79**, 113704 (2010).

[148] N. Tajima, M. Tamura, Y. Nishio, K. Kajita, and Y. Iye, J. Phys. Soc. Jpn. **69**, 543 (2000).

[149] N. Tajima, A. Ebina-Tajima, M. Tamura, Y. Nishio, and K. Kajita, J. Phys. Soc. Jpn. **71**, 1832 (2002).

[150] N. Tajima, A. Tajima, M. Tamura, R. Kato, Y. Nishio, and K. Kajita, J. Phys. IV (Paris) **114**, 263 (2004).

[151] N. Tajima, S. Sugawara, M. Tamura, Y. Nishio, and K. Kajita, J. Phys. Soc. Jpn. **75**, 051010 (2006).

[152] N. Tajima, S. Sugawara, R. Kato, Y. Nishio, and K. Kajita, Phys. Rev. Lett. **102**, 176403 (2009).

[153] N. Tajima and K. Kajita, Sci. Technol. Adv. Mater. **10**, 024308 (2009).

[154] N. Tajima, T. Yamauchi, T. Yamaguchi, M. Suda, Y. Kawasugi, H. M. Yamamoto, R. Kato, Y. Nishio, and K. Kajita, Phys. Rev. B **88**, 075315 (2013).

[155] B. Tanatar and D. M. Ceperley, Phys. Rev. B **39**, 5005 (1989).

[156] R. Y. Tay, M. H. Griep, G. Mallick, S. H. Tsang, R. S. Singh, T. Tumlin, E. H. Tong Teo, and S. P. Karna, Nano Lett. **14**, 839 (2014).

[157] C. Tőke and V. I. Fal'ko, Phys. Rev. B **83**, 115455 (2011).

[158] C. Tőke , Phys. Rev. B **88**, 241411(R) (2013).

[159] P. R. Wallace, Phys. Rev. **71**, 622 (1947).

[160] D. Wang and G. Jin, Europhys. Lett. **92**, 57008 (2010).

[161] Q. H. Wang, K. Kalantar-Zadeh, A. Kis, J. N. Coleman, and M. S. Strano, Nat. Nanotechnol. **7**, 699 (2012).

[162] J. Wang, S. Deng, Z. Liu, and Z. Liu, Nat. Sci. Rev. **2**, 22 (2015).

[163] H. Wei, S.-P. Chao, and V. Aji, Phys. Rev. B **86**, 041403(R) (2012).

[164] R. T. Weitz, M. T. Allen, B. E. Feldman, J. Martin, and A. Yacoby, Science **330**, 812 (2010).

[165] B. Wunsch, T. Stauber, F. Sols, and F. Guinea, New J. Phys. **8**, 318 (2006).

[166] X. Yin, X. Liu, Y.-T. Pan, K. A. Walsh, and H. Yang, Nano Lett. **14**, 7188 (2014).

[167] J. Xue, arXiv:1309.6714 (2013).

[168] K. Yang, S. Das Sarma, and A. H. MacDonald, Phys. Rev. B **74**, 075423 (2006).

[169] A. F. Young and P. Kim, Nat. Phys. **5**, 222 (2009).

[170] Y. Zhang, Y.-W. Tan, H. L. Stormer, and P. Kim, Nature **438**, 201 (2005).

[171] L. M. Zhang, Z. Q. Li, D. N. Basov, M. M. Fogler, Z. Hao, and M. C. Martin, Phys. Rev. B **78**, 235408 (2008).

[172] Y. Zhang, T.-T. Tang, C. Girit, Z. Hao, M. C. Martin, A. Zettl, M. F. Crommie, Y. R. Shen, and F. Wang, Nature, **459** 820, (2009).

[173] L. M. Zhang, M. M. Fogler, and D. P. Arovas, Phys. Rev. B **84**, 075451 (2011).

[174] Y. Zhao, P. Cadden-Zimansky, Z. Jiang, and P. Kim, Phys. Rev. Lett. **104**, 066801 (2010).

[175] K. Zou, X. Hong, J. Zhu, Phys. Rev. B **84**, 085408 (2011).

[176] N. Zettili, *Quantum Mechanics: Concepts and Applications* (John Wiley & Sons, Chichester, 2009).